ASPECTS OF THE MODULATION OF COSMIC RAYS IN THE OUTER HELIOSPHERE

by

MABEDLE DONALD NGOBENI, B.Sc. Hons.

Dissertation accepted in partial fulfilment of the requirements for the degree Magister Scientiae in Physics at the North-West University (Potchefstroom Campus)

Supervisor: Prof. M. S. Potgieter
Assistant Supervisor: Dr. U. W. Langner

November 2006
Potchefstroom
South Africa

ABSTRACT

A time-dependent two-dimensional (2D) modulation model including drifts, the solar wind termination shock (TS) with diffusive shock acceleration and a heliosheath based on the Parker (1965) transport equation is used to study the modulation of galactic cosmic rays (GCRs) and the anomalous component of cosmic rays (ACRs) in the heliosphere. In particular, the latitude dependence of the TS compression ratio and injection efficiency of the ACRs (source strength) based on the hydrodynamic modeling results of Scherer et al. (2006) is used for the first time in a modulation model. The subsequent effects on differential intensities for both GCRs and ACRs are illustrated, comparing them to the values without a latitude dependence for these parameters. It is found that the latitude dependence of these parameters is important and that it enables an improved description of the modulation of ACRs beyond the TS. With this modeling approach (without fitting observations) to the latitude dependence of the two parameters, it is possible to obtain a TS spectrum for ACRs at a polar angle of $\theta = 55°$ that qualitatively approximates the main features of the Voyager 1 observations. This positive result has to be investigated further. Additionally, it is shown that the enhancement of the cosmic ray intensity just below the cut-off energy found for the ACR at the TS in an $A < 0$ magnetic polarity cycle in the equatorial plane with the latitude independent scenario, disappears in this region when the latitude dependence of the compression ratio and injection efficiency is assumed. Subsequent effects of these scenarios are illustrated on the global anisotropy vector of both GCRs and ACRs as the main theme of this work. For this purpose the radial and latitudinal gradients for GCRs and ACRs were accurately computed. The radial and latitudinal anisotropy components were then computed as a function of energy, radial distance and polar angle. It is also the first time that the anisotropy vector is comprehensively calculated in such a global approach to cosmic ray modeling in the heliosphere, in particular for ACRs. It is shown that the anisotropy vector inside (up-stream) and outside (down-stream) the TS behaves in a complicated way, so care must be taken in interpreting it. It is found that the latitude dependence of the two mentioned parameters can alter the direction (sign) of the anisotropy vector. Its behaviour beyond the TS is markedly different from inside the TS, mainly because of the slower solar wind velocity, with less dependence on the magnetic polarity cycles.

Keywords: Termination shock, heliosheath, cosmic rays, anomalous cosmic rays, heliospheric modulation, solar wind, transport processes, cosmic ray anisotropy

SAMEVATTING

'n Tydafhanklike, twee-dimensionele (2D) modulasie-model gebaseer op die Parker-transportvergelyking (Parker, 1965) wat dryf, die terminasieskok (TS) van die sonwind en diffuse skokversnelling en die heliosfeermantel insluit, word aangewend om die heliosferiese modulasie van galaktiese (GKS) en anomale kosmiese strale (AKS) te bestudeer. Die afhanklikheid van die TS se kompressieverhouding en van die inspuit-effektiwiteit van AKS van helio-breedtegraad word vir die eerste keer in besonderhede ondersoek en is gebaseer op die hidrodinamiese model-resultate van Scherer et al. (2006). Die effekte op die differensiële intensiteit van GKS en AKS word illustreer en vergelyk met resultate sonder die genoemde breedtegraads-afhanklikheid. Die navorsing toon aan dat hierdie afhanklikheid belangrik is en die beskrywing van die modulasie van AKS naby die TS verbeter sodat die simulasies kwalitatief die waarnemings van AKS met Voyager 1 kan nadoen. Hierdie positiewe resultaat moet verder ondersoek word. Vervolgens word aangetoon dat die verhoging in die AKS-spektrum onder die afsny-energie (sogenaamde bultvorming) tydens die $A < 0$ magnetiese polariteitsiklus by die TS in die ewenaarsgebiede verdwyn met die breedtegraads-afhanklike benadering. As hooftema van hierdie werk word die daaropvolgende effekte van bogenoemde benadering vir die globale anisotropie-vektor van GKS en AKS illustreer. Die radiale en breedtegraads-gradiënte is vir die doel akkuraat numeries bereken en gebruik om die oorstemmende anisotropie-vektorkomponente as funksie van energie, radiale afstand en breedtegraad te bereken. Dit is ook die eerste keer dat hierdie komponente so omvattend vir AKS met 'n globale modulasiemodel bereken word. Die resultate toon aan dat die anisotropie-vektor heelwat verskil aan die binnekant (stroom-op) en aan die buitekant (stroom-af) van die TS en 'n baie komplekse gedrag het sodat die berekenings versigtig verklaar moet word. Die verskille is hoofsaaklik aan die stadiger sonwind in die heliomantel toe te skryf. Die effek van die veranderende magnetiese polariteitsiklusse is heelwat minder in die gebied verby die TS.

NOMENCLATURE

ACRs	Anomalous component of Cosmic Rays
ADI	Alternating Direct Implicit
AU	Astronomical Unit
CME	Coronal Mass Ejection
CR	Cosmic Ray
ESP	Energetic Storm Particles
GCR	Galactic Cosmic Ray
HCS	Heliospheric Current Sheet
HD	Hydrodynamic
HMF	Heliospheric Magnetic Field
HP	Heliopause
LIS	Local Interstellar Spectra
LISM	Local Interstellar Medium
LOD	Locally One-Dimensional
MHD	MagnetoHydroDynamic
MIR	Merged Interaction Region
PDE	Partial Differential Equation
QLT	Quasi-Linear Theory
SEP	Solar Energetic Particles
TPE	Transport Equation
TS	Termination Shock
V1	Voyager 1
1D	One-dimensional
2D	Two-dimensional
3D	Three-dimensional

TABLE OF CONTENTS

1 INTRODUCTION 3

2 COSMIC RAYS AND THE HELIOSPHERE 6

2.1 INTRODUCTION 6
2.2 THE SUN 6
2.2.1 Why study the Sun? 7
2.3 THE SOLAR WIND 8
2.4 THE HELIOSPHERIC MAGNETIC FIELD 11
2.5 HELIOSPHERIC CURRENT SHEET 13
2.6 SOLAR CYCLE VARIATION 15
2.7 THE HELIOSPHERE 16
2.7.1 Geometry of the heliosphere 17
2.7.2 Termination shock 18
2.7.3 Heliosheath 19
2.8 CHARGED PARTICLES IN THE HELIOSPHERE 19
2.8.1 Galactic cosmic rays 20
2.8.2 Anomalous cosmic rays 20
2.8.3 Energetic particles 21
2.9 SPACE MISSIONS 22
2.9.1 Ulysses mission 22
2.9.2 Voyager missions 22
2.10 SUMMARY 23

3 THE TRANSPORT EQUATION AND NUMERICAL MODELS 24

3.1. INTRODUCTION 24
3.2 THE PARKER TRANSPORT EQUATION 24
3.3 PARTICLE DRIFTS 26
3.4 THE ELEMENTS OF THE DIFFUSION TENSOR 27
3.4.1 Diffusion theory 28
3.4.2 Cosmic ray approach 30
3.4.2.1 The parallel diffusion coefficient 32
3.4.2.2 The perpendicular diffusion coefficient 34
3.4.2.3 The drift term 36
3.5 SHOCK ACCELERATION 38
3.5.1 First-order Fermi acceleration 39
3.5.2 Second-order Fermi acceleration 39
3.6 NUMERICAL MODULATION MODELS 39
3.6.1 Boundary conditions 40
3.6.2 Termination shock models 41
3.6.3 The numerical solution of the TPE 42
3.7 SUMMARY 42

4 EFFECTS OF THE LATITUDE DEPENDENCE OF THE SHOCK'S COMPRESSION RATIO AND THE INJECTION EFFICIENCY ON COSMIC RAY SPECTRA IN THE HELIOSPHERE 44

4.1 INTRODUCTION 44
4.2 COSMIC RAY INTENSITIES AT THE TS AS MEASURED BY V1 45
4.3 THE LATITUDE DEPENDENCE OF THE SHOCK'S COMPRESSION RATIO AND OF THE INJECTION EFFICIENCY 46
4.4 THE EFFECTS OF THE LATITUDE DEPENDENT COMPRESSION RATIO ON GCR PROTON SPECTRA 49
4.5 THE EFFECTS OF THE LATITUDE DEPENDENT COMPRESSION RATIO AND INJECTION EFFICIENCY ON ACR PROTON SPECTRA 52
4.6 EFFECTS OF A NEGATIVE DIVERGENCE OF V IN THE HELIOSHEATH 59
4.7 ACR INTENSITY RATIOS 62
4.8 SUMMARY AND CONCLUSIONS 64

5 COSMIC RAY LATITUDINAL AND RADIAL GRADIENTS .. 66

5.1 INTRODUCTION 66
5.2 COSMIC RAY INTENSITY GRADIENTS 66
5.2.1 The radial gradients 67
5.2.2 The latitudinal gradients 77
5.3 SUMMARY AND CONCLUSIONS 81

6 COSMIC RAY ANISOTROPIES IN THE HELIOSPHERE 83

6.1 INTRODUCTION 83
6.2 ANISOTROPIES 83
6.3 RADIAL COMPONENT OF THE ANISOTROPY VECTOR 84
6.3.1 Energy dependence of the radial anisotropy 85
6.3.2 Spatial dependence of the radial anisotropy 92
6.4 LATITUDINAL COMPONENT OF THE ANISOTROPY VECTOR 100
6.5 THE EFFECTS OF THE LATITUDE DEPENDENCE OF THE COMPRESSION RATIO AND THE INJECTION EFFICIENCY ON CR ANISOTROPIES. 109
6.6 SUMMARY AND CONCLUSIONS 116

7 SUMMARY AND CONCLUSIONS 119

REFERENCES 125

ACKNOWLEDGEMENTS 135

Chapter 1

Introduction

Galactic cosmic rays (GCRs) that enter our heliosphere encounter an outward flowing solar wind which carries a turbulent magnetic field. Of importance is the interaction between these energetic charged particles and the interplanetary medium. This interaction reduces the cosmic ray intensity below the level of the local interstellar spectrum, a phenomenon called the heliospheric modulation of cosmic rays. Besides GCRs, there is another population of charged particles of importance to this study known as the anomalous component of cosmic rays (ACRs) which enter the heliosphere as interstellar neutrals because of the movement of the heliosphere through interstellar space. These particles penetrate deeply into the heliosphere before they become ionized by charge exchange with the solar wind ions, electron collisions, or photo-ionization. These ionized atoms are then picked up by the solar wind and convected outwards towards the outer heliosphere, where they are accelerated at and beyond the solar wind termination shock (TS) gaining energy by multiple crossing of the TS. Some of these particles then diffuse into the heliosphere, where they are modulated by the same processes as GCRs. This study focuses mainly on modeling the modulation of GCR and ACR protons in the outer heliosphere.

Much progress has been made over the past decade in the field of modulation studies. An example is the development of an extended two-dimensional (2D) modulation model including drifts, the diffusive shock acceleration at the TS, and the effects of the heliosheath (Steenkamp, 1995; Steenberg, 1998; Ferreira, 2002; Langner, 2004), which describes the relevant physics of the transport of particles in the outer heliosphere. These authors assumed a constant compression ratio of the TS over all latitudes and hence effects of a compression ratio changing over latitudes on modulation of cosmic rays have not been shown before.

The main aim of this dissertation is to investigate the latitudinal dependence of the compression ratio and injection efficiency of the ACR source, and to further illustrate their subsequent effects on the modulation and anisotropy components of GCR and ACR protons in the heliosphere. This is motivated by the observations made by Voyager 1 (V1) in the heliosheath after crossing the TS on the 16th of December 2004 (Stone et al., 2005; Decker et al., 2005), which indicate that at the location of the TS encountered by V1, no direct

evidence was found of the source of the ACRs, and that the compression ratio of the TS was ~ 2.5, calculated from the spectral index of the power law type intensity profiles, but it could be as low as 2. This observation confirms that the TS is not a strong shock, at least not where V1 crossed into the heliosheath. Furthermore, as V1 flew downstream from the TS, the intensities of ACRs continued to grow, as if its source still lay ahead (Fisk, 2005). The effects of a moderate negative divergence of the solar wind velocity in the heliosheath, which imply that further acceleration of particles in the heliosheath occur as shown by Langner et al. (2006a, 2006b), are also studied for ACR protons.

The structure of this dissertation is as follows:

Chapter 2: This chapter introduces the reader to the study of cosmic rays and the heliosphere. It starts with a brief discussion of the Sun, the solar wind, the heliospheric magnetic field, the heliospheric current sheet, solar cycle variations, the geometry of the heliosphere and charged particles in the heliosphere, in particular GCRs as fully ionized particles with kinetic energy $E > 1$ MeV that traverse the heliosphere. It closes with a concise discussion of selected spacecraft missions, which provide valuable observations for comparison with numerical models.

The transport processes that affect and determine the transport of cosmic rays throughout the heliosphere, as combined in the transport equation (Parker, 1965), as well as a brief discussion of the 2D shock acceleration model is given in **Chapter 3**. A description of diffusive acceleration, and the diffusion tensor constructed by Langner (2004) based mainly on the work of Burger et al. (2000), as used in this work, is also given here.

In **Chapter 4**, a new relation of the latitude dependence of the TS compression ratio and the injection efficiency is established based on the hydrodynamic modeling results of Scherer et al. (2006). The effects of the latitude dependence of these TS parameters on the computed intensities of GCR and ACR protons are illustrated in comparison to those when these two parameters are latitude independent. This is done to accentuate the modulation effects associated with the latitude dependent compression ratio and injection efficiency. This chapter closes with the investigation of a negative divergence of the solar wind velocity in the heliosheath which is combined with the latitude dependence of the two mentioned parameters to enable improved modeling, the effects of which are illustrated.

The radial and latitudinal (polar) gradients of GCRs and ACRs are studied in **Chapter 5** and the effects of the latitude dependences of the TS parameters established in Chapter 4 on these intensity gradients are illustrated. Such computations together with measurements of

these gradients by space probes provide crucial information about the diffusion tensor and for our understanding of the modulation and propagation of charged particles in the HMF.

The energy and spatial dependence of various physical components of the anisotropy vector for both GCRs and ACRs and how they change across the TS are investigated in **Chapter 6** using the 2D shock acceleration model of Langner (2004). These anisotropy studies have become of special interest (McDonald et al., 2003; Krimigis et al., 2003) since 2002 when the first flux enhancements of charged particles associated with the approach of V1 to the TS were observed. The effects of the latitude dependence of the compression ratio and the injection efficiency on the two components of the anisotropy vector are illustrated.

A summary of this work is given in **Chapter 7**.

Extracts of this dissertation from Chapter 4 (latitude dependence of the compression ratio and the injection efficiency) and from Chapter 6 (radial anisotropy component of the anisotropy vector) have been accepted for publication in Advances in Space Research (Ngobeni and Potgieter, 2007). Results of this dissertation were presented at the last two annual conferences of the South African Institute of Physics in 2005 and 2006. A poster presentation was made at the 36th COSPAR Scientific Assembly.

Chapter 2

Cosmic rays and the heliosphere

2.1 Introduction

This chapter introduces the reader to the study of cosmic rays (CRs) and the heliosphere. It starts with a brief discussion of the Sun, the solar wind, the heliospheric magnetic field, the heliospheric current sheet, solar cycle variations, the heliospheric geometry and charged particles in the heliosphere, in particular GCRs as mostly fully ionized particles with kinetic energy $E > 1$ MeV that traverse the heliosphere. It closes with a concise discussion of selected spacecraft missions, which provide valuable observations and insight for modulation studies.

2.2 The Sun

The Sun is our nearest star, it is of intermediate size and luminosity with radius of about ~ 0.005 AU (one astronomical unit = 1.49×10^8 km, the average distance between the Sun and Earth). The Sun has a differential rotational period that increases with latitude from an average of ~ 25 days at the equator up to even ~ 32 days near the polar regions. This behavior is due to the fact that the Sun is not a solid body like Earth but a gravitating plasma sphere. The Sun is mainly composed of Hydrogen (~ 90%) and Helium (~ 10%) with traces of heavier elements such as Carbon, Nitrogen and Oxygen. The visible solar surface is called the photosphere. It is the apparent solar surface that emits most of the Sun's light and heat. Visible on the photosphere of the Sun are sunspots which are regions of the surface cooler than their surroundings and containing intense magnetic fields. Detailed records of the sunspot numbers, which are a direct indication of the level of solar activity, are shown in Figure 1 from 1750 up to 2005 as function of time (data from http://www.spaceweather.com). From these observations of monthly averaged values of the sunspot numbers, it is evident that the Sun has a quasi-periodic ~ 11 year cycle called a solar activity cycle. Every ~ 11 years the Sun moves through a period of fewer and smaller sunspots called "solar minimum" followed by a period of larger and more sunspots called "solar maximum" (e.g., Smith and Marsden, 2003).

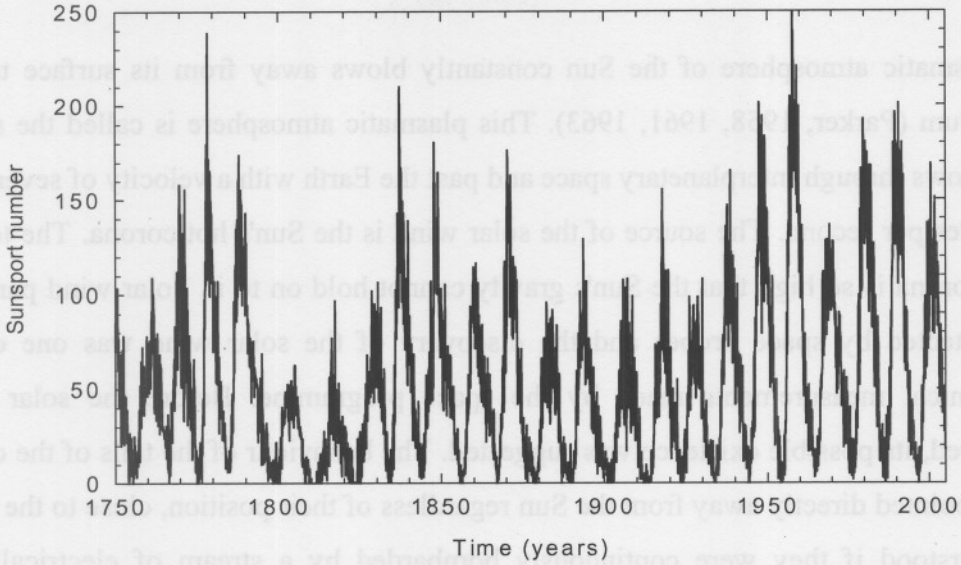

Figure 2.1. Yearly averaged sunspot number from the year 1750 up to 2005 (data from *http://www.spaceweather.com*).

2.2.1 Why study the Sun?

The Sun is the source of light and heat for life on Earth. The Sun is also the source of the solar wind, discussed below, which flows past the Earth at supersonic speeds. Disturbances in the solar wind "shake" the Earth's magnetic field and pump energy into the radiation belts. Regions on the surface of the Sun often show flares and apart from energetic charged particles give off ultraviolet light to x-rays that "heat" up the Earth's upper atmosphere. This "Space Weather" can change the orbits of satellites and shorten mission lifetimes. The excess (particle) radiation can physically damage satellites and pose a threat to astronauts. Affecting the Earth's magnetic field can also cause electric current surges in power lines that destroy equipment and knock out power over large areas during particles of maximum activity. As we become more dependent upon satellites in space and 24 hours of reliable electric energy, we will increasingly feel the effects of space weather and need to predict it (http://spacescience.spaceref.com/ssl/pad/solar/whysolar.htm).

The Sun also serves in helping us to understand the rest of the universe. It is the only star close enough to reveal details about its surface and its influence sphere so that it is a key to understanding other stars. We really depend on the Sun for our daily lives and knowledge about the universe and its stars. The importance of the Sun from a cosmic ray point of view will be discussed in the next section.

2.3 The solar wind

The plasmatic atmosphere of the Sun constantly blows away from its surface to maintain equilibrium (Parker, 1958, 1961, 1963). This plasmatic atmosphere is called the solar wind, which flows through interplanetary space and past the Earth with a velocity of several hundred kilometres per second. The source of the solar wind is the Sun's hot corona. The temperature of the corona is so high that the Sun's gravity cannot hold on to it. Solar wind particles have been detected by space probes and the discovery of the solar wind was one of the first astronomical measurements made by the space programme. Before the solar wind was discovered, its possible existence was suggested. The behaviour of the tails of the comets that always pointed directly away from the Sun regardless of their position, close to the Sun, could be understood if they were continuously bombarded by a stream of electrically charged particles emitted by the Sun (Biermann, 1951, 1961). Biermann's estimates of the solar wind speed, V, ranged between 400-1000 km.s^{-1} which was remarkably accurate. However, the name "solar wind" was first introduced by Parker (1958). For a review, see Fichtner (2001), and references therein.

Observations over many years have revealed that V is not uniform over all heliolatitudes and can be divided into the fast solar wind and the slow solar wind (e.g., Philips et al., 1994, 1995). The basic reason is that the Sun's magnetic field dominates the original outflow of the solar wind (e.g., Smith, 2000). If the solar magnetic field is perpendicular to the radial outflow of the solar wind it can prevent the outflow. This is usually the case at low solar latitudes where the near Sun magnetic field lines are parallel to the Sun's surface. These field lines are in the form of loops which begin and end on the solar surface and stretch around the Sun to form the streamer belts. These streamer belts are regarded as the most plausible sources of the slow solar wind speed which have typical velocities of $V \sim 400$ km.s^{-1} (Schwenn, 1983; Marsch, 1991; Withroe et al., 1992). Other indications are that the slow solar wind speed may arise from the edges of large coronal holes or from smaller coronal holes (e.g., Hundhausen, 1977; McComas et al., 2002a).

In regions where the solar magnetic field is directed radially outward, such as at the solar polar regions, the magnetic field will assist rather than oppose the coronal outflow. The fast solar wind with a characteristic average speed of up to $V \approx 800$ km.s^{-1} emanates from the polar coronal holes that are located at the higher heliographic latitudes (e.g., Krieger et al., 1973; McComas et al., 2002b; Neugebauer et al., 2002; Hu et al., 2003). In these regions the magnetic field lines are carried off by the solar wind and their connections to the Sun at the

one end of the field line is lost. These quasi-open magnetic field lines affect the transport of CRs in the heliosphere. The fast solar wind from the polar regions can sometimes extend close to the equator and overtake the earlier emitted slow stream, resulting in corotating interaction regions (CIRs), see Odstrcil (2003) for a review.

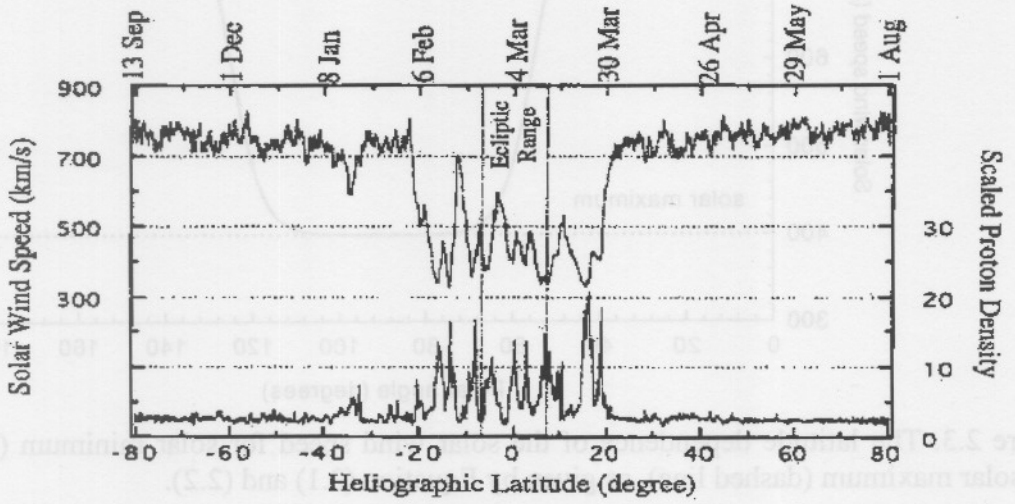

Figure 2.2. Six-hour average solar wind speed (top curve) for the pole-to-pole transit of Ulysses from the peak southerly latitude of -80.2° on 12 September 1994, to the corresponding northerly latitude on 31 July 1995. The proton density is shown by the bottom curve (from Philips et al., 1995).

The latitudinal dependence of V during solar minimum activity has been confirmed by Ulysses spacecraft observations (Philips et al., 1994, 1995) and is shown in Figure 2.2 as six hour averages during the fast pole-to-pole transit of Ulysses spacecraft. Evident from Figure 2.2 are significant variations of V with heliolatitude. Ulysses has observed a high solar wind speed, 700-800 km.s^{-1} at $\geq \sim 20°$ S, but in the $\sim 20°$ S to the $\sim 20°$ N band it observed medium to slow speeds, $\sim$ 400 km.s^{-1}, after which the solar wind speed increases again to speeds between 700-800 km.s^{-1} at $\sim 20°$ N, thus confirming the existence of the fast and slow solar wind during solar minimum. In contrast, for solar maximum activity no well-defined high speed solar wind is observed (e.g., Richardson et al., 2001; McComas et al., 2002b).

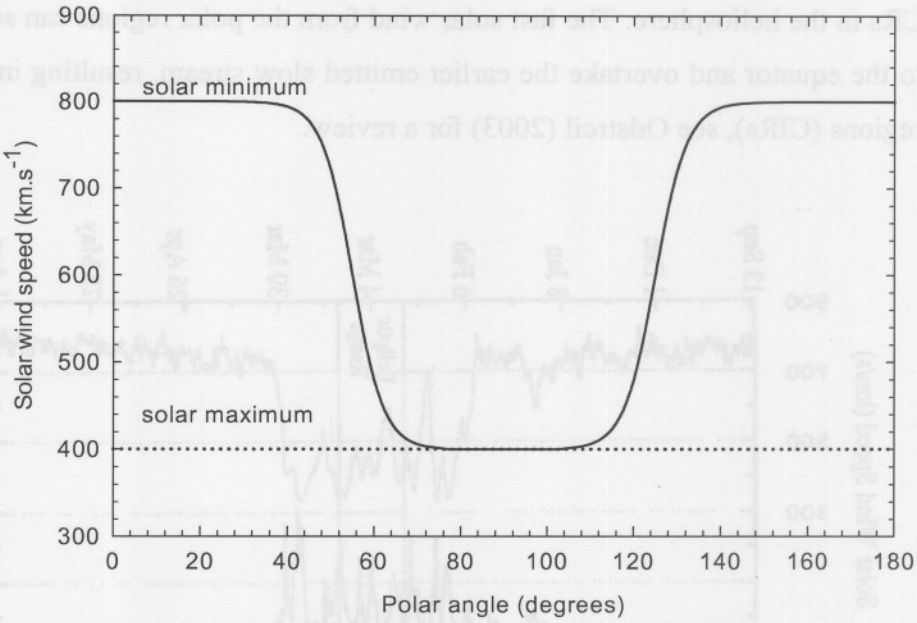

Figure 2.3. The latitude dependence of the solar wind speed for solar minimum (solid line) and solar maximum (dashed line), as given by Equation (2.1) and (2.2).

The radial dependence of V between 0.1 AU and 1.0 AU was studied by e.g., Kojima et al. (1991) and Sheeley et al. (1997). They have found that both the low and high speed winds accelerate within 0.1 AU of the Sun and become a steady flow at 0.3 AU. Using measurements from Pioneer 10 and 11 and Voyagers 1 and 2, Gazis et al. (1994) and Richardson et al. (2001) have found that the slow averaged solar wind speed does not vary with distance up to several tens of AUs. However, it does show a solar cycle dependence with values about 20% higher during solar minimum than during solar maximum. At solar maximum there is a mixture of high speed and low speed winds in the region of the equator (Gazis et al., 1991) so that the picture is not as clear.

To model the solar wind velocity, **V**, in modulation models it is assumed that

$$\mathbf{V}(r,\theta) = V(r,\theta)\mathbf{e}_r = V_r(r)V_\theta(\theta)\mathbf{e}_r, \tag{2.1}$$

where r is the radial distance, θ the polar angle with $\mathbf{e}_r$ the unit vector in the radial direction. The latitude dependence of **V** during solar minimum conditions (e.g., Hattingh, 1998) is given as

$$\mathrm{V}_\theta(\theta) = 1.5 \mp 0.5 \tanh\left[\frac{2\pi}{45}(\theta - 90^0 \pm \varphi)\right], \tag{2.2}$$

in the northern and southern hemisphere respectively, with $\varphi = 35°$. For solar maximum the solar wind speed is assumed independent of latitude so that

$$V_\theta(\theta) = 1.0. \tag{2.3}$$

Figure 2.3 shows the latitude dependence of V as given by Equations (2.1) to (2.3) for solar minimum and solar maximum conditions respectively. The solid line shows solar minimum while the dotted line shows solar maximum conditions. For solar minimum there is a slow solar wind speed of 400 km.s^{-1} in the equatorial regions which increases in the polar regions to 800 km.s^{-1}. It is evident from Figure 2.3 that for moderate solar maximum conditions no latitudinal dependence is assumed, so that under these conditions the solar wind speed on average is assumed 400 km.s^{-1} for all latitudes.

The radial dependence of **V** is given as

$$V_r(r) = V_0\left\{1\text{-}\exp\left[\frac{40}{3}\left(\frac{r_\odot - r}{r_0}\right)\right]\right\}, \tag{2.4}$$

with $r_0 = 1$ AU, $V_0 = 400$ km.s^{-1}, $r_\odot = 0.005$ AU which is the radius of the Sun, and with r in AU (Hattingh, 1998). For more information on the latitudinal dependence of V and progress made to improve modeling of Equation (2.1), see Ferreira et al. (2001a, 2001b), Moeketsi (2004) and Moeketsi et al. (2005).

2.4 The heliospheric magnetic field

Due to the small resistivity of the solar wind plasma, the heliospheric magnetic field (HMF) is frozen-in so that it is carried with the solar wind throughout the heliosphere. The rotation of the Sun causes the HMF to have a spiral structure in and away from the Sun's equatorial plane. This is shown in Figure 2.4. This HMF plays an important role in the transport of cosmic rays in the heliosphere. Charged particles, such as cosmic rays, follow and gyrate along the HMF so that the magnetic field irregularities, due to turbulence, causes pitch angle scattering of these particles.

An equation for the spiral HMF as derived by Parker (1958) is

$$\mathbf{B} = B_0\left(\frac{r_0}{r}\right)^2\left(\mathbf{e}_r - \tan\psi\mathbf{e}_\phi\right), \tag{2.5}$$

where **B** is the HMF with unit vector components $\mathbf{e}_r$ and $\mathbf{e}_\phi$ in the radial and azimuthal direction respectively. Here the symbol ψ denotes the spiral angle which is the angle between the radial and the average HMF direction at a certain position. This spiral angle gives an indication of how tightly wound the HMF spiral is. A typical value is $\psi \approx 45°$ at Earth and it increases with r to $\sim 90°$ beyond 10 AU in the equatorial plane. The magnitude of the HMF at Earth is B_0, with an average value of $B_0 \approx 5$nT. The spiral angle is given by

$$\psi = \tan^{-1}\left(\frac{\Omega(r-r_\odot)\sin\theta}{V}\right), \tag{2.6}$$

where Ω is the angular speed of the Sun at its axis.

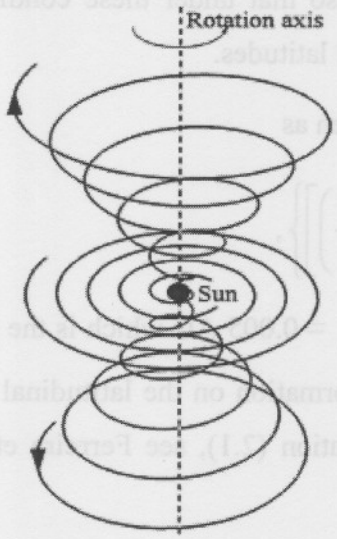

Figure 2.4. A three dimensional (3D) representation of the Parker HMF spiral structure with the Sun at the origin. Spirals rotate around the polar axis shown at $\theta = 45°$, $\theta = 90°$ and $\theta = 135°$ (from Hattingh, 1998).

Substituting Equation (2.6) into (2.5) yields

$$B = \frac{B_0 r_0^2}{r^2}\sqrt{1+\left(\frac{\Omega(r-r_\odot)\sin\theta}{V}\right)^2}, \tag{2.7}$$

for the magnitude of Parker HMF throughout the heliosphere.

The polar angle θ is measured from 0° at the polar axis of the Sun with $\theta = 90°$ the equatorial plane. However, at high latitude the geometry of the HMF is not just an ordinary Parker spiral as argued by Jokipii and Kóta (1989). The solar surface, where the "feet" of the field lines occur, is not a smooth surface, but a granular turbulent surface that keeps changing with time, especially in the polar regions. This turbulence may cause the field lines to wander randomly, creating transverse components in the field, thus causing temporal deviations from

the smooth Parker geometry. The effect of the more turbulent magnetic field in these regions is to increase the mean magnetic field strength. However, Jokipii and Kóta (1989) suggested a modification to Equation (2.7) so that

$$B = \frac{B_0 r_0^2}{r^2} \sqrt{1 + \left(\frac{\Omega (r - r_\odot) \sin\theta}{V} \right)^2 + \left(\frac{r \delta_m}{r_\odot} \right)^2} \; . \tag{2.8}$$

For $\delta_m = 0$ in Equation (2.8) there is no modification so that the standard Parker geometry is obtained. In this work a modification of $\delta_m = 0.002$ near the poles (at $\theta = 2.5°$) and $\delta_m \approx 0$ in the ecliptic plane is used (see also Haasbroek, 1993).

Qualitatively this modification is supported by measurements made of the HMF in the polar regions of the heliosphere by Ulysses (e.g., Balogh et al., 1995). This equation is therefore used in most modulation models (e.g., Ferreira, 2002; Langner, 2004).

Another modification was proposed by Smith and Bieber (1991) who based their modification on magnetic field data. This modification also changes the geometry of the magnetic field and affects the field strength over the poles. For an implementation of this modification in a numerical model see Haasbroek (1997). An alternative model for HMF has been proposed by Fisk (1996) based on the argument that the Sun does not rotate rigidly, but rather differentially with the solar poles rotating ~ 20% slower than the solar equator (e.g., Snodgrass, 1983). The Fisk model includes a meridional component which is not present in the Parker model. This could account for observations from Ulysses spacecraft of recurrent energetic particles events at higher latitudes, where in the Fisk model the magnetic field lines at high latitudes can be connected directly to corotating regions in the solar wind at lower latitudes. However, the Fisk field leads to a more complicated form of transport equation and the implementation of this field in numerical models lies beyond the scope of this work. For more information from a cosmic ray point of view the reader is referred to Kóta and Jokipii (1997), Kóta and Jokipii (1999), van Niekerk (2000), Burger and Hattingh (2001), Burger and Hitge (2004), Krüger (2005). See also the review by Burger (2005).

2.5 Heliospheric current sheet

The HMF changes sign across a neutral sheet, thus dividing the heliosphere into two halves, a hemisphere where the HMF is directed inward, and a hemisphere where the HMF is directed outward. The transition between these hemispheres is necessarily made with a relatively thin neutral sheet region, known as the heliospheric current sheet (HCS). Because the magnetic

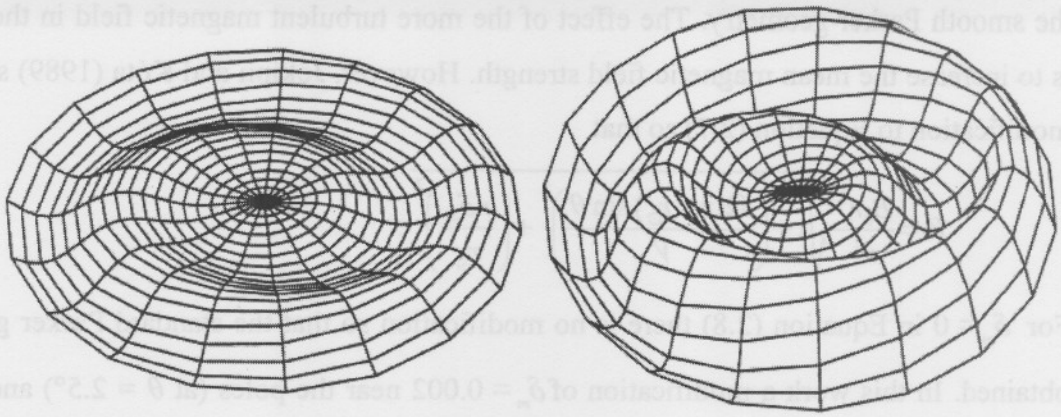

Figure 2.5. The wavy heliospheric current sheet to a radial distance of 10 AU with a tilt angle of $\alpha = 5°$ (low solar activity, left panel) and $\alpha = 20°$ (low to moderate activity, right panel). The Sun is at the centre (from Haasbroek, 1997).

and rotational axis of the Sun are not aligned, the rotation of the Sun causes the HCS to have a wavy structure. Since the Sun has typically an 11-year activity cycle, the waviness of the HCS correlates with solar activity of the Sun (see e.g., Haasbroek, 1997; Smith, 2001). This indicates that during the solar maximum the angle between the Sun's magnetic and rotational axis, known as the tilt angle α, increases to more than 70°. While during the period of lower solar activity the rotation and magnetic axis of the Sun become nearly aligned, causing relatively small neutral sheet waviness $\alpha \approx 5°$ to 10°; see Figure 2.5. The wavy structure of the HCS is convected with the solar wind outward to the outer heliosphere together with the HMF; for a review see Smith (2000). Figure 2.5 illustrates a three-dimensional idealization of two HCS configurations for distances up to 10 AU when $\alpha = 5°$ and $\alpha = 20°$.

For a constant and radial solar wind speed the HCS satisfies the following equation (Jokipii and Thomas, 1981):

$$\theta' = \frac{\pi}{2} + \sin^{-1}\left\{\sin\alpha \sin\left[\phi + \frac{\Omega(r - r_0)}{V}\right]\right\}. \tag{2.9}$$

However, for small values of α, Equation (2.9) reduces to

$$\theta' = \frac{\pi}{2} + \alpha \sin\left[\phi + \frac{\Omega(r - r_0)}{V}\right]. \tag{2.10}$$

(Hattingh, 1998). To include the polarity of the magnetic field, Equation (2.5) is modified so that

$$\mathbf{B} = A_c B_0 \left(\frac{r_0}{r}\right)^2 \left(\mathbf{e}_r - \tan\psi \mathbf{e}_\phi\right)\left[1 - 2H\left(\theta - \theta'\right)\right] \tag{2.11}$$

with θ' the polar angle of the HCS and $A_c = \pm 1$ a constant determining the polarity of the HMF which alternates every 11 years. Periods when the magnetic lines are directed outward in the northern hemisphere and inward in the southern hemisphere are called A > 0 polarity epochs with $A_c = +1$. For A < 0 periods, $A_c = -1$ and the direction of HMF reverses. The Heaviside step function in Equation (2.11) is given by

$$H(\theta - \theta') = \begin{cases} 0 \text{ when } \theta < \theta' \\ 1 \text{ when } \theta > \theta' \end{cases}. \tag{2.12}$$

This function causes the HMF to change polarity across the HCS. If this function is used directly in the numerical modulation model, the discontinuity causes severe numerical problems. To overcome this problem the Heaviside function is approximated (Hattingh, 1998; Langner, 2004) by

$$H'(\theta - \theta') \approx \tanh\left[2.75(\theta - \theta')\right]. \tag{2.13}$$

2.6 Solar cycle variation

It is well known in the field of heliospheric physics that the measurements of the sunspot numbers (shown in Figure 2.1) indicate that the Sun has a quasi-periodic cycle called a solar activity cycle. Every ~11 years the Sun moves through a period of fewer and smaller sunspots, a period called "solar minimum" and a period of larger and many more sunspots called "solar maximum" conditions.

The effects of solar cycle variations in the Sun's magnetic dipole angle have considerable effects on the structure of the HCS with the tilt angle α following the changes in magnetic dipole angle of the Sun which is nearly aligned with the Sun's rotation axis near solar minimum and almost equatorial at solar maximum (Hoeksema, 1992). Figure 2.6 shows the monthly averaged HCS tilt angles from 1976 until recently, computed with the "classic" and "new" Hoeksema models (For details see Wilcox Solar observatory with courtesy of J.T. Hoeksema: http://wso.stanford.edu). It is evident that α varies from small to a larger value between solar minimum and solar maximum ($\alpha \sim 75°$) tracing out an 11 year solar cycle. The relation between α and CR modulation has been studied in detail, see e.g., Potgieter (1984), le Roux (1990), Haasbroek (1997), Ferreira (2002), Ferreira and Potgieter (2003), Ferreira and Potgieter (2004) and references therein.

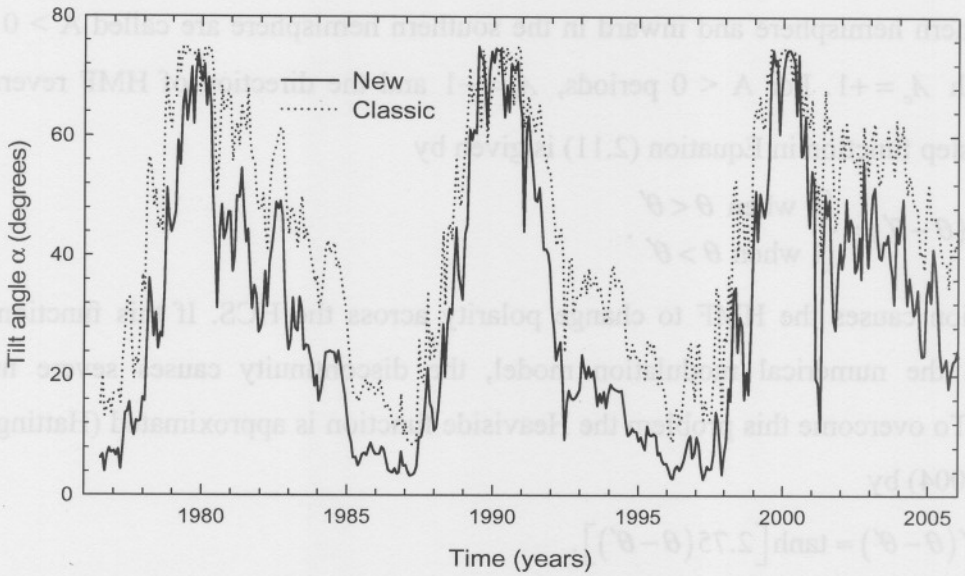

Figure 2.6. The tilt angle α from the first calculated value in 1976 until recently. Two different models for the tilt angles are shown namely "new" (solid line) and "classic" (dotted line). The "classic" model uses a line-of-sight boundary condition and the newer model uses a radial boundary condition at the photosphere. (Wilcox Solar observatory with courtesy of J.T. Hoeksema: http://wso.stanford.edu; see also Hoeksema, 1992).

It is also evident from measurements of the magnitude of the HMF at Earth (not shown) that the time-dependent magnetic field $B(t)$ varies with solar activity and shows a good correlation with α. In fact there is a factor ~ 2 increase in $B(t)$ from solar minimum to solar maximum for a solar cycle (Ferreira, 2002; Ferreira and Potgieter, 2004).

2.7 The heliosphere

The solar wind streams off of the Sun at speeds of 400-800 km.s^{-1} as discussed above, creating a magnetized "bubble" of hot plasma surrounding the Sun. This "bubble" is called the heliosphere, and it is separated from the local interstellar medium (LISM) by a heliopause (HP). The heliosphere is created because the solar wind and the HMF interact with the interstellar magnetic field and gas. The LISM consist of some combination of dust, neutral gas, plasma, magnetic fields and galactic cosmic rays (e.g., Smith, 2001). The heliosphere can be viewed as a huge laboratory where we can directly observe and measure physical parameters that cannot be scaled down to terrestrial laboratories. The heliosphere can be considered a typical, small astrosphere that may occur around other stars in the galaxy. For

additional information, see Ferreira and Scherer (2004, 2006), and Scherer and Ferreira (2005), and reference therein.

2.7.1 Geometry of the heliosphere

The geometry of the heliosphere is defined by the mutual interaction between the solar wind plasma and interstellar medium, thus a hydrodynamic model can be used to calculate the geometry of the heliosphere. Figure 2.7 shows a contour plot of the heliosphere with the computed proton number density (top) and proton speed (bottom) for an anisotropic solar wind (Ferreira and Scherer, 2004). Since the proton number density varies over several orders of magnitude, a logarithmic scale is assumed. The results are shown in the rest frame of the Sun, where its motion relative to the LISM appears as an interstellar wind blowing from right to left. The dashed lines indicate the position of the termination shock (TS) and HP. As shown both the TS radius, r_s, and HP radius, r_b, are functions of polar angle and are elongated

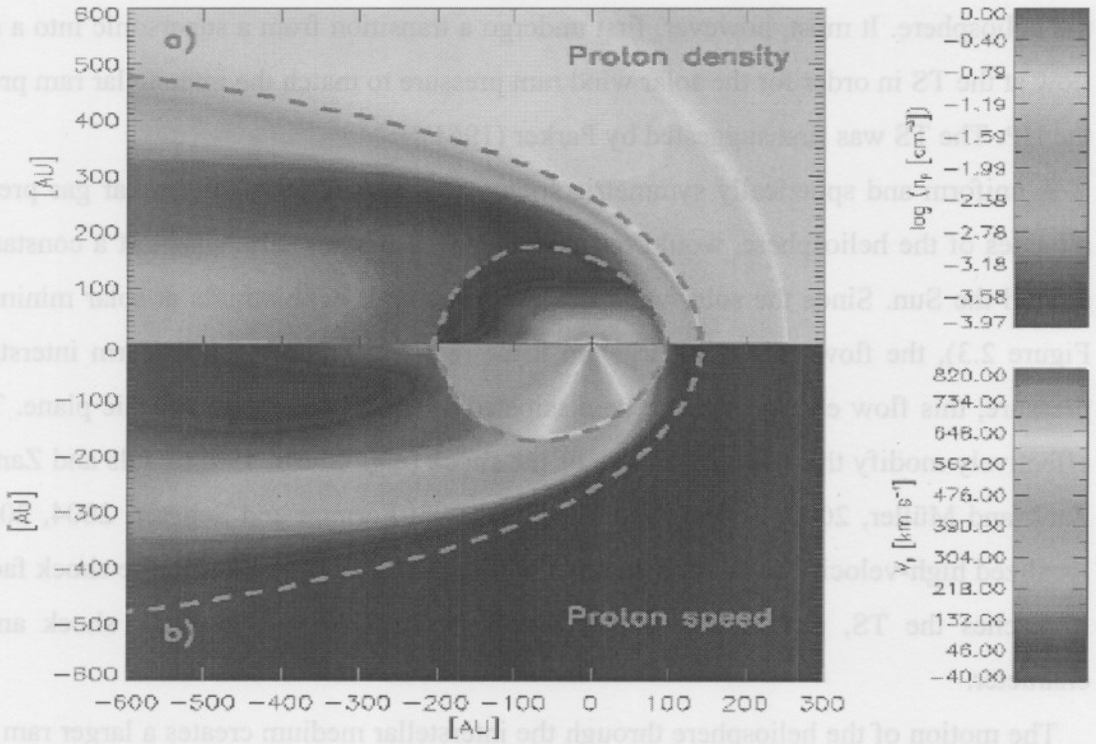

Figure 2.7. Contour plot of the heliosphere showing the computed proton number density (top) and proton speed (bottom). Shown by the dashed lines are the positions of the termination shock (dashed circle) and the heliopause (from Ferreira and Scherer, 2004).

along the Sun's polar axis. This elongation is due to an increase in solar wind ram pressure in the polar regions (see also Pauls and Zank, 1996, and Zank 1999). From Figure 2.7 follows that in the equatorial regions r_s = 94 AU and r_b = 140 AU in the nose direction, while at the poles r_s = 157 AU and r_b = 244 AU; r_s = 206 AU in the tail direction, but there is no well defined distance to the HP as the heliosphere is most probably an open structure in the tail direction as seen from Figure 2.7.

2.7.2 Termination shock

As the heliosphere moves through the LISM it forces the plasma component of the LISM to flow around it. At large radial distances the LISM pressure causes the supersonic solar wind to decrease to subsonic speeds. A supersonic flow cannot decelerate into a subsonic flow in a continuous way. Thus, the supersonic flow energy must be dissipated discontinuously. This discontinuity in supersonic flow to subsonic flow is called a shock.

The supersonic solar wind, originating on the Sun, must merge with the LISM surrounding the heliosphere. It must, however, first undergo a transition from a supersonic into a subsonic flow at the TS in order for the solar wind ram pressure to match the interstellar ram pressure at the HP. The TS was first suggested by Parker (1961).

A uniform and spherically symmetric solar wind, and uniform interstellar gas pressure on all sides of the heliosphere, would result in a spherical symmetric shock at a constant radius around the Sun. Since the solar wind velocity rises with heliolatitude at solar minimum (see Figure 2.3), the flow energy is larger in these regions. Assuming a uniform interstellar gas pressure, this flow energy will not be dissipated as quickly as in the ecliptic plane. This will effectively modify the spherical nature of the shock (e.g., Suess, 1993; Pauls and Zank, 1997; Zank and Müller, 2003; Scherer and Ferreira, 2005; Ferreira and Scherer, 2004, 2006). The localized high-velocity solar wind streams will cause localized bulges in the shock face where it reaches the TS, pushing the shock further back. This will give the shock an uneven character.

The motion of the heliosphere through the interstellar medium creates a larger ram pressure in the direction of motion and a smaller pressure in the opposite direction. This means that the flowing energy of the solar wind will be dissipated faster in the direction of motion than in the opposite direction, and thus the shock face will be nearer to the Sun in the direction of motion

and further out on the opposite side. A spherical shock will thus be deformed into an ovoid (see e.g., Scherer and Fahr, 2003; Zank and Müller, 2003, Langner et al., 2006a).

There is a reasonable consensus that the TS is in the vicinity of 90 ± 5 AU in the equatorial plane (e.g., Stone and Cummings, 2001) and in the heliospheric nose direction. Indeed V1 crossed the TS at a distance of 94 AU in the nose direction in December 2004 (Stone et al., 2005); details in section 2.9.2.

However, such asymmetries mentioned above will not be included in this dissertation so that a spherical TS is assumed and it is taken to be at 90 AU from the Sun in the nose and tail directions. As was illustrated by Langner et al. (2006a), this assumption is quite reasonable.

2.7.3 Heliosheath

The solar wind and the LISM plasma flows are separated by the HP which is considered for practical reasons the boundary of the heliosphere. The position of the HP is less certain, ~ 30 – 50 AU beyond the TS in the nose direction, while in the tail direction the heliosphere is most probably an open structure (e.g., Scherer and Fahr, 2003; Zank and Müller, 2003; Ferreira et al., 2004; Scherer and Ferreira, 2005). The region between the TS and the HP is the inner heliosheath that contains hot shocked plasma of solar origin that is deflected from its initial radial expansion and forms an extended heliotail in the downwind direction. In the inner heliosheath the wind is slower, hotter and denser as it interacts with the surrounding interstellar matter. The magnetic field is still frozen into the solar wind plasma and increases in proportion to the increase in plasma density in the inner heliosheath. The LISM plasma also undergoes a weak shock transition at the bow shock ahead of the heliopause. The LISM flow is diverted around this obstacle in the region behind the bow shock forming the outer heliosheath. In this work the inner heliosheath is simply referred to as the heliosheath.

There is growing evidence that a significant, or even dominant part of the modulation of galactic cosmic rays may occur in the heliosheath (McDonald et al. 2000; Webber and Lockwood, 2001; Langner and Potgieter, 2005). The Voyager 1 spacecraft is presently exploring this region.

2.8 Charged particles in the heliosphere

CRs were discovered by Victor Hess during the historic balloon flights in 1911 and 1912, where it was shown that the origin of these particles is extraterrestrial (for a review see e.g.

Simpson, 1998 and Fichtner, 2001). CRs travel through interstellar space and the heliosphere, filter through the Earth's atmosphere to be detected at ground level. Those that arrive at Earth are mainly composed of ~ 98% nuclei, stripped of all their orbital electrons and ~ 2% electrons and positrons (e.g., Longair, 1990; Simpson, 1992).

In the heliosphere three main populations of CRs are found. They are galactic CRs, the anomalous component and energetic particles, all discussed below.

2.8.1 Galactic cosmic rays

Galactic CRs originating from far outside our solar system. It is believed that the energy transfer processes during supernova explosions in the galaxy are major sources of these particles (see e.g. Casedei and Bindi 2004; Kobayashi et al. 2004). Experimental evidence of this was earlier found by e.g. Koyama et al. (1995) and confirmed by Tanimori et al. (1998). On their way to Earth these particles are to some extent reaccelerated at the TS (e.g., Langner et al., 2006a).

2.8.2 Anomalous cosmic rays

The discovery of the anomalous component of cosmic rays (ACRs) by Garcia-Munoz et al. (1973a, 1973b, 1973c) provided a powerful new tool with which the heliosphere can be probed. Soon thereafter, in addition to Helium, anomalous Oxygen (Hovestadt et al., 1973), Nitrogen (McDonald et al., 1974), and Neon (Von Rosenvinge and McDonald, 1975) were observed. Fisk et al. (1974) recognized that these elements all have high first ionization potentials and, therefore, they proposed that these elements enter the heliosphere as interstellar neutrals because of the movement of the heliosphere through interstellar space. These elements then penetrate deeply into the heliosphere before they become singly ionized by charge exchange with the solar wind ions, electron collisions, or photo-ionization. These singly ionized atoms are then picked up by the solar wind and convected outwards towards the outer heliosphere, where they are accelerated at the solar wind termination shock (e.g. through a process of first order Fermi acceleration) gaining energy by multiple crossing of the TS. This process was first suggested by Pesses et al. (1981) and illustrated by Jokipii (1986). Some of these accelerated particles may then diffuse into the heliosphere, where they are modulated by the same processes as the galactic component to form the anomalous component of the cosmic rays.

Möbius et al. (1985) obtained the first conclusive evidence of the solar wind picking up the singly ionized Helium (He^+), using a time-of-flight spectrometer. According to Möbius (1986) the kinetic energy of these pick-up ions varies from basically zero to approximately four times the flow energy of the solar wind.

Diffusive shock acceleration (first-order Fermi acceleration) still remains the widely accepted mechanism for the acceleration of pick-up ions to form the ACRs. However, the process of exactly how the pick-up ions are injected into the acceleration mechanism at the TS remains a topic of study. For reviews, see Zank (1999), Zank et al. (2001) and Fichtner (2001). Recent observations by V1 also indicate that the ACRs may also get accelerated beyond the TS.

2.8.3 Energetic particles

The solar system is pervaded by energetic particles, in addition to those discussed above, from various sources. Energetic storm particles (ESP) of various ions species have been shown to comprise of suprathermal seed ions accelerated by traveling interplanetary shocks. They typically exhibit spectral rollovers at 0.1 to 10 MeV nucleon^{-1} (Desai et al., 2004; Gosling et al., 1981). Solar energetic particles (SEPs) originate from solar flares (e.g., Smith et al., 2003). Coronal mass ejections (CMEs) and shocks in the interplanetary medium can also produce energetic particles. SEPs may have energies up to several hundred MeV but are usually observed at Earth only for several hours when occurring. These particles are disregarded for the purpose of this study. For a review, see Cliver (2000).

It was discovered with the Jupiter fly-by of the Pioneer 10 spacecraft in 1973 that the Jovian magnetosphere, situated at ~ 5 AU in the equatorial region, is a relatively strong source of electrons with energies up to at least ~ 30 MeV (Simpson et al. 1974; Teegarden et al. 1974; Chenette et al. 1974; Heber et al., 2003). These electrons, when released into the interplanetary medium, dominate the low energy electron intensities within the first ~ 10 AU (e.g., Jokipii and Kóta, 1991; Moraal et al., 1991; Haasbroek, 1997; Haasbroek et al., 1997a, 1997b; Ferreira et al., 2001a, 2001b; Ferreira, 2002; Moeketsi, 2004). These particles are also disregarded in this study because the focus is on galactic and anomalous CRs and the outer heliosphere.

2.9 Space missions

One of the most important aspects in the study of the heliospheric modulation of the CRs is the accumulation of data from *in situ* observations. In this section the Ulysses and Voyager space missions are briefly discussed.

2.9.1 The Ulysses mission

The Ulysses spacecraft was launched on 6 October 1990. It was the first spacecraft to undertake measurements above the ecliptic plane and over the polar regions of the Sun, thus obtaining first hand knowledge concerning the high latitudes of the inner heliosphere (< 5 AU).

After its launch, the spacecraft stayed close to the ecliptic plane to reach Jupiter (at ~ 5 AU), from where it started to move to higher latitudes south of the ecliptic plane. In mid 1994 the highest southern point was reached at minimum solar activity. From there, Ulysses moved to the northern polar region which was reached in mid 1995 and returned to the equatorial plane again in 1998. After ~1998 Ulysses started the second out-of-ecliptic orbit moving into the southern heliospheric polar regions. It crossed the equatorial plane in May 2001, and on 5 February 2004 the spacecraft was again closest to Jupiter.

The Ulysses mission is highly successful and has contributed significantly to the current knowledge regarding the inner heliosphere. See the following publications for an overview: Marsden (1995; 2001), Balogh et al. (2001) and Smith et al. (2003).

2.9.2 Voyager missions

The Voyager program consisted of a pair of unmanned scientific probes, Voyager 1 and Voyager 2, launched in 1977. They were sent to study Jupiter and Saturn and their satellites and magnetospheres. Voyager 2 also examined Uranus and Neptune. However, the mission planners always had in mind a continued mission. The two Voyager spacecrafts were set to explore the Sun's environment from different heliographic latitudes simultaneously by sending V1 to the north while Voyager 2 was sent to the southern hemisphere both in the general direction of the nose of the heliosphere. Both missions revealed large amounts of information about the magnetic field, solar wind and CRs.

Voyager 1 and 2 are traveling at the speeds of 3.6 and 3.1 AU per year respectively (Stone, 2004). V1 crossed the TS on 16 December 2004 (Stone et al., 2005; Decker et al., 2005) with the HP a still unknown distance ahead. Periodic contact has been maintained with both probes to monitor conditions in the outer expanses of the solar system. The crafts' radioactive power sources are still producing electrical energy, fuelling hopes of locating the HP in the next decade.

Table 2.1 shows the present heliospheric positions of both Voyager 1 and Voyager 2. Unexpected discoveries have unfolded as Voyager 1 explored the heliosheath region and when Voyager 2 crosses the TS more discoveries are expected. The crossing of the TS by Voyager 2 will give additional information of the TS structure and the heliosheath.

Table 2.1. Voyager positions in 2006 (*http://nssdc.gsfc.nasa.gov/space/helios/heli.html*)

Spacecraft	Month	Year	Distance (AU) from the Sun	Latitude (degrees)	Longitude (degrees)
Voyager 1	June	2006	99.4	34.2	172.7
Voyager 2	June	2006	79.8	-26.7	216.0

2.10 Summary

In this chapter a brief overview was given of the concepts used in the heliospheric modulation of cosmic rays. These concepts include the nature of cosmic rays, the heliosphere and its geometry, the solar wind, the heliospheric magnetic field, the solar cycle and the heliospheric current sheet. The Voyager and Ulysses space missions were briefly discussed.

In the next chapter an overview is given of the modulation model used for this study and the supporting theory, particularly a discussion regarding the transport equation, as well as the diffusion tensor.

Chapter 3

The transport equation and numerical models

3.1. Introduction

Galactic CRs have to cross various heliospheric boundaries and regions (see Figure 2. 7) on their way to a point of observation, which can be Earth or one of the current fleet of spacecraft. Beyond the outer boundary of the heliosphere, the Sun's magnetic field and solar wind can no longer influence CRs. Within this boundary, modulation takes place as CR intensities decrease relative to the interstellar values. This process is also strongly time and energy dependent. Global modulation within the heliosphere is theoretically described by the Parker transport equation (TPE).

In this chapter a discussion of the transport processes as they occur in the TPE is given, together with a short overview of existing modulation models as well as a thorough discussion of the model that is used for this work.

3.2 The Parker transport equation

The modulation of CRs is described by the TPE which was developed by Parker (1965). To verify all the transport processes present in the TPE, this equation was re-derived by Gleeson and Axford (1967) and refined by Gleeson and Axford (1968) and Jokipii and Parker (1970). The TPE is given by

$$\frac{\partial f}{\partial t} = -\mathbf{V}.\nabla f + \nabla.(\mathbf{K}.\nabla f) + \frac{1}{3}(\nabla.\mathbf{V})\frac{\partial f}{\partial \ln P} + Q_{source}, \tag{3.1}$$

where $f(\mathbf{r},P,t)$ is the omni-directional cosmic ray distribution function dependent on position $\mathbf{r}$, rigidity P, and time t. The rigidity is defined as the momentum per charge for a given species of particles, and is given by $P = pc/q$ where p is the particle's momentum, q the particle's charge and c the speed of light in space. $\mathbf{V}$ is the solar wind velocity discussed in Chapter 2 and $\mathbf{K}$ is the diffusion tensor. The TPE includes the following processes:

(1) The term on the left describes the changes in the CR distribution with time.

(2) The first term on the right describes the outward particle convection due to the radially outward solar wind.

(3) The second term on the right describes spatial diffusion parallel and perpendicular to the average heliospheric magnetic field (HMF), particle drifts due to gradients and curvature of the HMF, and any abrupt changes like the heliospheric current sheet (HCS).

(4) The third term describes energy changes in the form of adiabatic cooling or heating, and the acceleration of particles at shocks.

(5) The final term describes possible sources of CRs inside the heliosphere, e.g. the anomalous proton source.

The transport equation in a spherical coordinate system rotating with the Sun is given by

$$\begin{aligned}\frac{\partial f}{\partial t} &= \left[\frac{1}{r^2}\frac{\partial}{\partial r}\left(r^2 K_{rr}\right)+\frac{1}{r\sin\theta}\frac{\partial}{\partial\theta}(K_{\theta r}\sin\theta)+\frac{1}{r\sin\theta}\frac{\partial K_{\phi r}}{\partial\phi}-V\right]\frac{\partial f}{\partial r}\\ &+\left[\frac{1}{r^2}\frac{\partial}{\partial r}\left(rK_{r\theta}\right)+\frac{1}{r^2\sin\theta}\frac{\partial}{\partial\theta}(K_{\theta\theta}\sin\theta)+\frac{1}{r^2\sin\theta}\frac{\partial K_{\phi\theta}}{\partial\phi}\right]\frac{\partial f}{\partial\theta}\\ &+\left[\frac{1}{r^2\sin\theta}\frac{\partial}{\partial r}\left(rK_{r\phi}\right)+\frac{1}{r^2\sin\theta}\frac{\partial K_{\theta\phi}}{\partial\theta}+\frac{1}{r^2\sin^2\theta}\frac{\partial K_{\phi\phi}}{\partial\phi}\right]\frac{\partial f}{\partial\phi}\\ &+K_{rr}\frac{\partial^2 f}{\partial r^2}+\frac{K_{\theta\theta}}{r^2}\frac{\partial^2 f}{\partial\theta^2}+\frac{K_{\phi\phi}}{r^2\sin^2\theta}\frac{\partial^2 f}{\partial\phi^2}+\frac{2K_{r\phi}}{r\sin\theta}\frac{\partial^2 f}{\partial r\partial\phi}\\ &+\frac{1}{3r^2}\frac{\partial}{\partial r}(r^2V)\frac{\partial f}{\partial\ln P}+Q_{source},\end{aligned} \tag{3.2}$$

with a radial solar wind speed V and where $K_{rr}, K_{r\theta}, K_{r\phi}, K_{\theta r}, K_{\theta\theta}, K_{\theta\phi}, K_{\phi r}, K_{\phi\theta}$ and $K_{\phi\phi}$ are the elements of the diffusion tensor $\mathbf{K}$ in Equation (3.1) which will be discussed in section 3.4. The position is described in terms of radial distance r, polar angle θ, and the azimuthal angle ϕ.

For clarity on the role of diffusion, drifts, convection, and adiabatic energy loss, the TPE is written as follows:

$$\begin{aligned}\frac{\partial f}{\partial t} &= \overbrace{\left[\frac{1}{r^2}\frac{\partial}{\partial r}\left(r^2 K_{rr}\right)+\frac{1}{r\sin\theta}\frac{\partial K_{\phi r}}{\partial\phi}\right]\frac{\partial f}{\partial r}+\left[\frac{1}{r^2\sin\theta}\frac{\partial}{\partial\theta}(K_{\theta\theta}\sin\theta)\right]\frac{\partial f}{\partial\theta}}^{diffusion}\\ &+\overbrace{\left[\frac{1}{r^2\sin\theta}\frac{\partial}{\partial r}\left(rK_{r\phi}\right)+\frac{1}{r^2\sin^2\theta}\frac{\partial K_{\phi\phi}}{\partial\phi}+\Omega\right]\frac{\partial f}{\partial\phi}}^{diffusion}\\ &+\overbrace{\left[K_{rr}\frac{\partial^2 f}{\partial r^2}+\frac{K_{\theta\theta}}{r^2}\frac{\partial^2 f}{\partial\theta^2}+\frac{K_{\phi\phi}}{r^2\sin^2\theta}\frac{\partial^2 f}{\partial\phi^2}+\frac{2K_{r\phi}}{r\sin\theta}\frac{\partial^2 f}{\partial r\partial\phi}\right]}^{diffusion}\end{aligned}$$

$$+\overbrace{\left[\left[-\langle v_d\rangle_r\right]\frac{\partial f}{\partial r}+\left[-\frac{1}{r}\langle v_d\rangle_\theta\right]\frac{\partial f}{\partial \theta}+\left[-\frac{1}{r\sin\theta}\langle v_d\rangle_\phi\right]\frac{\partial f}{\partial \phi}\right]}^{drift}$$

$$\overbrace{-V\frac{\partial f}{\partial r}}^{convection}+\overbrace{\frac{1}{3r^2}\frac{\partial (r^2V)}{\partial r}\frac{\partial f}{\partial lnP}}^{adiabatic\ energy\ changes}+\overbrace{Q_{source}}^{sources}. \qquad (3.3)$$

The equatorial plane is specified at $\theta = 90°$.

3.3 Particle drifts

Although particle drifts were included in the original transport equation they had been neglected until Jokipii et al. (1977) pointed out that the inclusion of drifts could alter modulation, especially since drifts are sensitive to the polarity of the HMF and to the charge leading to a charge asymmetry. The smooth global or background magnetic field affects the CR transport by contributing drift motions associated with the gradients in field magnitude, the curvature of the field and any abrupt changes in the field direction, such as caused by the HCS. The components of the drift velocity as they appear in Equation (3.3) in three dimensions (e.g., Hattingh, 1998) are:

$$\langle v_d\rangle_r = -\frac{A}{r\sin\theta}\frac{\partial}{\partial\theta}(\sin\theta K_{\theta r}), \qquad (3.4)$$

$$\langle v_d\rangle_\theta = -\frac{A}{r}\left[\frac{1}{\sin\theta}\frac{\partial}{\partial\phi}(K_{\phi\theta})+\frac{\partial}{\partial r}(rK_{r\theta})\right],$$

$$\langle v_d\rangle_\phi = -\frac{A}{r}\frac{\partial}{\partial\theta}(K_{\theta\phi}),$$

or alternatively

$$\langle v_d\rangle = \nabla\times K_A\mathbf{e}_B, \qquad (3.5)$$

here $A = sign(Bq)$ determines the direction of the drifts of the charged particles in the heliosphere that depend on the geometry of the HMF, $\mathbf{e}_B = \mathbf{B}_m / B$, and K_A is the "drift" coefficient that is discussed in detail below.

For the A > 0 polarity cycle, positively charged particles drift from the polar region of the heliosphere down to the equatorial regions and they are largely insensitive to the conditions in the equatorial region, e.g. changes in HCS. For A < 0 polarity cycle, positively charged particles drift primarily in along the HCS and outwards over the polar regions and are

sensitive to changes in the tilt angle of the HCS. These drift directions are shown in Figure 3.1 for protons. For negatively charged particles the drift is in the opposite direction.

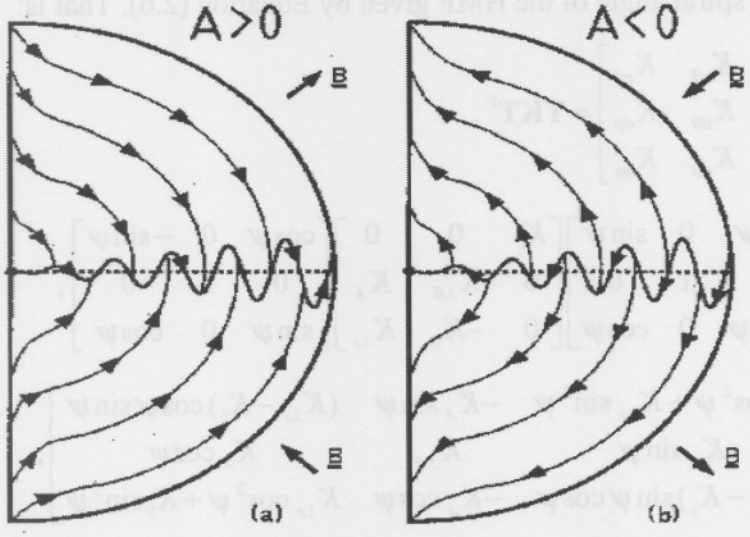

Figure 3.1. The drift direction of protons caused by gradients, curvature and the current sheet of the HMF for (a) the A > 0 HMF, and (b) the A < 0 HMF polarity. The electron drift directions are opposite of the proton drift directions (from Jokipii and Thomas, 1981).

3.4 The elements of the diffusion tensor

The transport of charged particles in the heliosphere is determined by a heliospheric diffusion tensor. This diffusion tensor **K**, as introduced in the TPE above, is given by

$$\mathbf{K} = \begin{bmatrix} K_{\parallel} & 0 & 0 \\ 0 & K_{\perp\theta} & K_A \\ 0 & -K_A & K_{\perp r} \end{bmatrix}, \tag{3.6}$$

where $K_{\parallel}$ is the diffusion coefficient parallel to the mean HMF, $K_{\perp\theta}$ and $K_{\perp r}$ denote the diffusion coefficients perpendicular to the mean HMF in the polar and radial direction respectively, and the anti-symmetric element K_A describes particle drifts which include gradient, curvature and heliospheric current sheet drift in the large scale HMF as described above. The tensor given by Equation (3.6) emerges naturally in the development of the TPE using the Fokker-Planck equation (see e.g., Stawicki, 2003), or by using physical arguments as in Jokipii and Parker (1970).

The elements of the diffusion tensor with respect to heliocentric spherical coordinates are obtained by using the transformation matrix

$$\mathbf{T}=\begin{bmatrix}\cos\psi & 0 & \sin\psi\\ 0 & 1 & 0\\ -\sin\psi & 0 & \cos\psi\end{bmatrix}, \tag{3.7}$$

where ψ is the spiral angle of the HMF given by Equation (2.6). That is:

$$\begin{bmatrix}K_{rr} & K_{r\theta} & K_{r\phi}\\ K_{\theta r} & K_{\theta\theta} & K_{\theta\phi}\\ K_{\phi r} & K_{\phi\theta} & K_{\phi\phi}\end{bmatrix}=\mathbf{TKT}^{T}, \tag{3.8}$$

$$=\begin{bmatrix}\cos\psi & 0 & \sin\psi\\ 0 & 1 & 0\\ -\sin\psi & 0 & \cos\psi\end{bmatrix}\begin{bmatrix}K_{\parallel} & 0 & 0\\ 0 & K_{\perp\theta} & K_{A}\\ 0 & -K_{A} & K_{\perp r}\end{bmatrix}\begin{bmatrix}\cos\psi & 0 & -\sin\psi\\ 0 & 1 & 0\\ \sin\psi & 0 & \cos\psi\end{bmatrix}, \tag{3.9}$$

$$=\begin{bmatrix}K_{\parallel}\cos^{2}\psi+K_{\perp r}\sin^{2}\psi & -K_{A}\sin\psi & (K_{\perp r}-K_{\parallel})\cos\psi\sin\psi\\ K_{A}\sin\psi & K_{\perp\theta} & K_{A}\cos\psi\\ (K_{\perp r}-K_{\parallel})\sin\psi\cos\psi & -K_{A}\cos\psi & K_{\perp r}\cos^{2}\psi+K_{\parallel}\sin^{2}\psi\end{bmatrix}, \tag{3.10}$$

where the superscript T in Equation (3.8) denotes the transpose of the matrix. A theoretical challenge in modulation studies is to determine the four elements $K_{\parallel}$, $K_{\perp r}$, $K_{\perp\theta}$ and K_{A} as a function of rigidity (energy), position and time.

3.4.1 Diffusion theory

This section gives a theoretical background on certain aspects of the diffusion theory without going into the detailed theory.

The diffusive transport of charged particles in the heliosphere is determined by the parallel and perpendicular diffusion coefficients. The parallel diffusion coefficient ($K_{\parallel}$) describes the transport of the cosmic rays along the HMF lines and the perpendicular diffusion coefficient ($K_{\perp}$) describes the transport of the charged particles perpendicular to the HMF. These processes can be described by quasi-linear theory (QLT) (see e.g. Jokipii, 1966; Hasselmann and Wibberenz, 1968), with the parallel mean free path ($\lambda_{\parallel}$) given by

$$\lambda_{\parallel}=\frac{3v}{2}\int_{0}^{1}\frac{\left(1-\mu^{2}\right)^{2}}{\Phi(\mu)}d\mu, \tag{3.11}$$

with v the speed of the particle, μ the cosine of the pitch angle and $\Phi(\mu)$ the Fokker Planck coefficient for pitch-angle scattering (Hasselmann and Wibberenz, 1970; Jokipii,

1971; Earl, 1974; Stawicki, 2003). The relationship between the parallel mean free path ($\lambda_{\parallel}$) and the parallel diffusion coefficient is given by

$$\lambda_{\parallel} = \frac{3}{v} K_{\parallel} . \tag{3.12}$$

The calculation of $\Phi(\mu)$ in Equation (3.11) needs as input the power spectrum of the magnetic field fluctuations which can be divided into three ranges namely the energy range, where the power spectrum variation is independent of the wave number *k*, the inertial range, where it is proportional to $k^{-5/3}$, and a dissipation range where it is proportional to k^{-3} (see e.g. Bieber et al., 1994).

The dissipation range plays a significant role in the resonant scattering of low energy particles where the pitch angles of these particles approach 90°. In the original derivation of $\lambda_{\parallel}$ the dissipation range was neglected (see e.g. Jokipii, 1966). It soon became evident from plasma wave observation in the solar wind (see e.g. Coroniti et al., 1982) that the magnetic fluctuation spectra typically exhibit a dissipation range. By neglecting the dissipation range, $\lambda_{\parallel}$ is too small for lower rigidities and has the wrong rigidity dependence (Bieber et al., 1994). However, this $\lambda_{\parallel}$ can be applied to high energy proton modulation in the heliosphere because cosmic ray protons experience large adiabatic energy changes below ~300 MeV and at these energies the proton modulation seems unaffected by changes in $\lambda_{\parallel}$ (see e.g. Potgieter, 1984, 1996, 2000).

Including the dissipation range, QLT predicts a $\lambda_{\parallel}$ which is infinite. This is because $\Phi(\mu)$ goes more rapidly to zero without dissipation range as the pitch angle approaches 90°. When $\Phi(\mu) \rightarrow 0$, it follows from Equation 3.11 that $\lambda_{\parallel} \rightarrow \infty$. A higher order theory is therefore needed. Several mechanisms have been proposed to overcome this problem. Bieber et al. (1994) calculated $\lambda_{\parallel}$ shown in Figure 3.2 by using two models for dynamical turbulence, namely the damping model and the random sweeping model. The left panels show the prediction for slab geometry, while the right panels show the predictions for slab and 2D geometry. Of particular interest from Figure 3.2 is that $\lambda_{\parallel}$ for protons (dashed line) and electrons (solid lines) is fundamentally different at low and intermediate rigidities (< 50 MV) due to an explicit speed dependence of $\lambda_{\parallel}$. The inclusion of dynamical turbulence causes $\Phi(\mu)$ not to decrease to zero for small μ, which leads to a finite $\lambda_{\parallel}$ at lower energies (see e.g., Hattingh, 1998).

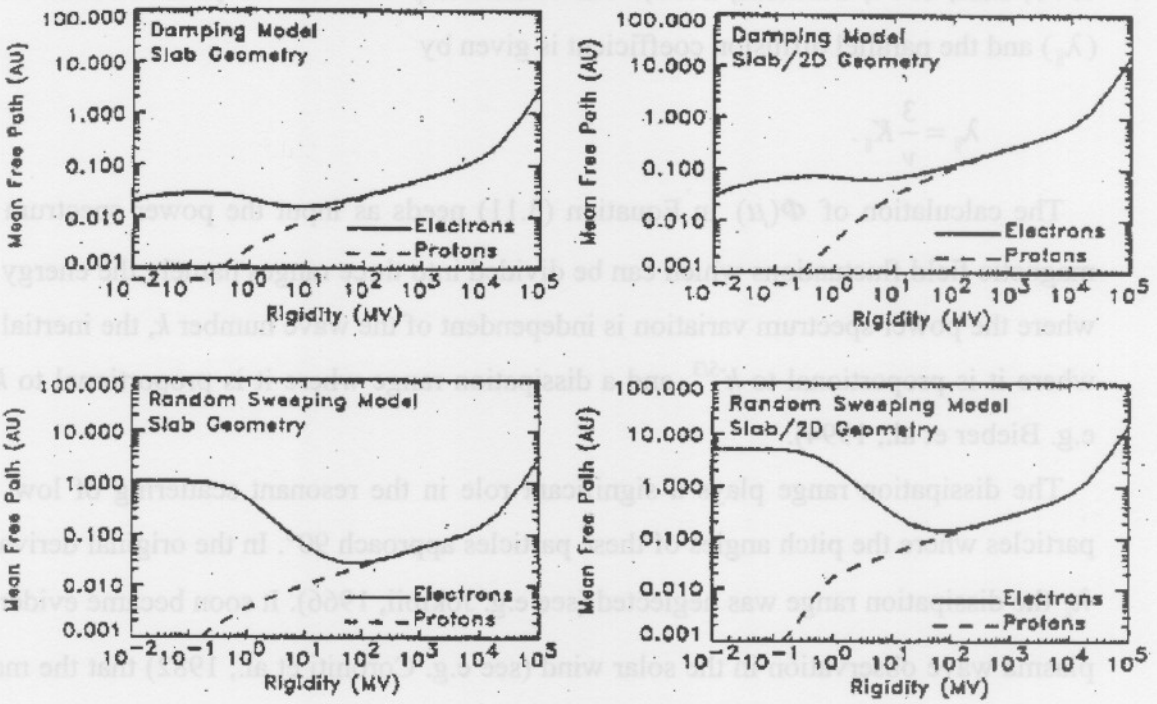

Figure 3.2. The parallel mean free path at Earth as predicted by the two models for dynamical turbulence (Bieber et al., 1994). The two top panels correspond to damping model and two bottom panels to the random sweeping model. The left panels show the predictions only for slab geometry and the two right panels for the composite slab geometries. (From Dröge, 2000).

Most of the recent work on the theory of diffusion coefficients has been done on perpendicular diffusion, because the theory behind parallel diffusion and drifts are thought to be in good shape (Teufel and Schlickeiser, 2002, 2003; Teufel et al., 2003; Stawicki, 2003). For this reason authors, using modulation models, usually scale $K_\perp$ as proportional to $K_\parallel$ (Jokipii and Kóta, 1995; Potgieter, 1996; Burger et al., 2000; Ferreira, 2002; Langner, 2004). For recent reviews on $K_\parallel$, see e.g., Dröge (2005) and McKibben (2005).

3.4.2 Cosmic ray approach

In contrast to the turbulence approach, a large set of cosmic ray observations is used to determine the rigidity and spatial dependence of the diffusion coefficients. However, modelers use also information from the turbulence approach to restrict the choice in parameter space, see e.g. Burger et al. (2000).

In this section the diffusion coefficients used in this work are discussed and illustrated and it is shown how they are constructed to be applicable to the entire heliosphere from the cosmic ray point of view.

The diffusion coefficients of special interest for this study after equating terms in Equation (3.8) and Equation (3.10) are

$$K_{rr} = K_{\parallel} \cos^2 \psi + K_{\perp r} \sin^2 \psi , \tag{3.13}$$

$$K_{\theta\theta} = K_{\perp\theta} , \tag{3.14}$$

$$K_{\theta r} = K_A \sin \psi , \tag{3.15}$$

with K_{rr} and $K_{\theta\theta}$ the effective diffusion coefficients in the radial and heliospheric polar direction, respectively, and $K_{\theta r}$ the diffusion coefficient caused by drifts.

Figure 3.3 shows for illustrative purposes $\cos^2 \psi$ and $\sin^2 \psi$ in Equation (3.13) as a function of radial distance for the equatorial plane (θ = 90°) and in the polar regions (θ = 10°). From Figure 3.3 it follows that $\cos^2 \psi$ decreases with increasing radial distance for

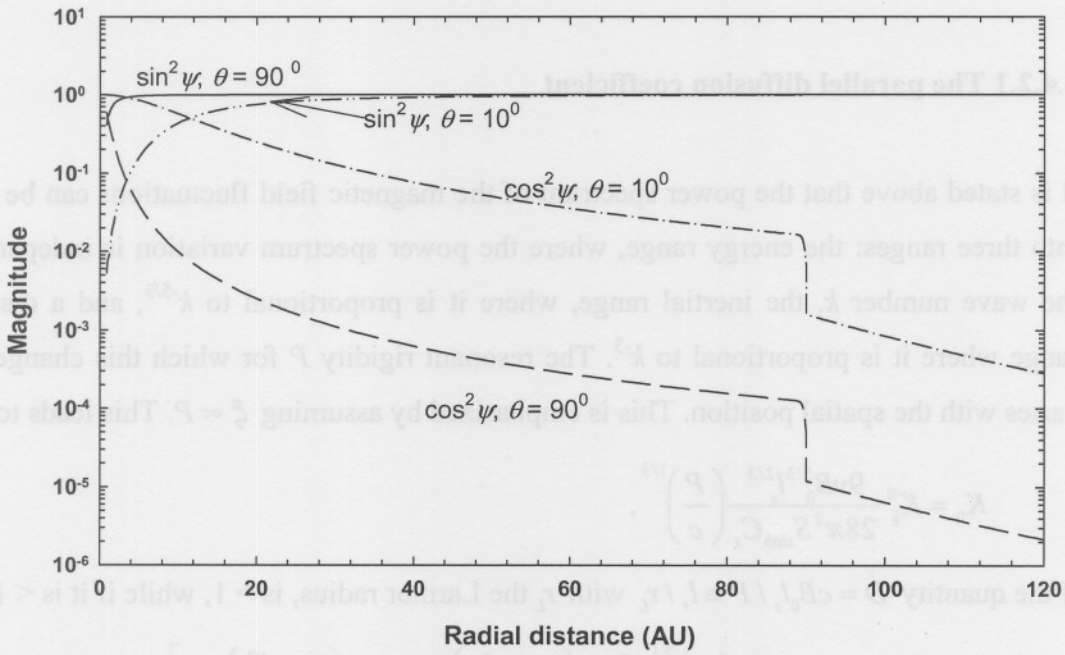

Figure 3.3. The values of $\cos^2 \psi$ and $\sin^2 \psi$ in Equation (3.13) as a function of radial distance in the equatorial plane (θ = 90°) and for the polar regions (θ = 10°). Here ψ is the spiral angle of the HMF as defined by Equation (2.6). The TS is at 90 AU with the HP at 120 AU.

polar regions and even more significantly for the equatorial regions. On the other hand, $\sin^2\psi$ stays almost constant for most of the heliosphere, except for the inner heliosphere where it rapidly changes for both the polar and equatorial regions. This indicates that, although $K_{\perp r}$ is usually ≤ 3% of $K_{\parallel}$, it dominates the term K_{rr} in the outer heliospheric regions. On the other hand, $K_{\parallel}$ dominates K_{rr} in the inner heliosphere and in the polar regions.

The expressions for the diffusion coefficients $K_{\parallel}$, $K_{\perp}$, and K_A which have been used in this work are similar to those that have been given by Burger et al. (2000) for a steady-state model, except for minor changes to their values that are caused by the introduction of the TS in this model (see also Langner, 2004). These changes are insignificant for both polarity cycles at Earth but become more significant with increasing radial distance. They are based and motivated on diffusion (Burger and Hattingh, 1998) and turbulence theory (Zank et al., 1996), but have been adapted to reflect some of the results of numerical simulations by Giacalone and Jokipii (1999, 2001). For the diffusion parallel to the magnetic field QLT and slab/2D geometry (20%/80%) for the turbulence is used.

3.4.2.1 The parallel diffusion coefficient

It is stated above that the power spectrum of the magnetic field fluctuations can be divided into three ranges: the energy range, where the power spectrum variation is independent of the wave number k, the inertial range, where it is proportional to $k^{-5/3}$, and a dissipation range where it is proportional to k^{-3}. The resonant rigidity P for which this change occurs varies with the spatial position. This is emphasized by assuming $\xi \propto P$. This leads to

$$K_{\parallel} = K_{\parallel}^{0} \frac{9 v B_0^{5/3} l_s^{2/3}}{28\pi^2 S_{slab} C_s} \left(\frac{P}{c}\right)^{1/3}, \tag{3.16}$$

if the quantity $D = cB_0 l_s / P \equiv l_s / r_L$ with r_L the Larmor radius, is > 1, while if it is < 1:

$$K_{\parallel} = K_{\parallel}^{0} \frac{v}{8\pi^2 S_{slab} C_s l_s} \left(\frac{P}{c}\right)^2 \left[\frac{\xi_0}{4\xi} + \left(2 + \frac{\xi}{2\xi_0}\right) D^2 - \frac{1}{12}\left(\frac{8}{7} + \frac{\xi^3}{\xi_0^3}\right) D^4\right] \text{ if } \xi D \le 1, \tag{3.17}$$

$$K_{\parallel} = K_{\parallel}^{0} \frac{v B_0}{4\pi^2 S_{slab} C_s} \left(\frac{P}{c}\right) \left[\frac{1}{3} + D - \frac{1}{12} D^3\right] \text{ if } \xi D > 1. \tag{3.18}$$

In these expressions, $K_{\parallel}^{0} = 0.9$ is a dimensionless constant for all tilt angles and both polarity cycles, B_0 is the magnitude of the average magnetic field, $l_s = 0.031(l/l_e)\mathrm{AU} = 4.55\times10^{9}(l/l_e)\mathrm{m}$ is the wavelength for slab turbulence at the break point between the energy and the inertial range of the magnetic field power spectrum, l is the correlation length of the magnetic field with $l_e = 0.023\mathrm{AU}$ at Earth, S_{slab} is the fraction of slab turbulence, $C_s = 0.06(\delta B^2/B_0^2)\mathrm{nT}^2$ is the level of turbulence and δB^2 is the variance of the magnetic field. Here $\xi = 10.0P$ in units of GV and the range 0.2 GV $\leq \xi \leq$ 100.0 GV, is applicable for both polarity cycles, with $\xi_0 = 1$ GV. This quantity determines the transition from $\lambda_{\parallel} \propto P$ to $\lambda_{\parallel} \propto P^2$.

To construct a diffusion tensor applicable to the whole heliosphere, Burger et al. (2000) used the spatial variations of $\delta B^2/B_0^2$ and l/l_e. This was done by dividing the heliosphere in three distinct regions with different turbulence mechanisms dominating in each region. An ionization cavity is defined with radius r = 10 AU, inside the ionization cavity a so-called 'stream-interaction' approach dominates in the slow solar wind region centered on the equatorial plane. A different approach, namely the 'undriven' approach, dominates in the high speed high latitude region (Hattingh, 1998). Outside the ionization cavity the 'pickup ions' approach dominates. For the first two regions, expressions for $\delta B^2/B_0^2$ and l/l_e by Zank et al. (1996) were used, while for the third region Hattingh (1998) and Burger and Hattingh (1998) derived an analytical expression based on the results of Zank et al. (1996).

For both polarity cycles, tilt angles and all species an additional adjustment had to be made to the radial dependence of $K_{\parallel}$:

$$K_{\parallel}^{*} = K_{\parallel}\left(45.0 - \frac{r}{r_e}\right)^{-0.218\alpha+0.289} \tag{3.19}$$

if 0.1 AU < r < 45.0 AU, in order to fit the measured proton radial intensities in the inner heliosphere and at Earth.

Assuming these expressions for the different turbulence models dominating in different parts in the heliosphere results in a $\lambda_{\parallel}$ with different spatial dependences. Figure 3.4 shows the radial dependence of $\lambda_{\parallel}$ at a rigidity of 1.05 GV in the equatorial plane and polar region as well as the rigidity dependence in the equatorial plane at radial distances of 1, 50 and 91

AU. Evident is the different spatial dependences in different parts of the heliosphere. Note the break in the radial dependence for the ionization cavity. The parallel mean free path decreases by the same magnitude for both equatorial plane and polar regions beyond the TS since it is related to the assumed constant compression ratio; the latitude dependence of this parameter is investigated in later chapters. The parallel mean free path for protons as a function of rigidity has typical values between 0.07 AU – 1.5 AU at Earth in the equatorial plane which is in good agreement with the values given by Burger et al. (2000).

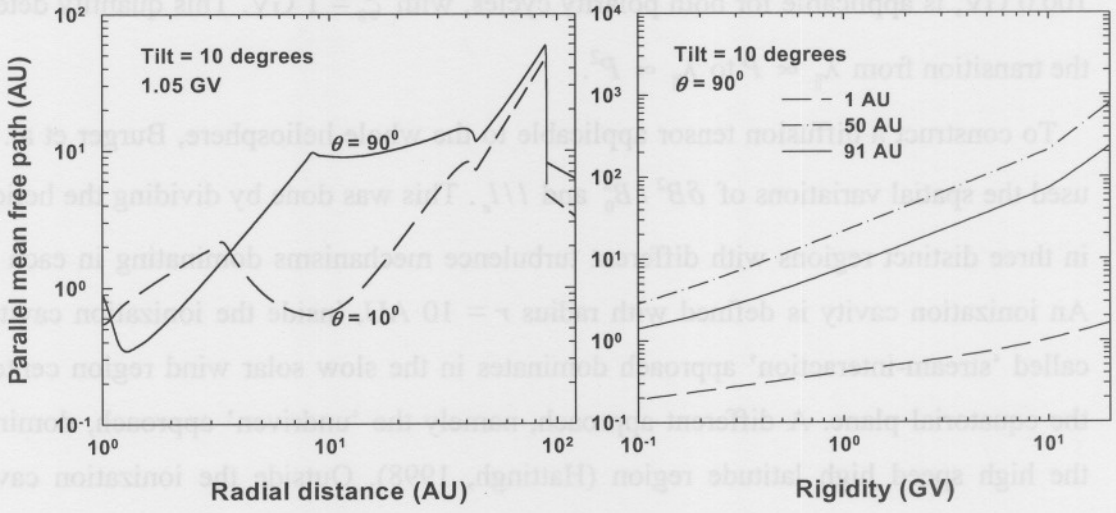

Figure 3.4. Left panel: The parallel mean free path for 1.05 GV protons as a function of radial distance near the heliospheric poles with $\theta = 10°$ (dashed line) and in the equatorial plane with $\theta = 90°$ (solid line) for solar minimum ($\alpha = 10°$) conditions. The TS is set at 90 AU. Right panel: The parallel mean free path as a function of rigidity for solar minimum conditions at radial distances of 1, 50 and 91 AU.

3.4.2.2 The perpendicular diffusion coefficient

The transport of the charged particles perpendicular to the HMF is described by the perpendicular diffusion coefficient $K_{\perp}$, which can be subdivided into two possibly independent coefficients, namely $K_{\perp r}$ and $K_{\perp \theta}$, which are the perpendicular diffusion in radial and polar direction, respectively. In this work following Langner (2004), $K_{\perp}$ is similar to that given in Burger et al. (2000) except for minor changes introduced by the TS and it is assumed anisotropic, given by the two perpendicular diffusion coefficients:

$$K_{\perp r} = K_e^0 \frac{\delta B^2}{B_0^2} K_{\parallel} \left(\frac{P}{P_0} \right)^{\gamma}, \tag{3.20}$$

and $$K_{\perp \theta} = g(\theta) \frac{\delta B^2}{B_0^2} K_{\parallel} \left(\frac{P}{P_0} \right)^{\eta}, \tag{3.21}$$

with $$g(\theta) = \frac{K_p^0 + K_e^0}{2} \mp \left(\frac{K_p^0 - K_e^0}{2} \right) \tanh \left[8 \left(\theta - \frac{\pi}{2} \pm \frac{25\pi}{180} \right) \right], \tag{3.22}$$

where θ is the polar angle in radians and the upper sign in $g(\theta)$ is valid for $\theta \leq 90°$ and lower signs for $\theta > 90°$ with $P_0 = 1$ GV. The quantities $\eta = \gamma = -0.4$ change the rigidity dependence of the perpendicular diffusion coefficients compared to that of the parallel diffusion. The quantities K_p^0 and K_e^0 are dimensionless. Diffusion perpendicular to the HMF is thus enhanced in the polar direction by assuming $K_p^0 > K_e^0$ according to Equation (3.22) (Kóta and Jokipii, 1995; Potgieter, 1996, 2000; Burger et al., 2000; Ferreira et al., 2000; Fichtner et al., 2000; Langner, 2004). The quantities are $K_p^0 = 0.185$ and $K_e^0 = 0.026$ when $\alpha = 10°$. A physical justification of this increase in $K_{\perp \theta}$ toward the polar regions is given by Burger et al. (2000), basing their arguments on Ulysses measurements which have shown an increase in the variance of the components of the HMF, δB^2 in Equation (3.16) to (3.18), as it moved away from the equatorial plane to smaller polar angles. Figure 3.5 shows the radial dependence of $\lambda_{\perp r}$ and $\lambda_{\perp \theta}$ at a rigidity of 1.05 GV in the equatorial plane and over the polar region for $\alpha = 10°$. Also shown in the figure is the rigidity dependence of $\lambda_{\perp r}$ and $\lambda_{\perp \theta}$ at radial distances of 1, 50 and 91 AU in the equatorial plane for $\alpha = 10°$. Typical values as a function of rigidity for $\lambda_{\perp r} / \lambda_{\parallel}$ at Earth for protons in this model are between 0.003 and 0.2 for 0.5 MV to 5.0 GV, respectively, which are in good agreement with the values given by Burger et al. (2000).

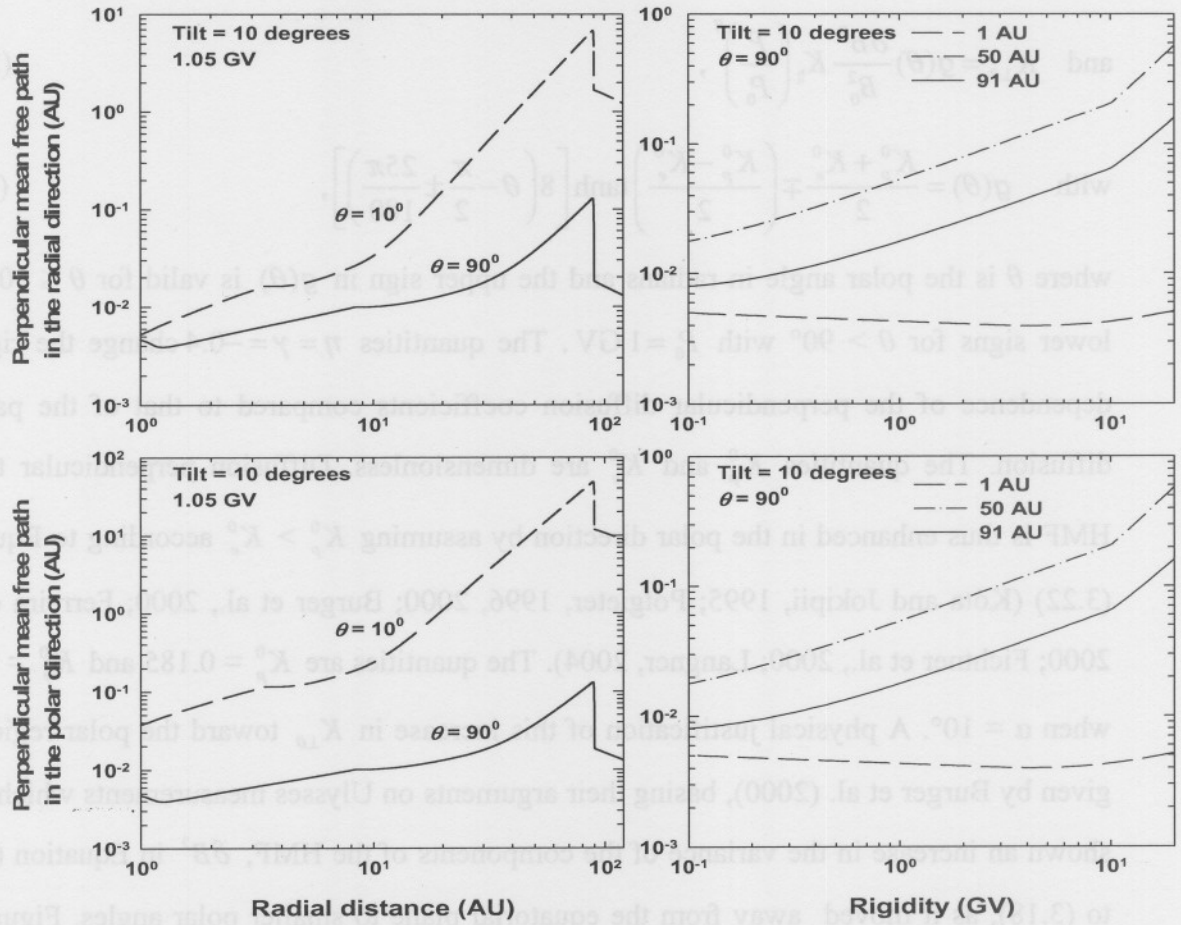

Figure 3.5. Top row: The perpendicular mean free path in the radial direction ($\lambda_{\perp r}$) for 1.05 GV protons as a function of radial distance (left panel) at the pole (dashed line) and in the equatorial plane (solid line) for solar minimum conditions ($\alpha = 10°$) and as a function of rigidity (right panel) at radial distances 1, 50 and 91 AU. The TS is set at 90 AU. Bottom row: The same as the top row but for the perpendicular mean free path in the polar direction ($\lambda_{\perp\theta}$).

3.4.2.3 The drift term

Under the assumption of weak scattering the drift coefficient, K_A, in Equation (3.5) is given by:

$$(K_A)_{traditional} = K_A^0 \frac{vP}{3cB} \tag{3.23}$$

with a dimensionless constant K_A^0. This equation describes what Potgieter et al. (1989) have called 100% (full drifts $K_A^0 = 1.0$), 50% (half drifts $K_A^0 = 0.5$) and no-drifts ($K_A^0 = 0$). This

traditional drift term K_A^0 has been used previously by many authors e.g., Haasbroek (1997), Ferreira et al. (2000), Potgieter (1996, 2000) and Ferreira and Potgieter (2004). The drift coefficient used by Burger et al. (2000) and Langner (2004) differs slightly from the traditional form and is given by

$$K_A = K_A^0 \frac{vP}{3cB}\left(\frac{10P^2}{1+10P^2}\right). \tag{3.24}$$

Below ~ 1.0 GV, drifts are thus slightly reduced with respect to weak scattering case for which $K_A \propto P$. This choice for the drift coefficient is consistent with the numerical simulations of Giacalone et al. (1999), which shows that in the case of weak scattering the 'standard' result as given by Equation (3.23) is in fact appropriate. In this work $K_A^0 = 0.5$ for all tilt angles and both polarity cycles corresponding to 50% drifts. Figure 3.6 shows the radial dependence of the diffusion coefficient due to drifts, as described in Equation (3.15), at a rigidity of 1.05 GV in the equatorial plane and over the polar region for α = 10°. Also shown in the figure is the rigidity dependence of this diffusion coefficient at radial distances of 1, 50 and 91 AU in the equatorial plane for α = 10°. It is evident that $K_{\theta r}$ decreases as a function of decreasing rigidity.

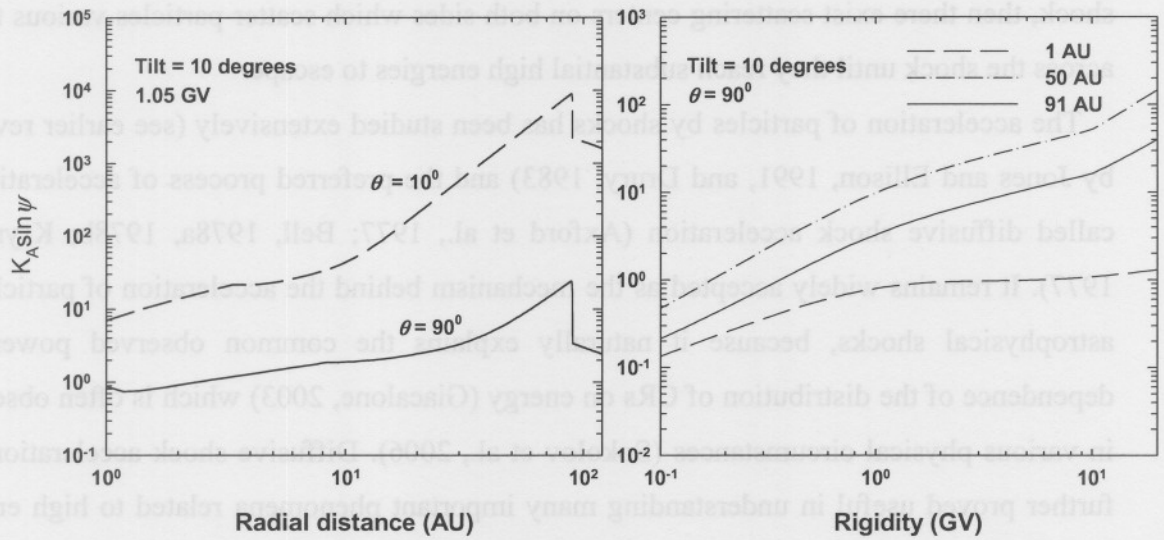

Figure 3.6. Left panel: The diffusion coefficient due to drifts ($K_{\theta r}$) in the θr direction for 1.05 GV protons as a function of radial distance at the poles with $\theta = 10°$ (dashed line) and equatorial plane with $\theta = 90°$ (solid line) for solar minimum (α = 10°) conditions. The TS is set at 90 AU. Right panel: The drift term as a function of rigidity for solar minimum conditions at radial distances 1, 50 and 91 AU.

3.5 Shock acceleration

In the above sections the diffusion and drift processes of CR particles in the heliosphere as they occur in the TPE have been discussed. This section briefly discusses the acceleration processes of charged particles by magnetohydrodynamic shocks.

Magnetohydrodynamic (MHD) shocks are defined as shocks in media that contain magnetic fields. Since an ionized gas or plasma has a high conductivity any magnetic field will be tied to the plasma (i.e., "frozen in") and will, in general, contribute to the dynamics of the shock. When the magnetic field is parallel to the normal on the shock front and therefore in the same direction as the plasma flow, the MHD shock is called parallel. In this case the field is continuous across the shock and it has no effect on the shock structure. In oblique shocks (shocks with an angle between the upstream magnetic field and the shock normal greater than 0°), the magnetic field takes a more active role and influences both the shock jump conditions and particle acceleration (for details see Giacalone, 2005; Giacalone and Jokipii, 2005). Jokipii (1982, 1987) explicitly discussed the role of the angle between the shock normal and the magnetic field in shock acceleration. He found that the acceleration rate, and the maximum energy attainable over a given time interval, is highest for a perpendicular shock. The magnetic field is not smooth but turbulent on both side of the shock, then there exist scattering centers on both sides which scatter particles various times across the shock until they reach substantial high energies to escape.

The acceleration of particles by shocks has been studied extensively (see earlier reviews by Jones and Ellison, 1991, and Drury, 1983) and the preferred process of acceleration is called diffusive shock acceleration (Axford et al., 1977; Bell, 1978a, 1978b; Krymski, 1977). It remains widely accepted as the mechanism behind the acceleration of particles at astrophysical shocks, because it naturally explains the common observed power-law dependence of the distribution of CRs on energy (Giacalone, 2003) which is often observed in various physical circumstances (Sokolov et al., 2006). Diffusive shock acceleration has further proved useful in understanding many important phenomena related to high energy particles in astrophysical plasmas. In this work, it will be applied to the solar wind termination shock. For overviews of these aspects related to the heliosphere, see Zank (1999) and Fichtner (2001).

3.5.1 First-order Fermi acceleration

In the presence of any jump in plasma bulk velocity, first-order Fermi acceleration is an unavoidable consequence if particles cross such a jump multiple times. The basic idea is that since the downward plasma is faster than the plasma upstream of the shock, energetic particles are, in effect, bouncing between two converging "walls", thus continuously gaining energy (Giacalone, 2003, 2005). Such shocks exist in a wide variety of astrophysical plasmas including those associated with supernovae blast waves, coronal mass ejection, and the termination shock of the solar wind.

3.5.2 Second-order Fermi acceleration

In the presence of magnetic-field fluctuations, which provide the means of cross shock transport, ions are also scattered back and forth between plasma waves with different velocities in the plasma frame. This leads to a second-order Fermi acceleration, which is also a natural consequence of particle transport. Comparing with first-order Fermi acceleration, whose strength derives from the change in the bulk velocity at a discontinuity, second-order Fermi acceleration depends on the random speed scattering centers in the plasma and hence it is a stochastic process. First-order Fermi acceleration is usually stronger than second-order Fermi acceleration in supersonic flows with discontinuities. However, in the absence of discontinuities second-order Fermi acceleration may become the dominant process.

3.6 Numerical modulation models

The first numerical model of the TPE was developed by Fisk (1971), who solved the TPE numerically by assuming a steady–state and spherical symmetry, i.e. a one dimensional (1D) model with the radial distance as the only spatial variable. Later the polar angle was included to form a two dimensional (2D) model without drifts (Fisk, 1976).

After this, various authors contributed to the development of increasingly sophisticated numerical models, see e.g., Potgieter (1984), Burger (1987), le Roux (1990), Steenkamp (1995), Haasbroek (1997), Hattingh (1998), Ferreira (2002) and Langner (2004). The first 2D models where the wavy HCS was emulated were developed by Potgieter (1984) and Burger (1987) (see also Potgieter and Moraal, 1985; Burger and Potgieter, 1989). This

simulation has been improved by Hattingh (1993) and is referred to as the WCS-model (see also Hattingh and Burger, 1995).

The first three-dimensional (3D) steady-state model including drifts and full wavy HCS was developed by Kóta and Jokipii (1983) and later by Hattingh (1998) and more recently by Gil and Alania (2001). A comparison of the 2D and 3D steady-state models were done by Hattingh (1998) and Ferreira (1998) to show to what extent they agree. They found that the agreement was excellent and therefore the 2D models, which use less computer time and memory, can be used with great confidence. By including drifts in modulation models the 22-year record of the long-term variation of CR flux observed by neutron monitors could be explained (see also Potgieter and Moraal, 1985, and Ferreira and Potgieter, 2004).

The 2D time-dependent shock acceleration model with continuous and discontinuous transitions of the solar wind as developed by Steenkamp (1995), le Roux et al. (1996), Haasbroek (1997), Steenberg (1998), Ferreira (2002) and Langner (2004) is used in this study except for changes in certain parameters which will be explained in detail in later chapters. For this model Equation (3.3) is solved with $\frac{\partial f}{\partial \phi} = 0$.

3.6.1 Boundary conditions

Equation (3.3), without azimuthal dependence, is solved numerically using the following boundary conditions:

(1) The heliosphere is taken to be spherical with an outer boundary (HP) at r_b = 120 AU where relevant local interstellar spectra (LIS) is specified as input spectra for GCRs.

(2) The boundary condition at the inner boundary, r_1, is assumed to be an absorbing boundary

$$\left.\frac{\partial f}{\partial r}\right|_{\lim r \to r_1^+} = \left.\frac{\partial f}{\partial r}\right|_{\lim r \to r_1^-} . \tag{3.25}$$

This implies that particles can enter (or leave) this boundary.

A reflecting boundary, implying that no particles can enter or leave this boundary, can also be used where

$$\left.\frac{\partial f}{\partial r}\right|_{r=r_1} = 0 . \tag{3.26}$$

Siluszyk and Alania (2001) showed that Equation (3.25) for an absorbing boundary could be a more appropriate boundary condition than Equation (3.26) for a reflecting boundary. However, comparisons between model calculations for these two different boundary conditions showed that this model was surprisingly insensitive to this feature and no effect was present in a distance larger than 0.15 AU from r_1.

(3) At the TS the distribution function and the radial streaming are assumed to be related by $f^- = f^+$ and $S_r^+ - S_r^- = Q_*$ respectively. Where '–' represents the upstream region and '+' the downstream region.

(4) The heliosphere is assumed to be symmetrical about the poles and equatorial plane, which implies that

$$\left.\frac{\partial f}{\partial \theta}\right|_{\theta=0,\pi/2,\pi} = 0 \qquad (3.27)$$

at these positions in the heliosphere. See also Steenkamp (1995).

3.6.2 Termination shock models

The phenomenon of shock acceleration at the TS as a source of the anomalous component of CRs in the heliosphere led to the development of the first 2D drift modulation model that included shock acceleration (Jokipii, 1986). From this work it was found that the principles of diffusive shock acceleration gave a natural explanation to several observed features of the anomalous component, e.g. the unexpected enhancements observed in the intensity of singly ionized helium, nitrogen, oxygen and other heavier elements at low energies. Although Jokipii (1986) had to use a time-dependent numerical scheme to handle energy changes, Potgieter and Moraal (1988) demonstrated that it was possible to include shock acceleration in a 1D steady-state model by specifying the appropriate boundary conditions with regard to CR streaming and spectra at the TS. This later model was expanded to 2D by Potgieter (1989) who used it to obtain reasonable fits to observed anomalous oxygen spectra. Kóta and Jokipii (1991) reported on their 3D shock acceleration model that could be applied to study particle acceleration at CIRs. Steenkamp (1995) developed an independent 2D shock acceleration model that was used to study the anomalous component. le Roux et al. (1996) also developed an independent 2D drift and acceleration model. Although this model was originally developed in 2D, it was only applied in 1D. This model was expanded by Haasbroek (1997) and Ferreira (2002), who applied it mainly to the shock

acceleration of electrons. In this study the 2D shock acceleration model developed by Langner (2004) is used. This model includes particle drifts and a new, more fundamental, approach to heliospheric diffusion coefficients as described above.

3.6.3 The numerical solution of the TPE

Equation (3.2) is a partial differential equation (PDE) and is a linear second-order parabolic PDE in four variables (two spatial variables r and θ, rigidity P, and time t). The TPE is solved by applying the Alternating Direct Implicit (ADI) method, which is a modification of the Crank-Nicholson finite difference method, or by using the fractional splitting method called the locally one-dimensional (LOD) method. Both these method were tested against each other and it was found that they gave solutions that were qualitatively the same so that from a physics point of view they would therefore be considered equally good (see e.g., Lapidus and Pinder, 1982 for a comparison of the LOD and Peace-Rachford ADI algorithm; Steenkamp, 1995). However, the LOD method is used for the TS model which has been developed by Langner (2004), and it is also used in this work, because the usage of computer memory and time is optimized, which is still a major consideration.

The technical details of the numerical model used in this study is based on the work of Langner (2004), for a detail discussion on the numerical scheme the reader is referred to Chapter 3 of Langner (2004).

3.7 Summary

The distribution of cosmic rays inside the heliosphere is a result of four modulation processes namely diffusion, convection, drift and adiabatic energy changes which can be combined into a transport equation (Parker, 1965). This equation can be solved numerically in various dimensions to study cosmic ray transport and shock acceleration. It has been shown that in 2D modulation models four different diffusion coefficients are of particular interest, namely $K_{\parallel}$, $K_{\perp r}$, $K_{\perp\theta}$ and K_{A}. The first coefficient $K_{\parallel}$ was constructed based on theoretical calculations without a dissipation range but with slab/2D turbulence according to the work of Burger et al. (2000). Because of the complexity, $K_{\perp}$ is scaled as $K_{\parallel}$. Furthermore, it was illustrated by Potgieter et al. (1997), Burger et al. (2000) and Ferreira (2002) that to produce the correct CR latitude dependence, $K_{\perp\theta}$ needs to enhance toward

the poles. The drift coefficient describes gradient and curvature of the field, and any abrupt change in the field direction such as HCS. The drift directions depend on the HMF polarity sign and influence cosmic ray transport resulting in a 22-year and charge-sign dependent modulation (Potgieter and Moraal, 1985).

At the TS low energy particles are accelerated to higher energies by a process called diffusive shock acceleration. This process remains widely accepted because it naturally explains the common observed power-law dependence of the distribution of CRs on energy.

In the following chapters the TS model of Langner (2004) will be applied to the study of modulation of galactic and anomalous protons in the heliosphere.

Chapter 4

Effects of the latitude dependence of the shock's compression ratio and the injection efficiency on cosmic ray spectra in the heliosphere

4.1 Introduction

On 16 December 2004, the spacecraft Voyager 1 (V1) crossed the TS of the solar wind (Stone et al., 2005; Decker et al., 2005). This observation confirms that the HMF increases across the TS by a ratio proportional to the compression ratio of the TS (Burlaga et al., 2005). It was expected that the intensity of the ACRs would peak at the TS. However, at the location of the TS encountered by V1, no direct evidence was found of the source of the ACRs. Langner et al. (2006b) showed that the ACR intensity does not necessarily reach a maximum at the TS but because of adiabatic heating in the nose direction of the heliosphere it could increase with increasing distance beyond the TS.

Stone et al. (2005) reported that the spectra measured by V1 at ~ 94 AU appear to consist of three different populations of particles and that the compression ratio of the TS was ~ 2.5, calculated from the spectral index of the power law type intensity profiles, but it could be as low as 2. This observation confirms that the TS is not a strong shock, at least not where V1 crossed into the heliosheath.

Scherer et al. (2006) studied the latitudinal dependence of the compression ratio of the TS and the injection efficiency of pick-up ions as source of the ACRs using a hydrodynamic (HD) model (Scherer and Ferreira, 2005). They found that during solar minimum conditions a significant decrease of both parameters towards the heliospheric poles is possible.

In this chapter, the effects of changing the essential modeling parameters are investigated, in particular the latitude dependence of the shock's compression ratio s and the injection efficiency, and the subsequent effects on the modulation of ACRs and GCRs in the heliosphere. This is followed by investigating the effects of the negative divergence of the solar wind velocity in the heliosheath.

4.2 Cosmic ray intensities at the TS as measured by V1

The TS was believed to be the source of ACRs and little modulation of the source spectra was expected in the heliosheath. Stone et al. (2005) fitted their model against V1 data in the heliosheath and found that the shock acceleration model was unable to reproduce the intensities of the CRs as measured by V1. These authors interpreted their result as an indication that the TS may not be the source of the ACRs.

The spectra between 1 and 500 MeV/nuc observed by V1 in the heliosheath are shown in Figure 4.1. The spectra (up to 10-20 MeV for protons and up to ~ 10 MeV/nuc for He) are broken power laws with a break energy of ~ 3.5 MeV for protons. ACR protons were not clearly observable during this period after the TS crossing in December 2004 as the large error bars indicate. The GCR protons are in contrast clearly recognizable at energies above

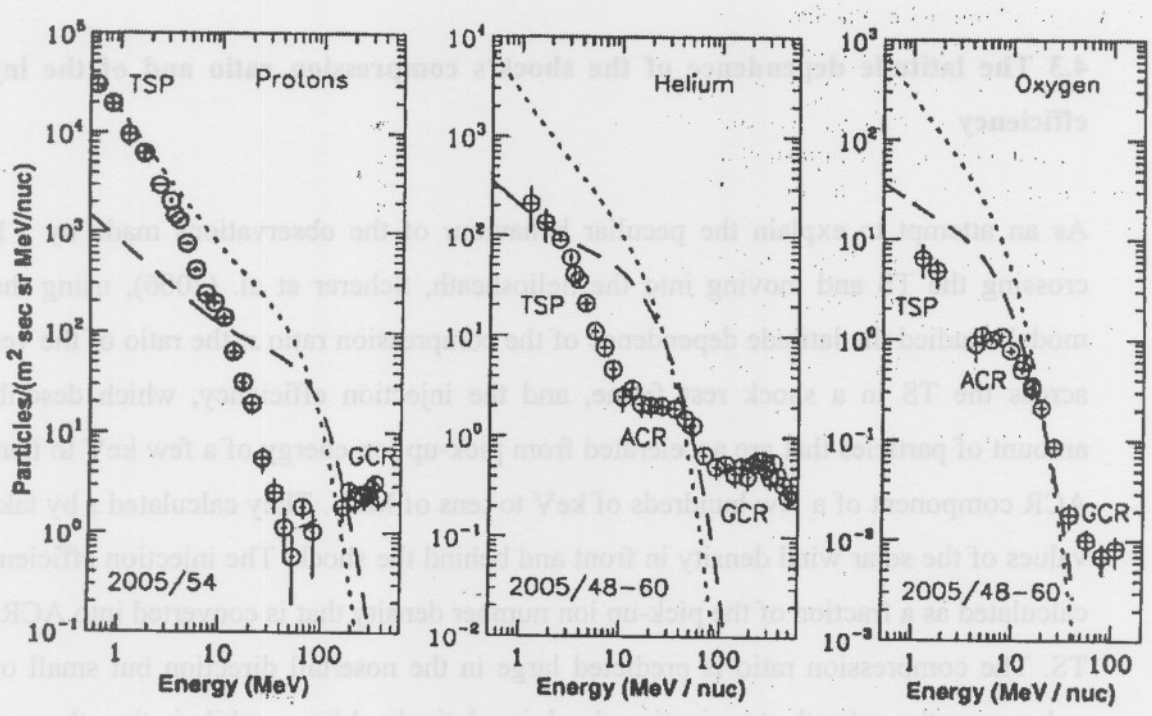

Figure 4.1. Spectra observed by V1 in the heliosheath, about two months after the TS crossing in December 2004. The spectra are broken power laws, e.g., with a break energy of ~3.5 MeV for protons. The He and O spectra are dominated by ACRs at mid-energies and by GCRs at higher energies. The predicted ACR spectra at the shock are shown for a strong (s = 4.0, dashed line) and a weak (s = 2.4, dotted line) shock (from Stone et al., 2005).

~ 200 MeV. The He and O spectra, on the other hand, are dominated by ACRs at mid-energies and by GCRs at higher energies. The predicted ACR spectra at the shock are shown for a strong (s = 4.0, dashed line) and a weak (s = 2.4, dotted line) shock (Stone et al., 2005). Evident from Figure 4.1 is that their model cannot reproduce the intensities as measured by V1, e.g. at ~ 80 MeV the observed ACR protons intensity is a factor of about 20 less than the model predicts. Furthermore, for the strong shock, the model fails to reproduce the proton observations, while for the weak shock the model fails to fit the Helium spectra, while both approaches seem to fit the Oxygen observations above ~10 MeV/nuc. These and other factors led Stone et al. (2005) to the conclusion that it is also possible that a more fundamental change in the standard modeling approach of ACR acceleration is required. However, it is also possible that other features of the TS such as the latitude dependence of s, neglected in their model, could improve the situation. Some of these aspects will be discussed in what follows.

4.3 The latitude dependence of the shock's compression ratio and of the injection efficiency

As an attempt to explain the peculiar behaviour of the observations made by V1 when crossing the TS and moving into the heliosheath, Scherer et al. (2006), using their HD model, studied the latitude dependence of the compression ratio s, the ratio of the velocities across the TS in a shock rest frame, and the injection efficiency, which describes the amount of particles that are accelerated from pick-up ion energy of a few keV to that of the ACR component of a few hundreds of keV to tens of MeV. They calculated s by taking the values of the solar wind density in front and behind the shock. The injection efficiency was calculated as a fraction of the pick-up ion number density that is converted into ACRs at the TS. The compression ratio is predicted large in the nose/tail direction but small over the poles; over the poles the termination shock is relatively oblique, while in the other regions it becomes increasingly perpendicular. Furthermore, during solar minimum conditions the increasing solar wind speed and simultaneously decreasing proton number density causes small values of s and the injection efficiency over the poles. This is shown in Figure 4.2, taken from Scherer et al. (2006). Evident from Figure 4.2 is that both the compression ratio and the injection efficiency have a clear latitude dependence that is strong at the equatorial plane (0° in their computations; in this work with the polar angle $\theta = 90°$) and weak at the

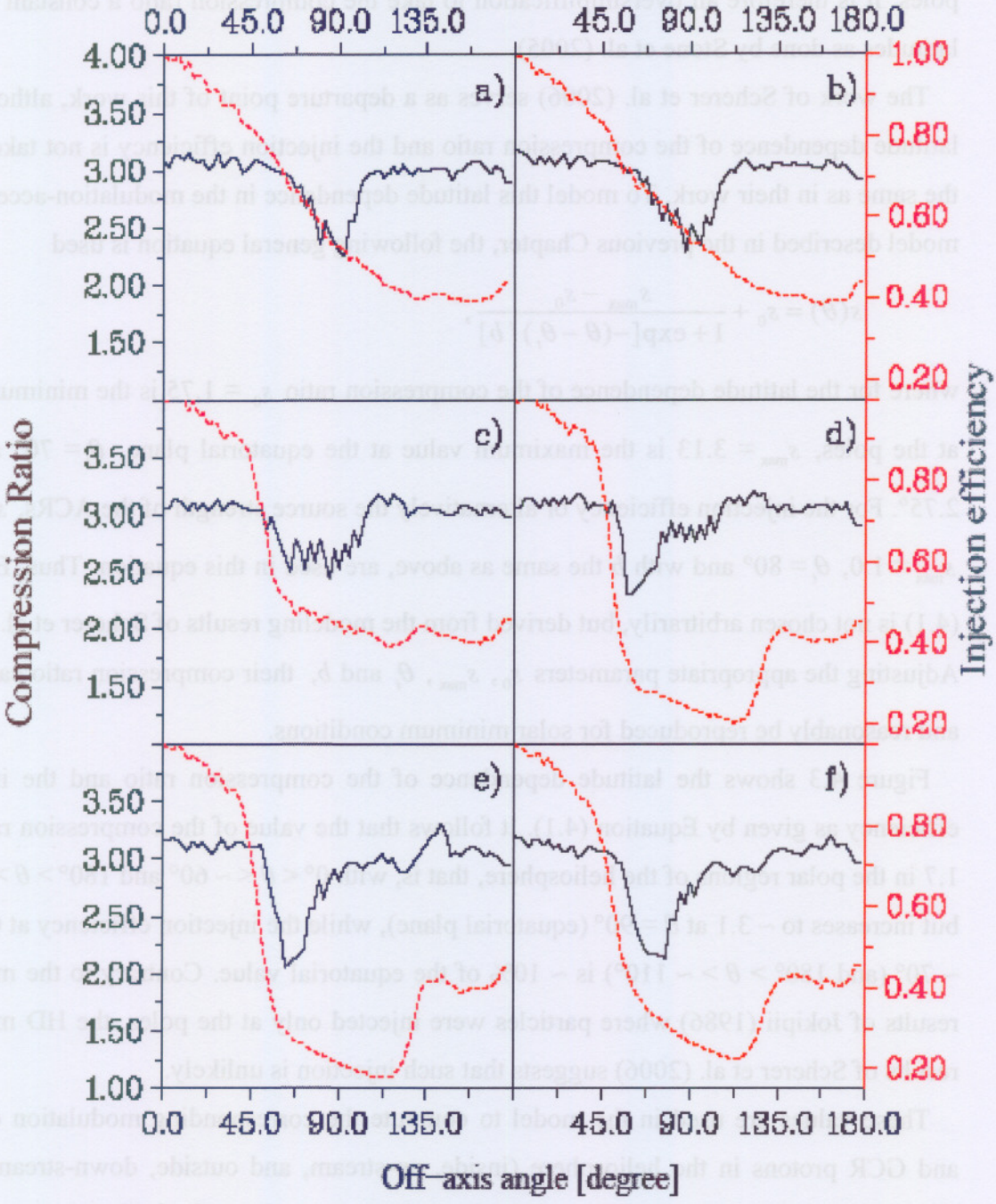

Figure 4.2. The compression ratio *s* (solid line) and the injection efficiency (dashed line) as a function of the off-axis angle (0° upwind – heliospheric nose, 90° poleward, 180° downwind- heliospheric tail). The scales on the left side correspond to the compression ratio; those on the right side to the injection efficiency, normalized to its value in the nose direction. The time in panel (a) is for a simulated solar maximum activity epoch, which then changes in one year steps to (d) with solar minimum conditions and back to the inclining solar activity shown in panel (f). From Scherer et al. (2006).

poles. It is therefore an oversimplification to take the compression ratio a constant over all latitudes as done by Stone et al. (2005).

The work of Scherer et al. (2006) serves as a departure point of this work, although the latitude dependence of the compression ratio and the injection efficiency is not taken to be the same as in their work. To model this latitude dependence in the modulation-acceleration model described in the previous Chapter, the following general equation is used

$$s(\theta) = s_0 + \frac{s_{\max} - s_0}{1 + \exp[-(\theta - \theta_t)/b]}, \tag{4.1}$$

where for the latitude dependence of the compression ratio $s_0 = 1.75$ is the minimum value at the poles, $s_{\max} = 3.13$ is the maximum value at the equatorial plane, $\theta_t = 70°$ and $b = 2.75°$. For the injection efficiency or alternatively the source strength of the ACRs, $s_0 = 0.1$, $s_{\max} = 1.0$, $\theta_t = 80°$ and with b the same as above, are used in this equation. Thus, Equation (4.1) is not chosen arbitrarily, but derived from the modeling results of Scherer et al. (2006). Adjusting the appropriate parameters s_0, $s_{\max}$, θ_t and b, their compression ratio can easily and reasonably be reproduced for solar minimum conditions.

Figure 4.3 shows the latitude dependence of the compression ratio and the injection efficiency as given by Equation (4.1). It follows that the value of the compression ratio is ~ 1.7 in the polar regions of the heliosphere, that is, with $0° < \theta < \sim 60°$ and $180° > \theta > \sim 120°$ but increases to ~ 3.1 at $\theta = 90°$ (equatorial plane), while the injection efficiency at $0° < \theta < \sim 70°$ (and $180° > \theta > \sim 110°$) is ~ 10% of the equatorial value. Contrary to the modeling results of Jokipii (1986) where particles were injected only at the poles, the HD modeling results of Scherer et al. (2006) suggests that such injection is unlikely.

These values are used in the model to compute the corresponding modulation of ACR and GCR protons in the heliosphere (inside, up-stream, and outside, down-stream of the TS), comparing them to the values without a latitude dependence for both these parameters. The value of s when no latitude dependence is assumed is 3.2 over all latitudes. In what follows, it is assumed that $\nabla.\mathbf{V} = 0$ in the heliosheath, which means that no adiabatic acceleration of particles occur beyond the TS in the heliosheath, unless specified otherwise.

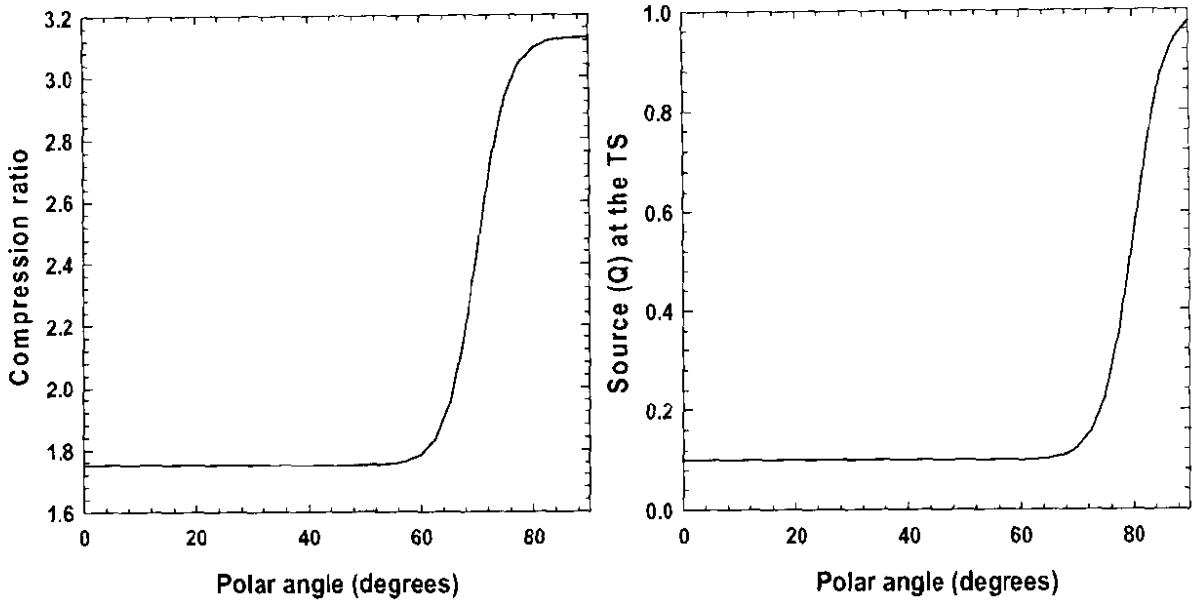

Figure 4.3. The compression ratio (left panel) and injection efficiency (or alternatively, the ACR source strength - right panel) as a function of polar angle; the equatorial plane is at 90°.

4.4 The effects of the latitude dependent compression ratio on GCR proton spectra

The LIS for GCR protons below a few GeV cannot be measured directly inside the heliosphere because of modulation, especially at low energies where large adiabatic energy losses these particles experience during their inward propagation. Many proposed LIS for the different GCR species exist, using various different techniques to calculate them (see e.g., Langner, 2000). For this work the proton LIS of Moskalenko et al. (2002) is used, based on their state-of-the-art galactic propagation models. They showed that the LIS for protons gives most reasonable heliospheric modulation results – see also Langner et al. (2003, 2004).

The LIS for GCR protons is specified at the heliospheric boundary (r_b = HP) as an initial condition for the numerical model. The proton LIS of Moskalenko et al. (2002) is given by

$$j_{LIS} = \begin{cases} \exp\left(4.64 - 0.08(\ln E)^2 - 2.91\sqrt{E}\right) & \text{if } E < 1.0\,\text{GeV} \\ \exp\left(3.22 - 2.86(\ln E) - \dfrac{1.50}{E}\right) & \text{if } E \geq 1.0\,\text{GeV}, \end{cases} \tag{4.2}$$

with E the kinetic energy in GeV, $j_{LIS} = P^2 f$ the differential intensity in particles MeV^{-1}. $m^{-2}.s^{-1}.sr^{-1}$ and $P = pc/q$ the rigidity in GV, and where p is the particle momentum, c the speed of light in space, q the particle charge and f the GCR distribution function.

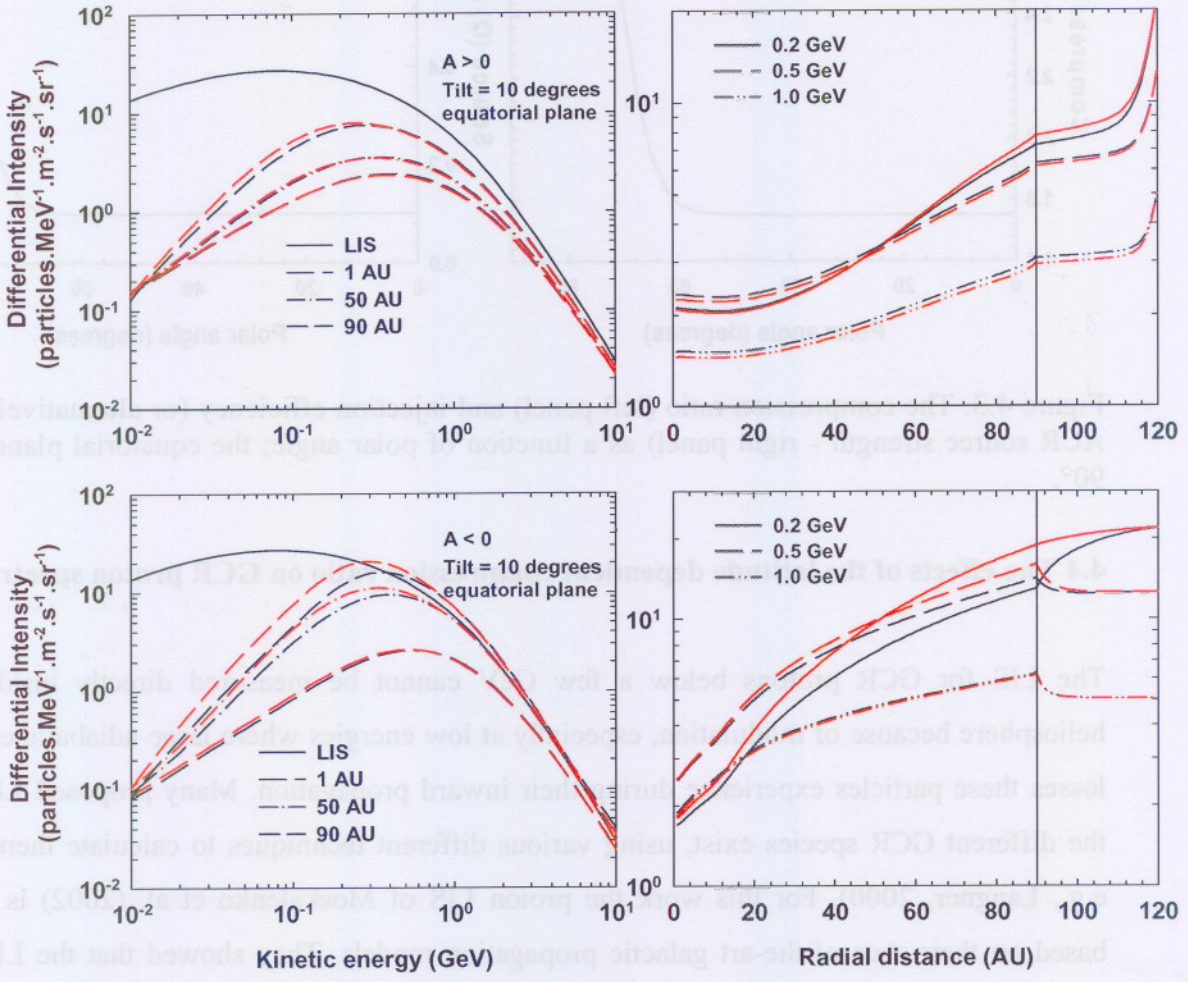

Figure 4.4. Left panels: Computed differential intensities for GCR protons as a function of kinetic energy for both polarity cycles and solar minimum (α = 10°) condition at radial distances of 1 (Earth), 50, and 90 AU in the equatorial plane. Right panels: Corresponding differential intensities as a function of radial distance for 0.2, 0.5 and 1.0 GeV, respectively. Two sets of solutions are shown, first without a latitude dependence (black lines) and second with a latitude dependence of the compression ratio (red lines). The TS is at 90 AU and the HP, where the LIS is specified, is at 120 AU.

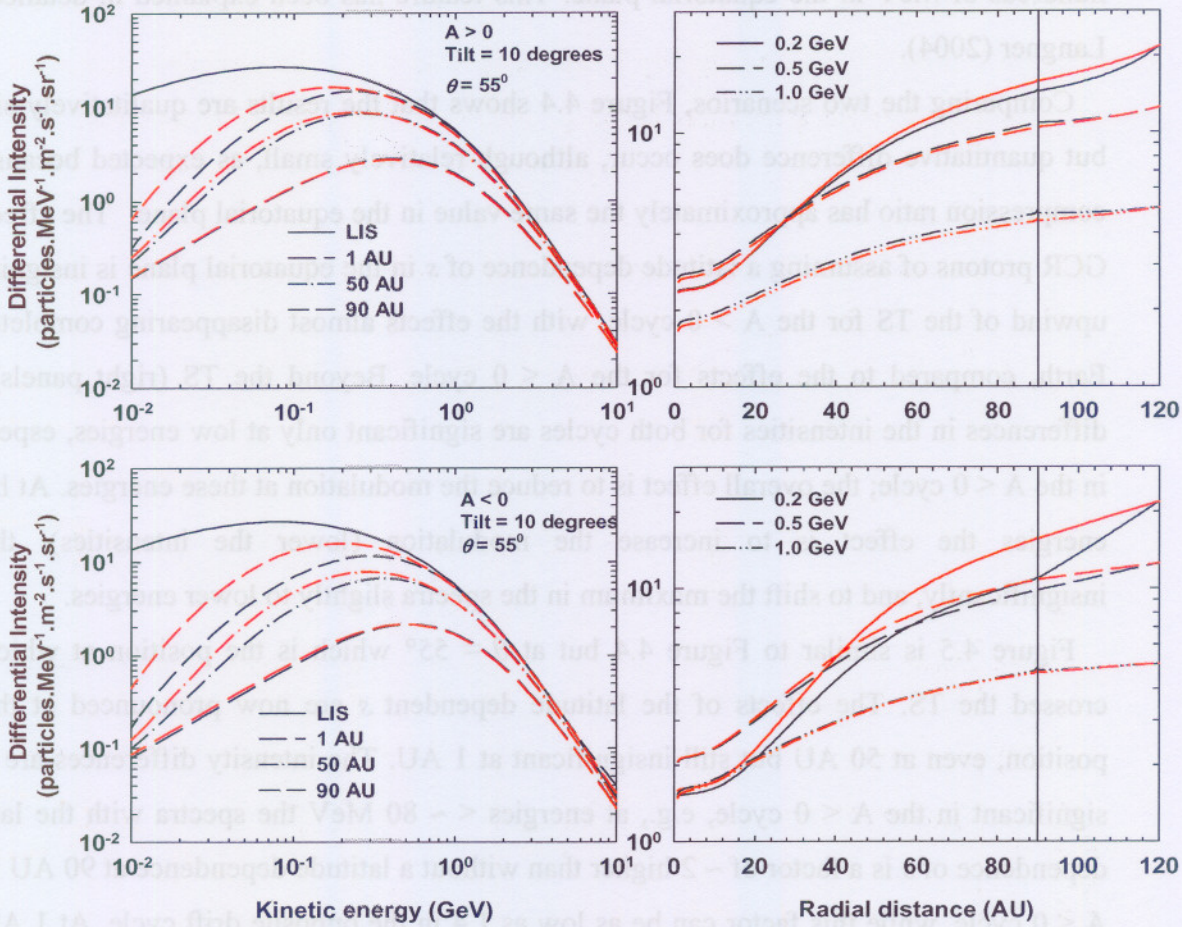

Figure 4.5. Similar to Figure 4.4 but for $\theta = 55°$.

Figure 4.4 shows the computed differential intensities for GCR protons as a function of kinetic energy for both polarity cycles in the equatorial plane and for solar minimum conditions, with the HCS tilt angle $\alpha = 10°$. The energy spectra are shown at radial distances of 1, 50 and 90 AU with respect to the LIS for comparison and the differential intensities as a function of radial distance at energies of 0.2, 0.5 and 1.0 GeV, respectively. Two sets of spectra are shown, first without a latitude dependence (black lines) and then with a latitude dependence (red lines) of the compression ratio. The TS is at 90 AU and the HP, where the LIS is specified, is at 120 AU. The effects of the TS with no latitude dependence of s on GCRs proton spectra have been studied intensively (e.g., Steenkamp, 1995; Steenberg, 1998; Ferreira, 2002; Langner, 2004), but the modulation effects of the latitude dependent TS have not been shown before. However, qualitative similarities are explored, e.g., the TS effect in both scenarios is most pronounced for the $A < 0$ polarity cycle in the sense that the modulated spectra exceed the LIS value at energies above several

hundreds of MeV in the equatorial plane. This feature has been explained in detailed, see Langner (2004).

Comparing the two scenarios, Figure 4.4 shows that the results are qualitatively similar but quantitative difference does occur, although relatively small, as expected because the compression ratio has approximately the same value in the equatorial plane. The effects on GCR protons of assuming a latitude dependence of s in the equatorial plane is insignificant upwind of the TS for the A > 0 cycle, with the effects almost disappearing completely at Earth, compared to the effects for the A < 0 cycle. Beyond the TS (right panels), the differences in the intensities for both cycles are significant only at low energies, especially in the A < 0 cycle; the overall effect is to reduce the modulation at these energies. At higher energies the effect is to increase the modulation (lower the intensities), though insignificantly, and to shift the maximum in the spectra slightly to lower energies.

Figure 4.5 is similar to Figure 4.4 but at θ = 55° which is the position at which V1 crossed the TS. The effects of the latitude dependent s are now pronounced at the TS position, even at 50 AU but still insignificant at 1 AU. The intensity differences are more significant in the A < 0 cycle, e.g., at energies < ~ 80 MeV the spectra with the latitude dependence of s is a factor of ~ 2 higher than without a latitude dependence at 90 AU in the A < 0 cycle, while this factor can be as low as 1.4 in the opposite drift cycle. At 1 AU the qualitative picture looks similar at both latitudes, confirming the small latitudinal gradients observed with Ulysses (Heber et al., 1996).

In a nutshell, the effect of the latitude dependence of the compression ratio on GCR protons is more pronounced at low energies and it reduces modulation at these energies, while at higher energies there are no significant measurable effects. The analysis at Earth requires that the latitude dependence of the compression ratio may not influence GCR intensities close to the Sun in both polarity cycles.

4.5 The effects of the latitude dependent compression ratio and injection efficiency on ACR proton spectra

Diffusive shock acceleration resulting from an infinite plane shock always gives rise to a power law spectrum with spectral index given by $\gamma = (3s/s\text{-}1)$, that depends only on the compression ratio s, e.g., for a strong shock with $s = 4.0$, the differential intensity $J \propto E^{(-\gamma+2)/2} = E^{-1}$, with E the kinetic energy (e.g., Steenkamp, 1995; Langner,

2004). The modulation effects of the latitude dependence of s and the injection efficiency on ACR protons have not been shown before.

For the ACR protons, a source is injected at the TS position, first with the same value over all latitudes at an energy of ~ 86.0 KeV as a delta function with arbitrary magnitude, and secondly a latitude dependence is assumed as in Figure 4.3. The solutions are independent of the injection energy as long as it is lower than the acceleration cut-off energy (Steenkamp, 1995; Langner, 2004).

In this section, the computational results are focused on three issues about the effects of the latitude dependence of s and the injection efficiency of the ACRs: (1) The power-law energy dependence of the ACR spectra; (2) The enhancement of the cosmic-ray intensity, a "bump", just below the cut-off (or roll-over) energy of the ACR, and (3) the high-energy cut-off (roll-over) of the shock spectra because of the well-known curvature (shock radius) effect when $Vr_s / K_{rr} < 1$ (Moraal and Axford, 1983; Drury, 1983). To make clear the effects of each TS parameter, firstly the effects of the latitude dependence of s only are shown, secondly of the injection efficiency and then finally of the two parameters combined.

Shown in Figure 4.6 are the computed differential intensities for ACRs protons as a function of kinetic energy for both polarity cycles in the equatorial plane and θ = 55°, respectively, for solar minimum conditions. The energy spectra are shown at radial distances of 1, 50 and 90 AU and the differential intensities as a function of radial distance at energies of 0.016, 0.08 and 0.2 GeV, respectively. Two sets of spectra are shown, first without a latitude dependence (black lines) and then with a latitude dependence (red lines) of s only.

Concerning the first issue, it follows from the two top left panels of Figure 4.6 that the spectra at the TS in the equatorial plane of the two approaches have the same required spectral index because the latitude dependence produces s = 3.1 in this region. At θ = 55° the spectral indices differ, because for the latitude dependent s the shock spectrum (red lines) is much steeper than that without the latitude dependence, because of the assumed s = 1.8 instead of s = 3.1.

Concerning the second issue, the latitude dependence of s shifts in general the cut-off (roll-over) energies to lower energies for both polarity cycles in the equatorial plane, especially at θ = 55°. This lowering of the roll-over energy of the spectra is considered an improvement in the sense that these solutions with the latitude dependent s have a better

compatibility to ACR observations. In the inner heliosphere ($r < \sim 30$ AU) this roll-over of the spectra shifts to significant lower energies; the intensities for the latitude dependent s (red lines) are reduced by a factor of ~ 10 compared to the solutions without the latitude dependence, this difference is larger in the A > 0 cycle at both latitudes.

The radial intensity profiles are clearly different for the two approaches, with the largest difference at lower energies. At $\theta = 55°$, the difference between the radial intensities of the two approaches stay almost the same beyond the inner heliosphere at all energies of interest while in the equatorial plane this difference is more pronounced in the inner heliosphere and decreases towards the TS to even become zero at 0.016 GeV, remaining that way in the heliosheath.

It is striking that the latitude dependence of s causes a large reduction in ACR intensities at Earth, whereas for GCR the difference between the two approaches is found to be insignificant. This is expected because the latitude dependence of s should influence the ACRs more significantly than the GCR that get only moderately re-accelerated at the TS.

Concerning the third issue, an intensity enhancement visible as a "bump", that is a deviation of the power law at lower energies, below the cut-off (roll-over) energy, in this case below ~ 200 MeV in the TS spectra for the A < 0 cycle in the equatorial plane, is prominent only for the latitude independent s scenario (black line in the left panel of the second row). Similar features of the "bump" during A < 0 polarity cycles had been previously reported in numerical modeling of ACR acceleration (e.g., Steenkamp, 1995; Langner, 2004) but no profound discussion was given. Shown here is that for the solutions with the latitude dependence of s this "bump" is significantly reduced (red lines) in the equatorial plane. However, most interesting is that at $\theta = 55°$, the "bump" reappears in the A < 0 cycle for the spectrum at the TS with the latitude dependence of s (red line in the left panel of the last row). This ACR enhancement during the A < 0 cycle, now also evident at $\theta = 55°$, is the consequence of drifts combined with polar diffusion and diffusive shock acceleration at the TS.

Figure 4.7 is similar to Figure 4.6. Again two sets of spectra are shown, first without a latitude dependence (black lines) and then with a latitude dependence (red lines) of the injection efficiency only, in all solutions the compression ratio was taken to be $s = 3.2$ over all latitudes. As before, the cut-off (roll-over) energies in the equatorial plane are shifted to lower energies because the shock acceleration process is made less effective. The factor of

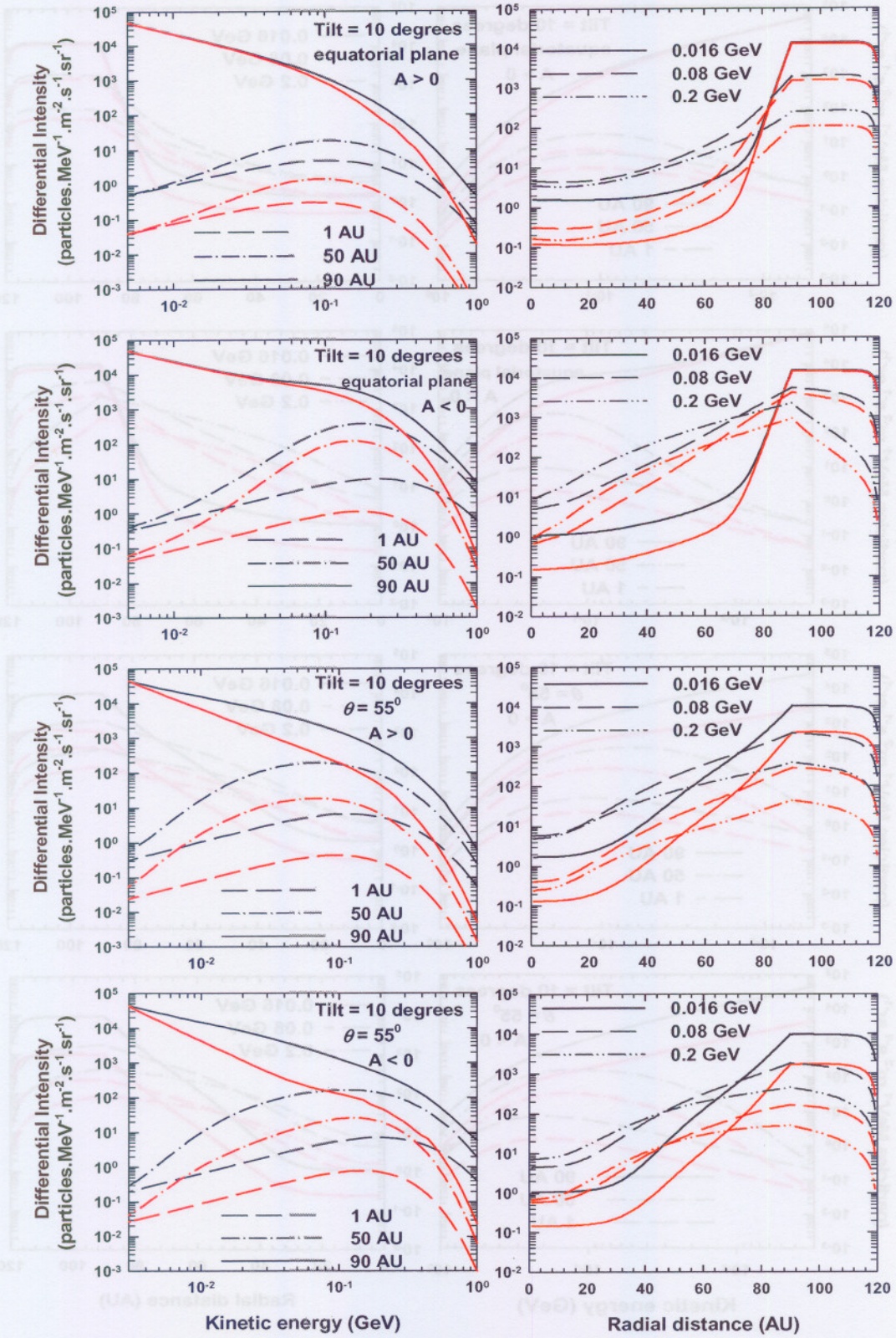

Figure 4.6. Left panels: Computed differential intensities for ACR protons as a function of kinetic energy for both polarity cycles and solar minimum condition at radial distances of 1, 50, and 90 AU in the equatorial plane and for θ = 55°, respectively. Right panels: Corresponding differential intensities as a function of radial distance for 0.016, 0.08 and 0.2 GeV, respectively. Two sets of solutions are shown, first without a latitude dependence (black lines) and second with a latitude dependence of s (red lines) only. TS is at 90 AU.

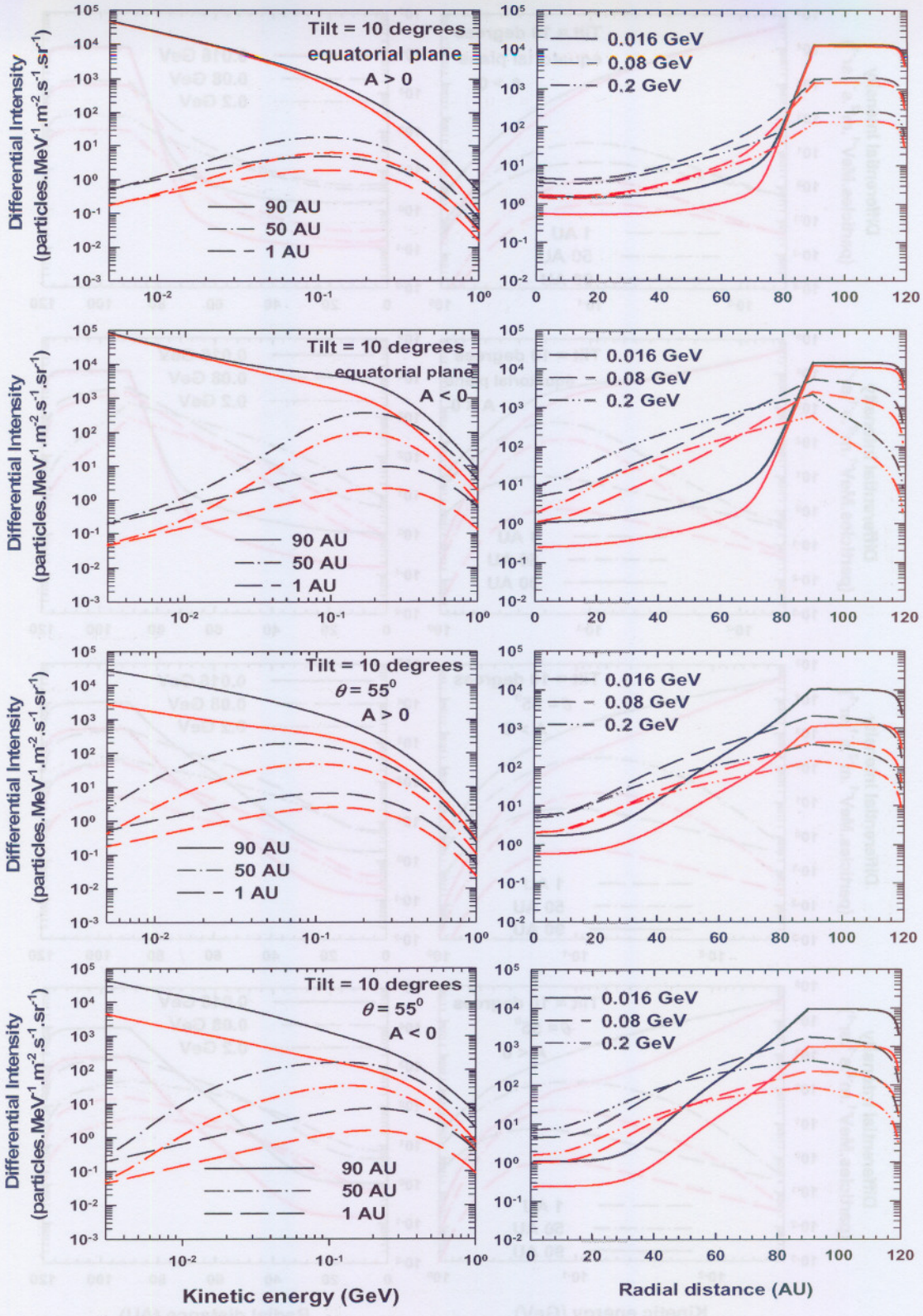

Figure 4.7. Left panels: Computed differential intensities for ACR protons as a function of kinetic energy for both polarity cycles and solar minimum condition at radial distances of 1, 50, and 90 AU in the equatorial plane and for θ = 55°, respectively. Right panels: Corresponding differential intensities as a function of radial distance for 0.016, 0.08 and 0.2 GeV, respectively. Two sets of solutions are shown, first without a latitude dependence (black lines) and second with a latitude dependence of only the injection efficiency (red lines). The TS is at 90 AU and the compression ratio is fixed at s = 3.2.

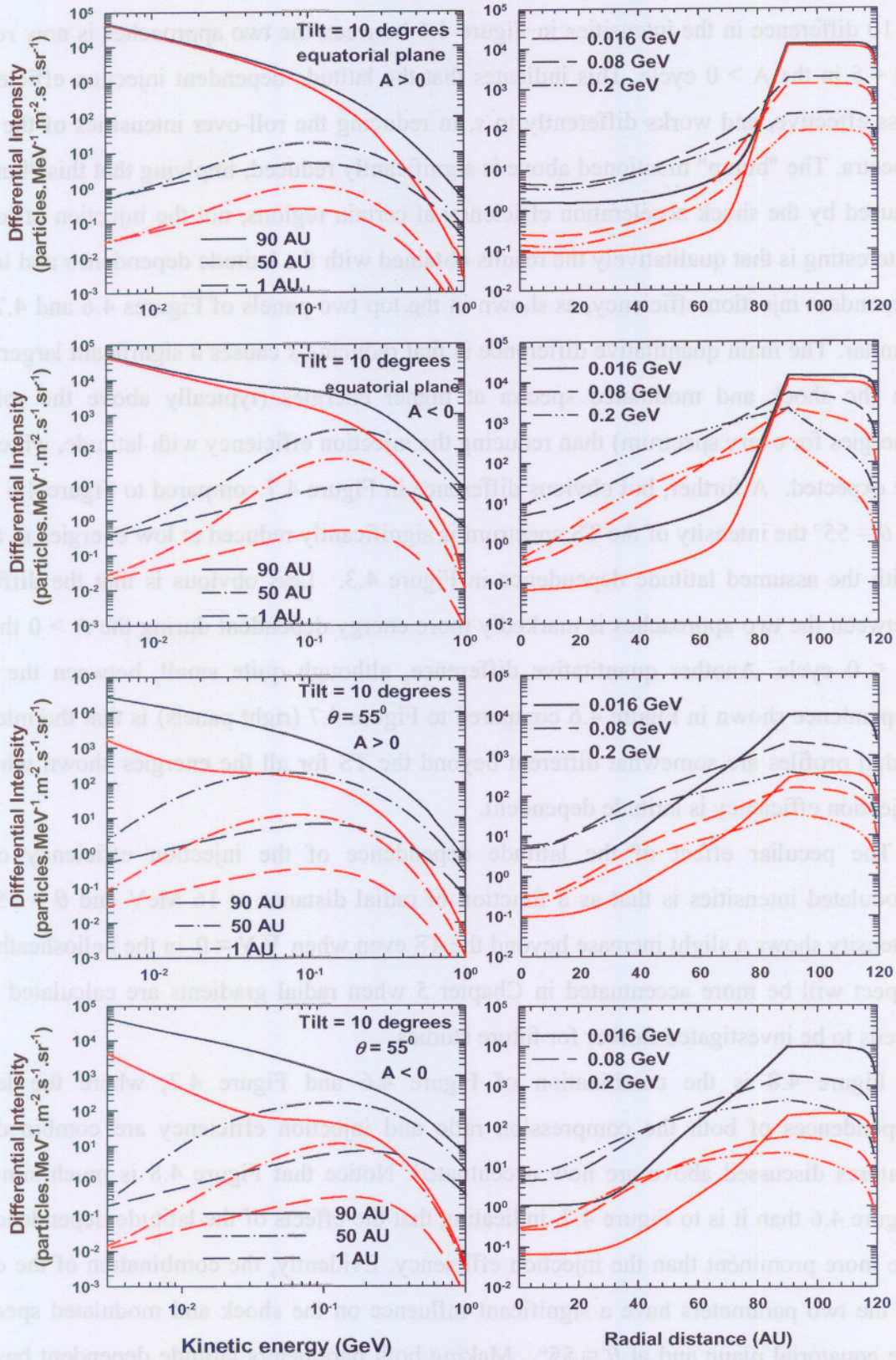

Figure 4.8. Similar to Figures 4.6 and 4.7 but now with a latitude dependence for both the compression ratio and the injection efficiency (red lines) compared to a latitude independent *s* and injection efficiency (black lines).

~ 10 difference in the intensities in Figure 4.6 between the two approaches is now reduced to ~ 5 in the A > 0 cycle. This indicates that the latitude dependent injection efficiency is less effective, and works differently to s, in reducing the roll-over intensities of the shock spectra. The "bump" mentioned above is significantly reduced, implying that this "bump" is caused by the shock acceleration efficiency at certain regions, not the injection efficiency. Interesting is that qualitatively the results obtained with the latitude dependent s and latitude dependent injection efficiency, as shown in the top two panels of Figures 4.6 and 4.7, look similar. The main quantitative difference is that reducing s causes a significant larger effect on the shock and modulated spectra at higher energies (typically above the roll-over energies for every spectrum) than reducing the injection efficiency with latitude, which is to be expected. A further, but obvious difference in Figure 4.7 compared to Figure 4.6 is that at $\theta = 55°$ the intensity of the TS spectrum is significantly reduced at low energies in accord with the assumed latitude dependence in Figure 4.3. Less obvious is that the difference between the two approaches is markedly more energy dependent during the A > 0 than the A < 0 cycle. Another quantitative difference, although quite small, between the radial dependence shown in Figure 4.6 compared to Figure 4.7 (right panels) is that the intensity-radial profiles are somewhat different beyond the TS for all the energies shown when the injection efficiency is latitude dependent.

The peculiar effect of the latitude dependence of the injection efficiency on the modulated intensities is that as a function of radial distance at 16 MeV and $\theta = 55°$, the intensity shows a slight increase beyond the TS even when $\nabla.\mathbf{V} = 0$ in the heliosheath. This aspect will be more accentuated in Chapter 5 when radial gradients are calculated and it needs to be investigated further for future studies.

Figure 4.8 is the combination of Figure 4.6 and Figure 4.7, where the latitude dependences of both the compression ratio and injection efficiency are combined. The features discussed above are now accentuated. Notice that Figure 4.8 is much similar to Figure 4.6 than it is to Figure 4.7, indicating that the effects of the latitude dependence of s are more prominent than the injection efficiency. Evidently, the combination of the effects of the two parameters have a significant influence on the shock and modulated spectra in the equatorial plane and at $\theta = 55°$. Making both parameters latitude dependent based on the HD results of Scherer et al. (2006), shown in Figure 4.2, has at least two major advances when keeping the main features of the V1 observations in mind, shown in Figure 4.1. First, the roll-over of the ACR spectra at the TS occurs at more realistic energies than with a latitude independent s. Second, the spectral shapes of the intensity at the TS at $\theta = 55°$,

shown in the two left side bottom panels in Figure 4.8, now have a form that is in general far more compatible to observations. This 'improvement' is taken as a strong indication that what V1 observed contains features of the TS shown and discussed here.

4.6 Effects of a negative divergence of V in the heliosheath

In standard modulation models, the solar wind is assumed to decrease as $1/r^2$ beyond the TS which implies that no additional acceleration can occur beyond the shock and that adiabatic energy losses become insignificant, which may be an oversimplification (see e.g., Langner et al., 2003, 2004, 2006a; Florinski et al., 2004). It became apparent that the change of V in the heliosheath may be different than the previously assumed $V \propto 1/r^2$ (Baranov and Malama, 1993; Pauls et al., 1995; le Roux and Fichtner, 1997; Florinski et al., 2004), which seemingly was done mostly for practical reasons. For a detailed discussion see also Langner et al. (2006a, 2006b).

In the TPE, the $\nabla.\mathbf{V}$ term determines the energy losses and gains of charged particles in the heliosphere, e.g., in the heliosheath $\nabla.\mathbf{V} < 0$ implies adiabatic heating, the further acceleration of particles; $\nabla.\mathbf{V} > 0$ in the heliosheath implies adiabatic energy losses, the deceleration of particles; and finally $\nabla.\mathbf{V} = 0$ with $V \propto 1/r^2$ implies that neither energy losses nor gains for charged particles can then play a role in the heliosheath, as was shown in Figures 4.6 to 4.8. Inside the TS (upwind), adiabatic energy losses occur because $\nabla.\mathbf{V} > 0$ everywhere, the amount increasing significantly towards the Sun. This produces the well-known power-law modulated GCR spectra at Earth and on which the Force-Field modulation approach is based (discussed in detail by Potgieter, 1984, and recently by Caballero-Lopez and Moraal, 2004). These spectral features at 1 AU are also evident in Figures 4.6 to 4.8, whereas at 50 AU the adiabatic losses are evidently much less.

Langner et al. (2006a, 2006b) studied the different scenarios for the global solar wind speed in the heliosheath for GCR and ACR protons with a 2D TS model, using as input the different solar wind speed profiles and the shape of the heliosphere from a 3D hydrodynamic model developed by Borrmann (2005); see also Borrmann and Fichtner (2005). They found that the stronger radial decrease of V in the heliosheath than $1/r^2$ causes an increase in radial intensities of the ACR protons beyond the TS. This helps to explain the

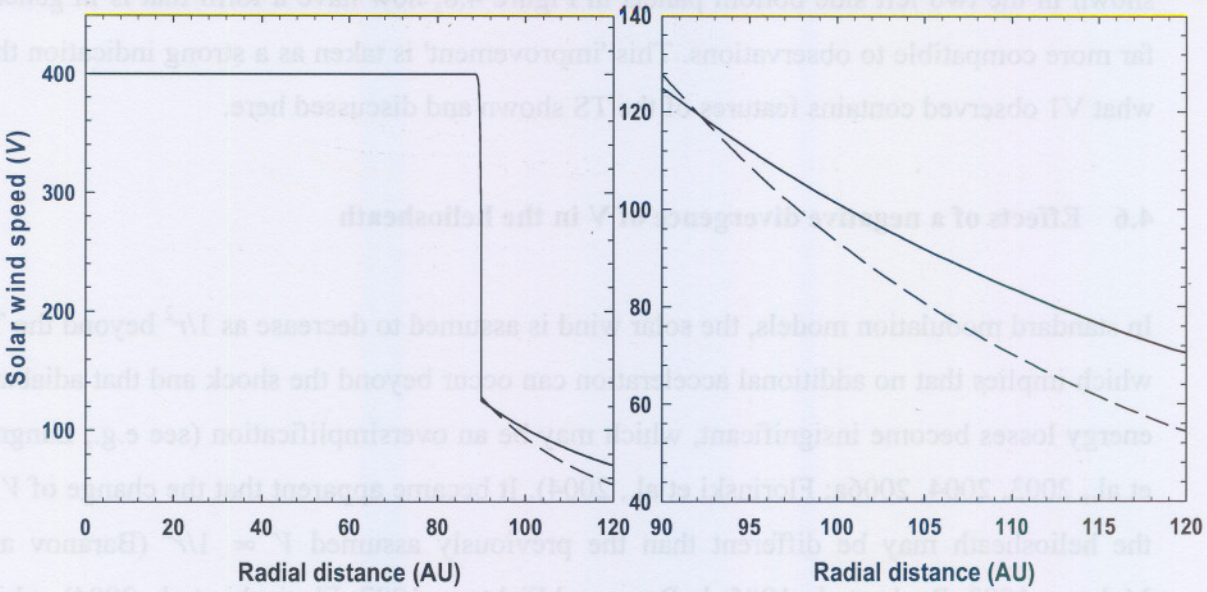

Figure 4.9. Left panel: Solar wind speed V as a function of radial distance in the equatorial plane for two scenarios, first with constant s and with $V \propto 1/r^2$ in the heliosheath (solid lines), and then with a varying s over latitude (see Figure 4.3) and with $V \propto 1/r^3$ in the heliosheath (dashed lines). The right panel shows the same as the left panel, emphasizing the behaviour of V in the heliosheath, 90-120 AU.

intensities of the ACRs as measured by V1 that continued to grow beyond the TS. The stronger radial decrease of V in the heliosheath and the latitude dependence of both s and the injection efficiency seem necessary to bring the modeling results closer to the observations.

Figure 4.9 shows the solar wind speed V as a function of radial distance in the equatorial plane for two scenarios, first with a constant s and with $V \propto 1/r^2$ in the heliosheath (90-120 AU), and then with a varying s over latitude as shown in Figure 4.3 and with $V \propto 1/r^3$ in the heliosheath. The right panel is the same as the left panel, emphasizing what happens in the heliosheath. The stronger radial decrease $V \propto 1/r^3$ in the heliosheath, as shown in Figure 4.9, is combined with the latitude dependence of s and the injection efficiency to study the subsequent effects on the modulation of ACRs in the heliosphere. These effects are then compared to the solutions with $V \propto 1/r^2$ in the heliosheath and without a latitude dependence of both s and the injection efficiency.

Shown in Figure 4.10 are the computed differential intensities for ACR protons as a function of kinetic energy for both polarity cycles at solar minimum conditions. The energy spectra are shown at radial distances of 1, 50 and 90 AU and the differential intensities as a

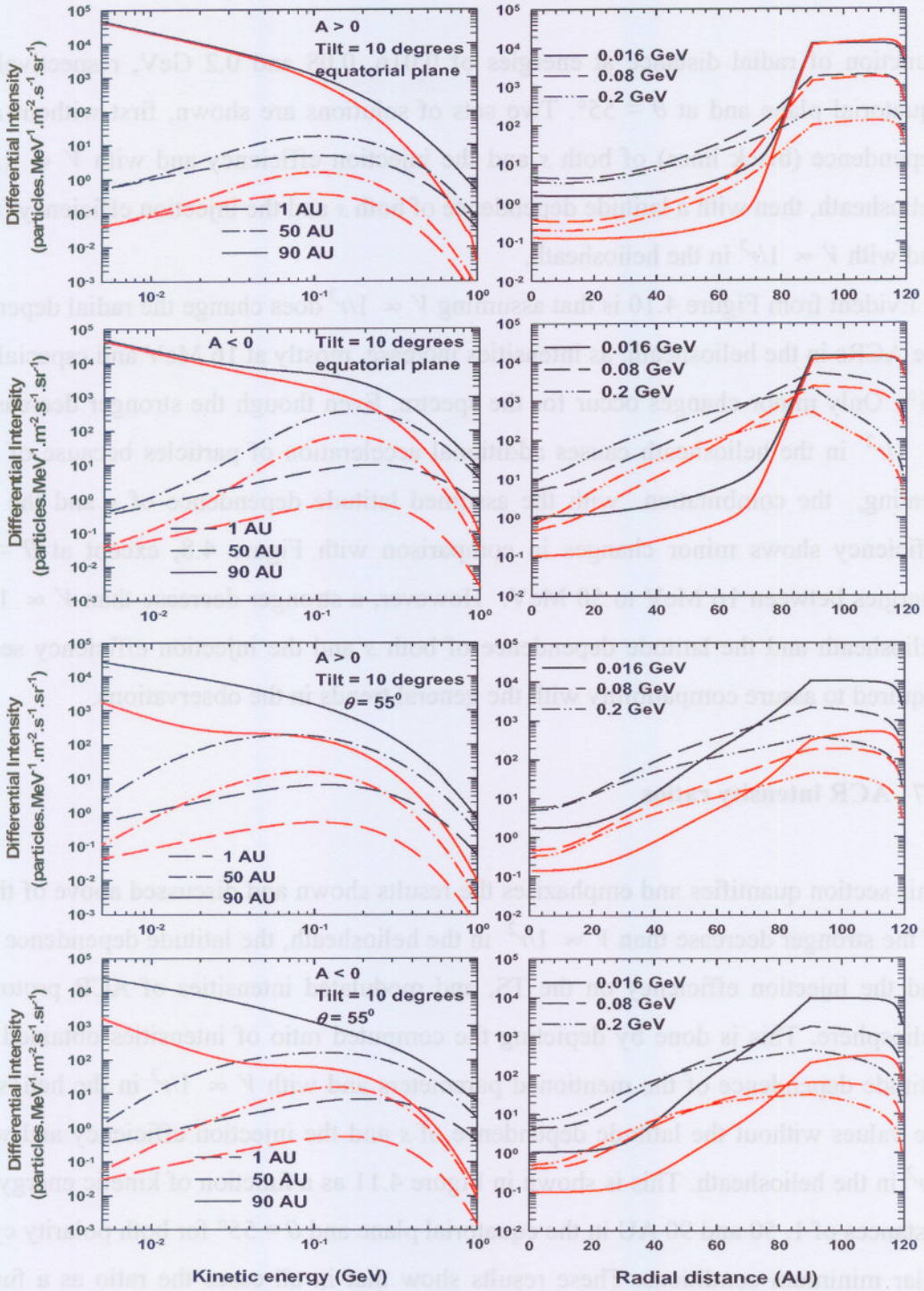

Figure 4.10. Left panels: Computed differential intensities for ACR protons as a function of kinetic energy for both polarity cycles and solar minimum condition at radial distances of 1, 50, and 90 AU in the equatorial plane and for θ = 55°, respectively. Right panels: Corresponding differential intensities as a function of radial distance for 0.016, 0.08 and 0.2 GeV, respectively. Two sets of solutions are shown, first without a latitude dependence (black lines) and with $V \propto 1/r^2$ in the heliosheath, and then with a latitude dependence of both s and for the injection efficiency (red lines), together with $V \propto 1/r^3$ in the heliosheath. The TS is at 90 AU.

function of radial distance at energies of 0.016, 0.08 and 0.2 GeV, respectively, in the equatorial plane and at $\theta = 55°$. Two sets of solutions are shown, first without a latitude dependence (black lines) of both s and the injection efficiency and with $V \propto 1/r^2$ in the heliosheath, then with a latitude dependence of both s and the injection efficiency (red lines) and with $V \propto 1/r^3$ in the heliosheath.

Evident from Figure 4.10 is that assuming $V \propto 1/r^3$ does change the radial dependence of the ACRs in the heliosheath, as intensities increase, mostly at 16 MeV and especially at $\theta = 55°$. Only minor changes occur for the spectra. Even though the stronger decrease than $V \propto 1/r^2$ in the heliosheath causes additional acceleration of particles because of adiabatic heating, the combination with the assumed latitude dependence of s and the injection efficiency shows minor changes in comparison with Figure 4.8, except at $\theta = 55°$ for energies between 16 MeV to 50 MeV. However, a stronger decrease than $V \propto 1/r^2$ in the heliosheath and the latitude dependence of both s and the injection efficiency seem to be required to assure compatibility with the general trends in the observations.

4.7 ACR intensity ratios

This section quantifies and emphazises the results shown and discussed above of the effects of the stronger decrease than $V \propto 1/r^2$ in the heliosheath, the latitude dependence of both s and the injection efficiency on the TS, and modulated intensities of ACR protons in the heliosphere. This is done by depicting the computed ratio of intensities obtained with the latitude dependence of the mentioned parameters and with $V \propto 1/r^3$ in the heliosheath, to the values without the latitude dependence of s and the injection efficiency and with $V \propto 1/r^2$ in the heliosheath. This is shown in Figure 4.11 as a function of kinetic energy at radial distances of 1, 50 and 90 AU in the equatorial plane and $\theta = 55°$ for both polarity cycles and solar minimum conditions. These results show that in all cases the ratio as a function of kinetic energy is larger than unity in the equatorial plane, whereas at $\theta = 55°$ the ratio becomes larger than 10. Clearly the difference in the two approaches is more pronounced at $\theta = 55°$ than in the equatorial plane and for the $A < 0$ cycle than for the $A > 0$ cycle. The ratios approach unity in the equatorial plane with decreasing energy for both polarity cycles but with a somewhat different energy dependence. (See also Langner and Potgieter, 2006).

In the equatorial plane at 50 AU the latitude dependence of s and the injection efficiency and with $V \propto 1/r^3$ in the heliosheath cause significant modulation in the $A > 0$ cycle, because in the opposite drift cycle at 50 AU the ratio between the two approaches is smaller

than 10 at energies < ~ 300 MeV. This may be due to the fact that drifts along the shock for A < 0 cycle are also in the same direction as the diffusion caused by $K_{\perp\theta}$ and this could enhance the effect in this cycle because particles can spend more time closer to the shock front (Langner, 2004). But, at $\theta = 55°$ the ratio of the two approaches at 1 AU is smaller than at 50 and 90 AU at energies < ~ 80 MeV in both polarity cycles, while in the equatorial plane it is large in both cycles and at all energies, indicating that the changes made in the model are more pronounced in the inner heliosphere in the equatorial plane and in the outer heliosphere at $\theta = 55°$. The ratios at all radial distances converge at higher energies in both cycles.

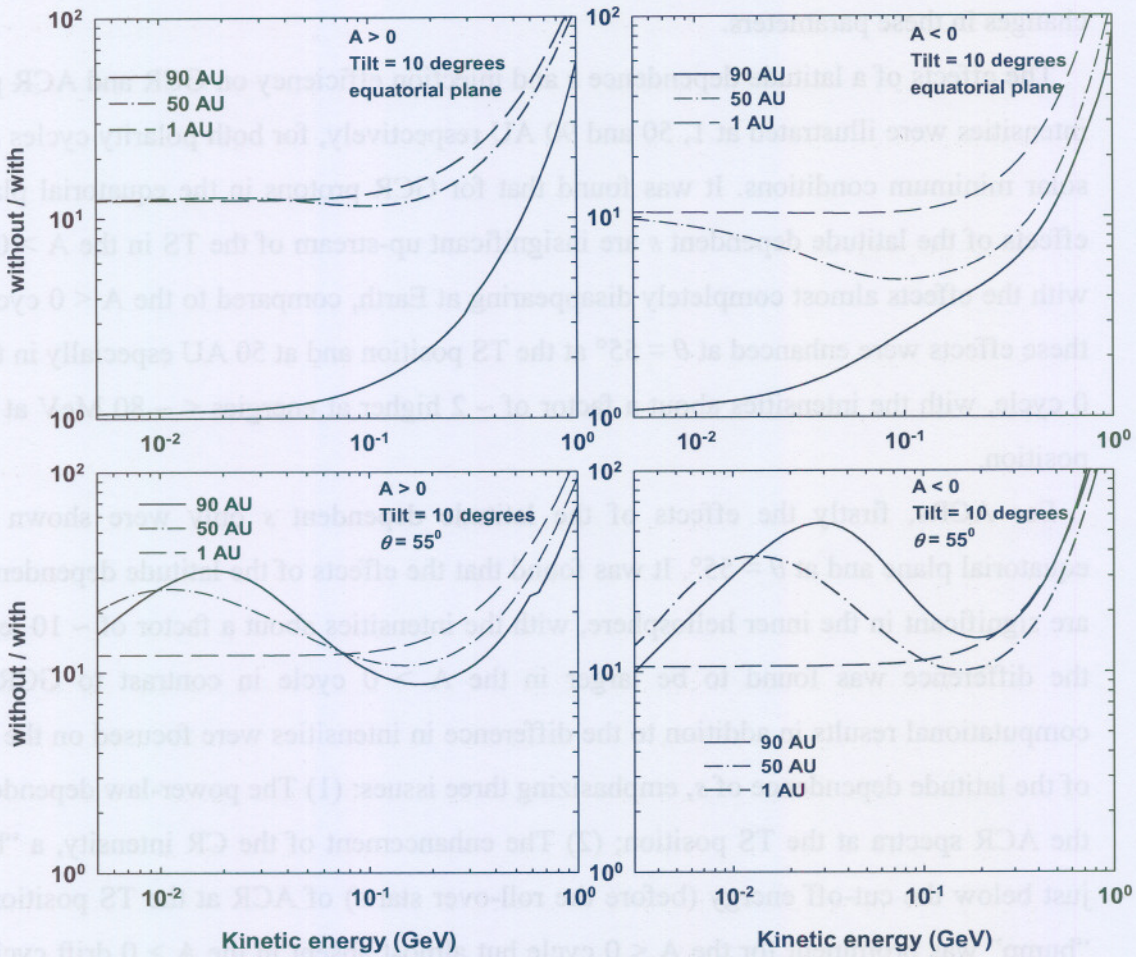

Figure 4.11. Intensity ratios for ACR protons as a function of kinetic energy at radial distances of 1, 50 and 90 AU in the equatorial plane (top panels) and $\theta = 55°$ (bottom panels) for both polarity cycles and solar minimum conditions. The ratios are computed using the intensities with $V \propto 1/r^3$ in the heliosheath and with the latitude dependence of s and the injection efficiency (with-label), and the intensities with $V \propto 1/r^2$ in the heliosheath and without the latitude dependence of s and the injection efficiency (without-label).

4.8 Summary and conclusions

In this Chapter new relations of the latitudinal dependences of the solar wind termination shock's compression ratio and the injection efficiency (or the ACR source) were established to enable improved modelling of GCR and in particular ACR protons intensities in the heliosphere. These two parameters are strong in the equatorial plane but weak at the poles as shown in Figure 4.3. Furthermore, the solar wind speed in the heliosheath was allowed to decrease stronger than $V \propto 1/r^2$. The effects of these parameters were studied using a 2D symmetric TS modulation model developed by Langner (2004). However, it should be emphasized that it is beyond the scope of this work to try to fit V1 observations in the heliosheath, the main purpose was to study the main modulation effects associated with changes in these parameters.

The effects of a latitude dependence s and injection efficiency on GCR and ACR protons intensities were illustrated at 1, 50 and 90 AU respectively, for both polarity cycles and for solar minimum conditions. It was found that for GCR protons in the equatorial plane the effects of the latitude dependent s are insignificant up-stream of the TS in the A > 0 cycle, with the effects almost completely disappearing at Earth, compared to the A < 0 cycle. But these effects were enhanced at $\theta = 55°$ at the TS position and at 50 AU especially in the A < 0 cycle, with the intensities about a factor of ~ 2 higher at energies < ~ 80 MeV at the TS position.

For ACRs, firstly the effects of the latitude dependent s only were shown in the equatorial plane and at $\theta = 55°$. It was found that the effects of the latitude dependence of s are significant in the inner heliosphere, with the intensities about a factor of ~ 10 less, and the difference was found to be larger in the A > 0 cycle in contrast to GCRs. The computational results in addition to the difference in intensities were focused on the effects of the latitude dependence of s, emphasizing three issues: (1) The power-law dependence of the ACR spectra at the TS position; (2) The enhancement of the CR intensity, a "bump", just below the cut-off energy (before the roll-over starts) of ACR at the TS position. This "bump" was prominent for the A < 0 cycle but almost absent in the A > 0 drift cycle, also found by Steenkamp (1995) and Langner (2004). le Roux et al. (1996) and later also Florinski and Jokipii (2003) showed that a similar "bump" (more correctly a change in the shock spectral index with increasing energy) could also be obtained in purely spherically symmetric geometry with no drifts. They attributed this effect to increased shock acceleration efficiency under certain conditions; and (3) high-energy cut-off of the shock

spectra. The two solutions, with and without the latitude dependence of s, were found to have the same required spectral index in the equatorial plane, but at $\theta = 55°$ the latitude dependence of s produces a much steeper spectra. For the cut-off energies, this latitude dependence was found to shift cut-off energies to lower energies, and more significantly at $\theta = 55°$. The "bump" was found to be largely diminished in the equatorial plane even in the $A < 0$ cycle. At $\theta = 55°$ this "bump" was found to reappear only in the $A < 0$ cycle.

Secondly, s was kept constant over latitudes and only the injection efficiency was varied. The intensities inside off the TS were found to be reduced by a factor of ~ 5 and this factor was found to be large in the $A < 0$ cycle in contrast to the discussion above. The cut-off energies were found to have been shifted to lower energies as before. The "bump" before the cut-off energy was found to have been wiped out even at $\theta = 55°$ in the $A < 0$ cycle.

Thirdly, the latitude dependences of s and the injection efficiency were combined. It was found that the cut-off energies shifted further to lower energies. The "bump" before the cut-off energies was found to have been wiped out in the equatorial plane, but it reappeared at $\theta = 55°$ and this time in both drift cycles. This was found to be similar to what Florinski and Jokipii (2003) found using a purely spherically symmetric geometry with no drifts.

Finally, the latitude dependences of s and the injection efficiency were combined with the stronger decrease of V in the heliosheath, $V \propto 1/r^3$. The qualitative picture was found to look similar to the one when only the latitude dependence of s and the injection efficiency was assumed and with $V \propto 1/r^2$ in the heliosheath, except as a function of radial distance and at 16 MeV where the intensities showed a slight increase in the heliosheath that is obviously caused by the negative divergence of V.

In the next Chapter the effects of the latitude dependence of s and the injection efficiency, and the stronger decrease of V than $1/r^2$ in the heliosheath, will be illustrated on the radial and latitudinal CR intensity gradients.

Chapter 5

Cosmic ray latitudinal and radial gradients

5.1 Introduction

In the previous chapter the newly developed latitude dependence of the compression ratio of the TS and the injection efficiency of the ACR source at the TS was combined with both $V \propto 1/r^2$ and $V \propto 1/r^3$ in the heliosheath, the associated effects on modulation of GCR and ACR protons in the heliosphere were studied. In this chapter, the computed spectra and intensities are used to study these effects on the radial and latitudinal (polar) gradients of GCR and ACR protons. Such computations together with measurement of these gradients by space probes provide crucial information about the diffusion tensor and for our understanding of the modulation and propagation of charged particles in the HMF. This work is a theoretical study, hence the computations are not fine-tuned for the purpose of fitting observations.

5.2 Cosmic ray intensity gradients

The four modulation processes discussed in Chapter 3 combine to produce CR gradients in the heliosphere. The model generates the omni-directional distribution function, f, in the heliosphere as a function of two spatial coordinates, rigidity and time. To obtain quantities that are equivalent to those measured by cosmic ray detectors, the distribution function must be expressed as a differential intensity $J = P^2 f$.

The gradient in the intensity of CRs in the 2D heliosphere is defined as

$$\boldsymbol{g} = g_r \boldsymbol{e}_r + g_\theta \boldsymbol{e}_\theta = \frac{1}{f}\frac{\partial f}{\partial r}\boldsymbol{e}_r + \frac{1}{rf}\frac{\partial f}{\partial \theta}\boldsymbol{e}_\theta = \frac{1}{J}\frac{\partial J}{\partial r}\boldsymbol{e}_r + \frac{1}{rJ}\frac{\partial J}{\partial \theta}\boldsymbol{e}_\theta, \tag{5.1}$$

where $g_r = \frac{1}{f}\frac{\partial f}{\partial r} = \frac{1}{J}\frac{\partial J}{\partial r}$ and $g_\theta = \frac{1}{rf}\frac{\partial f}{\partial \theta} = \frac{1}{rJ}\frac{\partial J}{\partial \theta}$ are the radial and the latitudinal gradient respectively.

Observations concerning the values of these gradients and their rigidity dependence put severe constraints on the modulation model from the cosmic ray point of view.

5.2.1 The radial gradients

In the literature (see e.g. Potgieter et al., 1989) two types of radial gradients, namely the local and non-local gradient are defined. The local gradient is defined as the variation of the differential intensity ΔJ with the variation in radial distance Δr, and is given by

$$G_r = \frac{1}{J}\frac{\Delta J}{\Delta r}, \tag{5.2}$$

expressed in %/AU and can easily be computed at various energies and different positions in the heliosphere with numerical models. This local radial gradient is computed in this work. The accuracy with which G_r is computed is determined by the spatial grid size used in the numerical model ($\Delta r \to 0 \Rightarrow G_r \to g_r$). This local radial gradient is impossible to measure, so that a non-local or global radial gradient is calculated from observed intensities by spacecraft probes which are separated by relatively large differences in radial distances and latitudes from the Sun (e.g., Voyager 1 and 2, Ulysses and IMP8). This non-local or global radial gradient measured at positions $r_2 >> r_1$ with corresponding intensities J_2 and J_1 is defined as

$$G_r^* = \frac{\Delta \ln J}{\Delta r} = \frac{\ln(J_2/J_1)}{r_2 - r_1} = \frac{\ln(f_2/f_1)}{r_2 - r_1}. \tag{5.3}$$

This form of gradient may also be calculated from differential intensities for a particular energy bin, and is then called the non-local differential gradient. Since observational spatial gradients are difficult to calculate, because of the distribution of spacecraft in the heliosphere, care must always be taken when these observational gradients are interpreted and compared to modeling values.

Many authors reported on observed radial gradients and their time variation based on direct observations (e.g., Heber et al., 1993; Fujii and McDonald, 1999, 2001; Webber and Lockwood, 2004). Numerical calculations of these gradients have also been extensively illustrated (e.g., Potgieter, 1984; Potgieter et al., 1989; le Roux, 1990; Steenkamp, 1995; Ndiitwani, 2005) and can explain the basic and prominent features of the observations.

Fujii and McDonald (1999), as a typical example, studied the radial gradient variations of GCRs and ACRs protons as a function of radial distance using data from IMP 6, 7 and 8 at Earth, Voyager 1 and 2, and Pioneer 10 and 11 out to the heliocentric distance of 65 AU in the heliosphere. They showed that G_r^* for GCR protons increases with decreasing radial

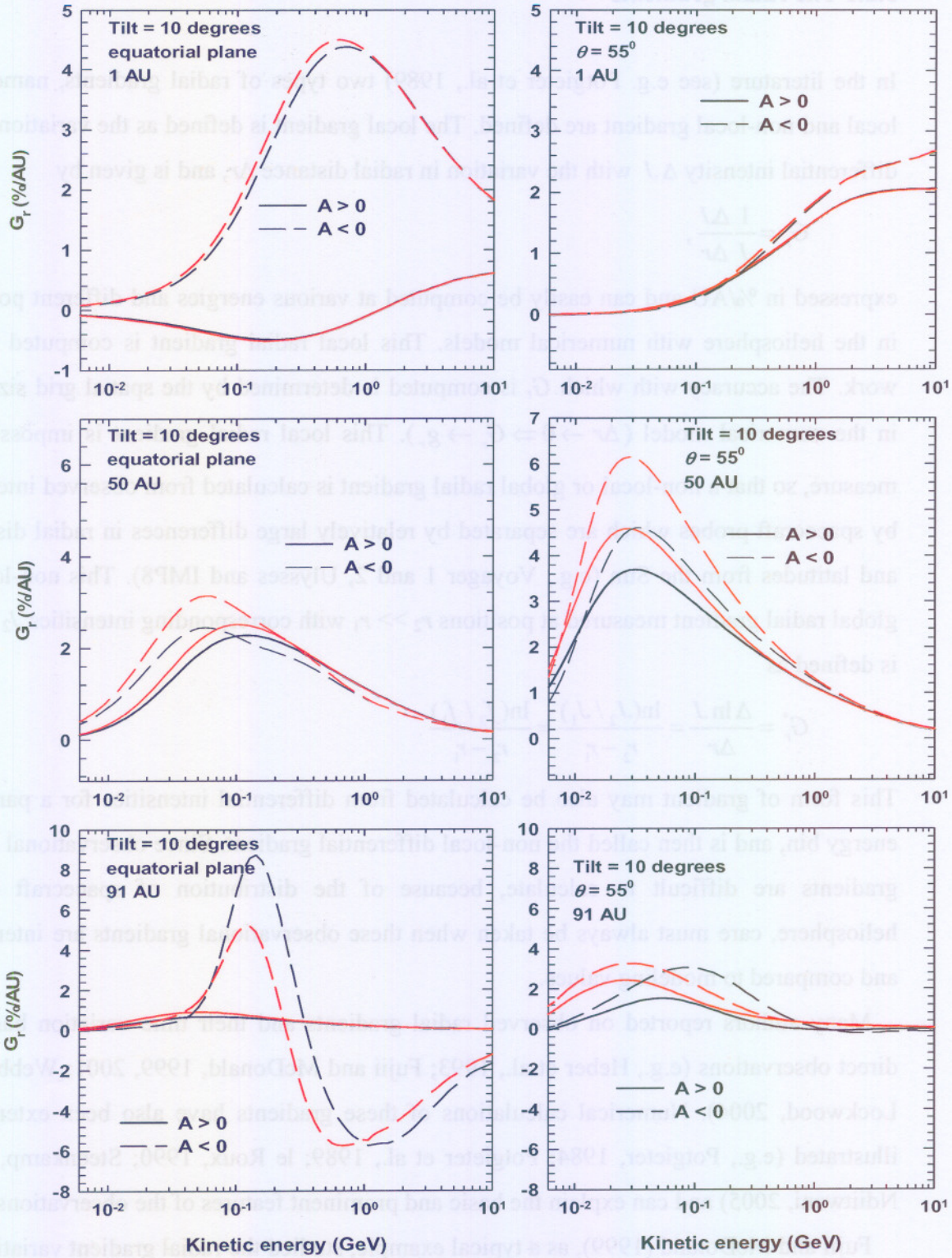

Figure 5.1. Left panels: Computed radial gradients for GCR protons, in %/AU, as a function of kinetic energy for both polarity cycles and for solar minimum conditions in the equatorial plane at 1, 50 and 91 AU respectively. Right panels: Similar but at $\theta = 55°$. Two sets of solutions are shown, first without a latitude dependence (black lines) and second with a latitude dependence of the compression ration s (red lines). The TS is at 90 AU and the HP, where the LIS is specified, is at 120 AU.

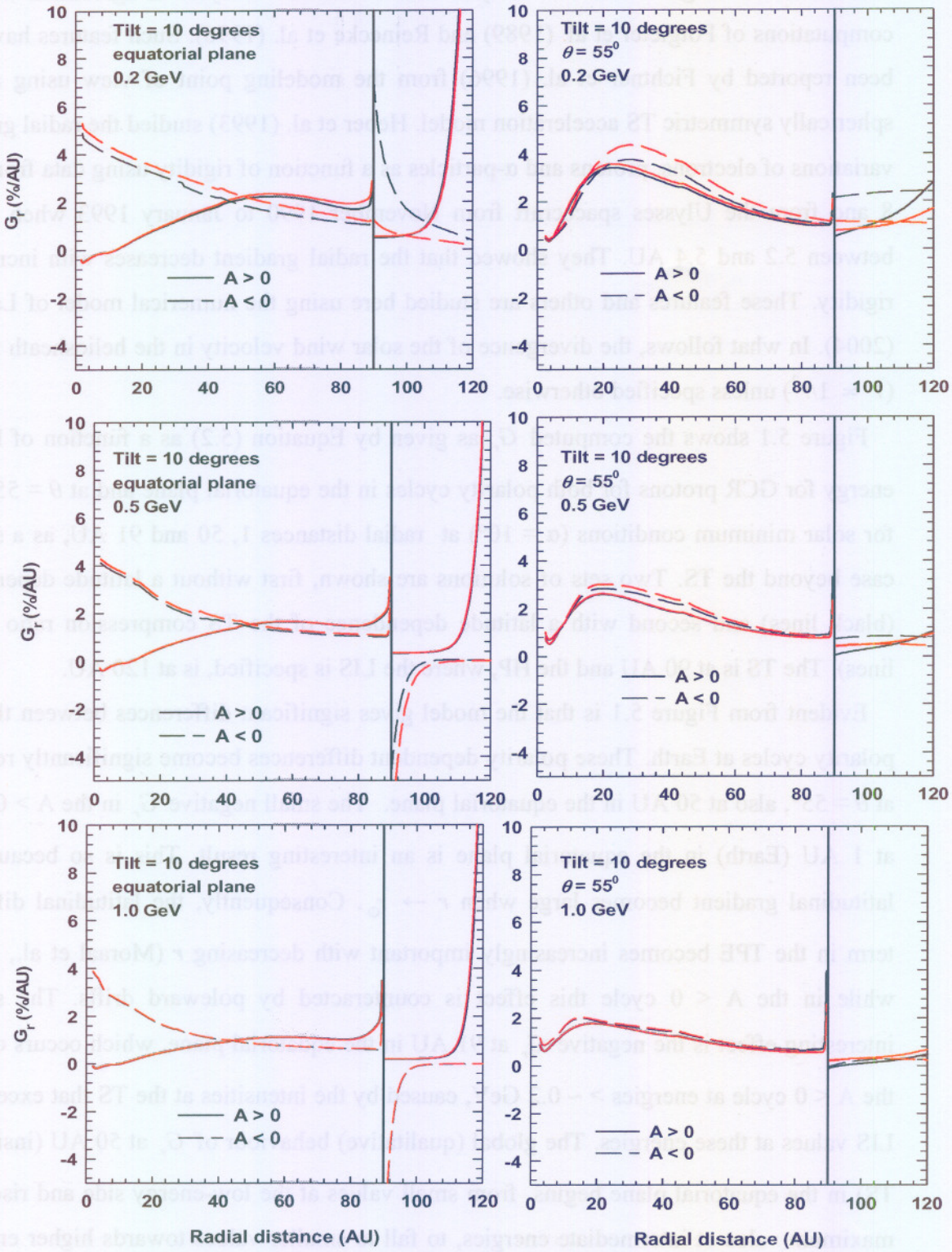

Figure 5.2. Left panels: Computed radial gradients for GCR protons, in %/AU, for both polarity cycles for solar minimum conditions as a function of radial distance in the equatorial plane at 0.2, 0.5 and 1.0 GeV respectively. Right panels: Similar but at $\theta = 55°$. Two sets of solutions are shown, first without a latitude dependence (black lines) and second with a latitude dependence of s (red lines). As before the TS is at 90 AU and the HP, where the LIS is specified, is at 120 AU.

distance and is larger in the A < 0 cycle than in the A > 0 cycle in agreement with the computations of Potgieter et al. (1989) and Reinecke et al. (1996). Such features have also been reported by Fichtner et al. (1996) from the modeling point of view using a non-spherically symmetric TS acceleration model. Heber et al. (1993) studied the radial gradient variations of electrons, protons and α-particles as a function of rigidity using data from IMP 8 and from the Ulysses spacecraft from November 1990 to January 1993 when it was between 5.2 and 5.4 AU. They showed that the radial gradient decreases with increasing rigidity. These features and others are studied here using the numerical model of Langner (2004). In what follows, the divergence of the solar wind velocity in the heliosheath is zero ($V \propto 1/r^2$) unless specified otherwise.

Figure 5.1 shows the computed G_r as given by Equation (5.2) as a function of kinetic energy for GCR protons for both polarity cycles in the equatorial plane and at $\theta = 55°$, and for solar minimum conditions ($\alpha = 10°$) at radial distances 1, 50 and 91 AU, as a special case beyond the TS. Two sets of solutions are shown, first without a latitude dependence (black lines) and second with a latitude dependence of the TS compression ratio s (red lines). The TS is at 90 AU and the HP, where the LIS is specified, is at 120 AU.

Evident from Figure 5.1 is that the model gives significant differences between the two polarity cycles at Earth. These polarity dependent differences become significantly reduced at $\theta = 55°$, also at 50 AU in the equatorial plane. The small negative G_r in the A > 0 cycle at 1 AU (Earth) in the equatorial plane is an interesting result. This is so because the latitudinal gradient becomes large when $r \rightarrow r_\odot$. Consequently, the latitudinal diffusive term in the TPE becomes increasingly important with decreasing r (Moraal et al., 2005), while in the A < 0 cycle this effect is counteracted by poleward drifts. The second interesting effect is the negative G_r at 91 AU in the equatorial plane, which occurs only in the A < 0 cycle at energies > ~ 0.2 GeV, caused by the intensities at the TS that exceed the LIS values at these energies. The global (qualitative) behaviour of G_r at 50 AU (inside the TS) in the equatorial plane begins from small values at the low-energy side and rises to a maximum value at intermediate energies, to fall to smaller values towards higher energies for both polarity cycles. This shape can be explained by looking at the spectra in the equatorial plane in the previous Chapter. At lower energies the adiabatic cooling dominates and the difference in the intensities at different positions in the heliosphere is reduced, while high energy particles are barely affected by the heliosphere. When drifts have a larger

influence, this behavior changes. G_r is significantly increased at 50 AU with $\theta = 55°$, compared to the equatorial plane at intermediate energies.

The effect of the latitude dependence of s is to increase G_r at $\theta = 55°$ but negligibly at 1 AU. At 91 AU in the equatorial plane the effect is to reduce it at intermediate energies in the A < 0 cycle. It is interesting to note that this latitude dependence of s shifts the maximum of G_r to lower energies and this is more pronounced at $\theta = 55°$ and 91 AU, but it does not alter its basic energy trend.

To further clarify how G_r for GCR protons changes throughout the heliosphere, it is also plotted as a function of radial distance in Figure 5.2, for both polarity cycles and for solar minimum conditions in the equatorial plane and at $\theta = 55°$ for energies of 0.2, 0.5 and 1.0 GeV, respectively. It follows from this figure that the dominant feature is that the model produces at the location of the TS a discontinuity in G_r caused by the presence of the peak in the re-accelerated GCR spectra at the TS. Notice that the nature of this effect varies significantly with particle energy e.g., in the A < 0 cycle at 0.2 GeV in the equatorial plane, the smallest gradient is found just up-stream of the shock whereas at energies of 0.5 and 1.0 GeV it is just outside the TS for both polarity cycles. This is in good agreement with the computations of Jokipii et al. (1993).

At radial distances of $r < \sim 40$ AU at all energies of interest, G_r in the equatorial plane is larger for the A < 0 cycle than for the A > 0 cycle. Beyond this distance G_r in the A > 0 cycle becomes marginally greater than in the A < 0 cycle. This behaviour in the A < 0 cycle is in good agreement to the observed gradients of Fuji and McDonald (1999) and Webber and Lockwood (2004). G_r remains larger in the A > 0 cycle than in the A < 0 cycle also in the heliosheath at 0.5 and 1.0 GeV. At the latitude traversed by V1, G_r is larger during the A < 0 cycle except in the inner heliosphere and in the outer heliosheath. In the heliosheath close to the HP, G_r increases abruptly in the A > 0 cycles in the equatorial plane because the intensity goes rapidly up to the corresponding LIS value. In the A < 0 cycle, it converges to zero when the HP is approached because the intensities in this cycle stay almost flat close to the HP. The latitude dependence of s constitutes rather small changes to the radial gradients in the equatorial plane but is large enough at $\theta = 55°$ to be considered meaningful.

Figure 5.3 is similar to Figure 5.1 but for ACR protons. Two sets of solutions are shown as before, but the second set is with a latitude dependence for s and for injection efficiency

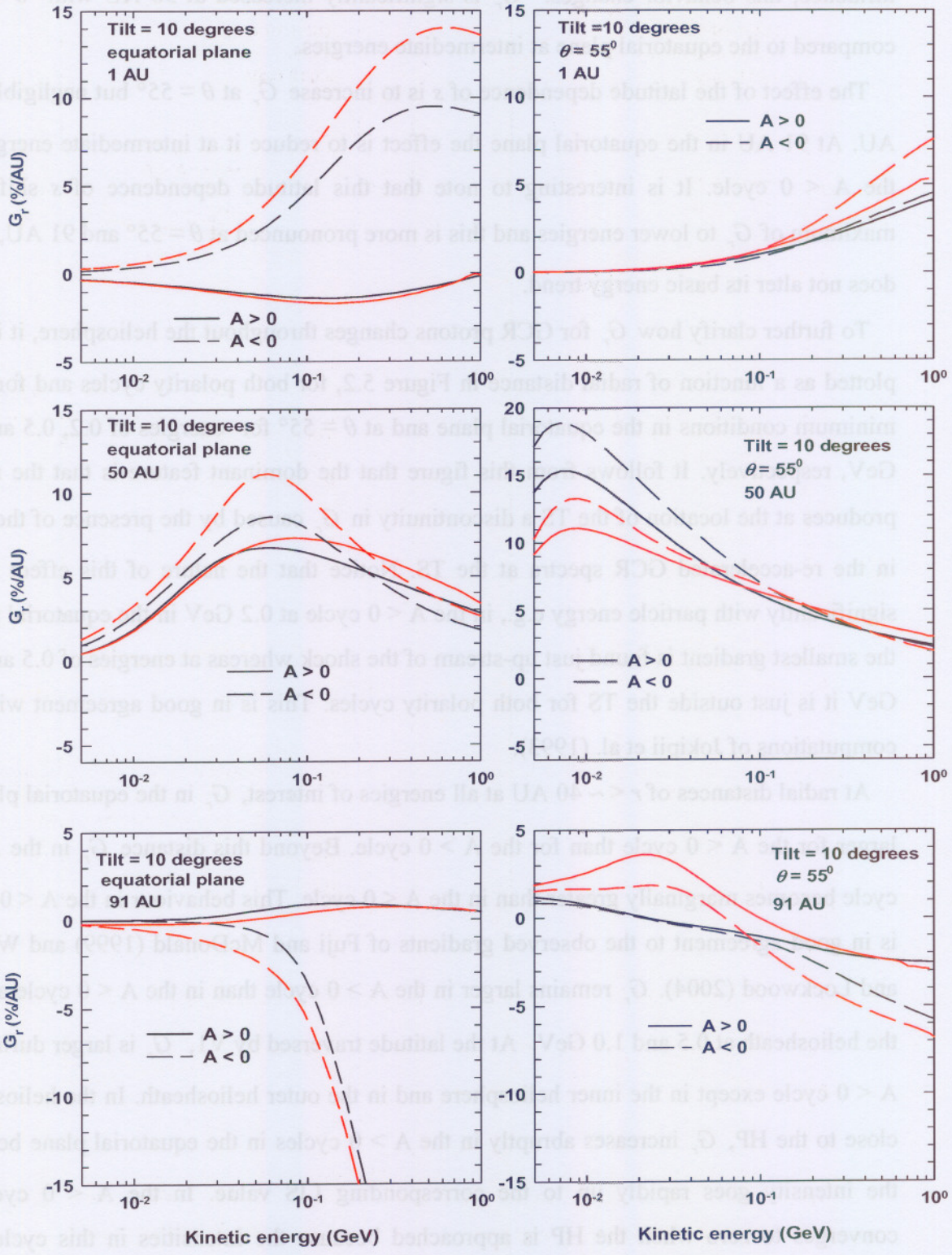

Figure 5.3. Left panels: Computed radial gradients for ACR protons, in %/AU, as a function of kinetic energy for solar minimum conditions and for both polarity cycles in the equatorial plane at 1, 50 and 91 AU respectively. Right panels: Similar but at $\theta = 55°$. As before two sets of solutions are shown, without a latitude dependence (black lines) and with a latitude dependence of both the compression ration s and the injection efficiency (red lines). The TS is at 90 AU.

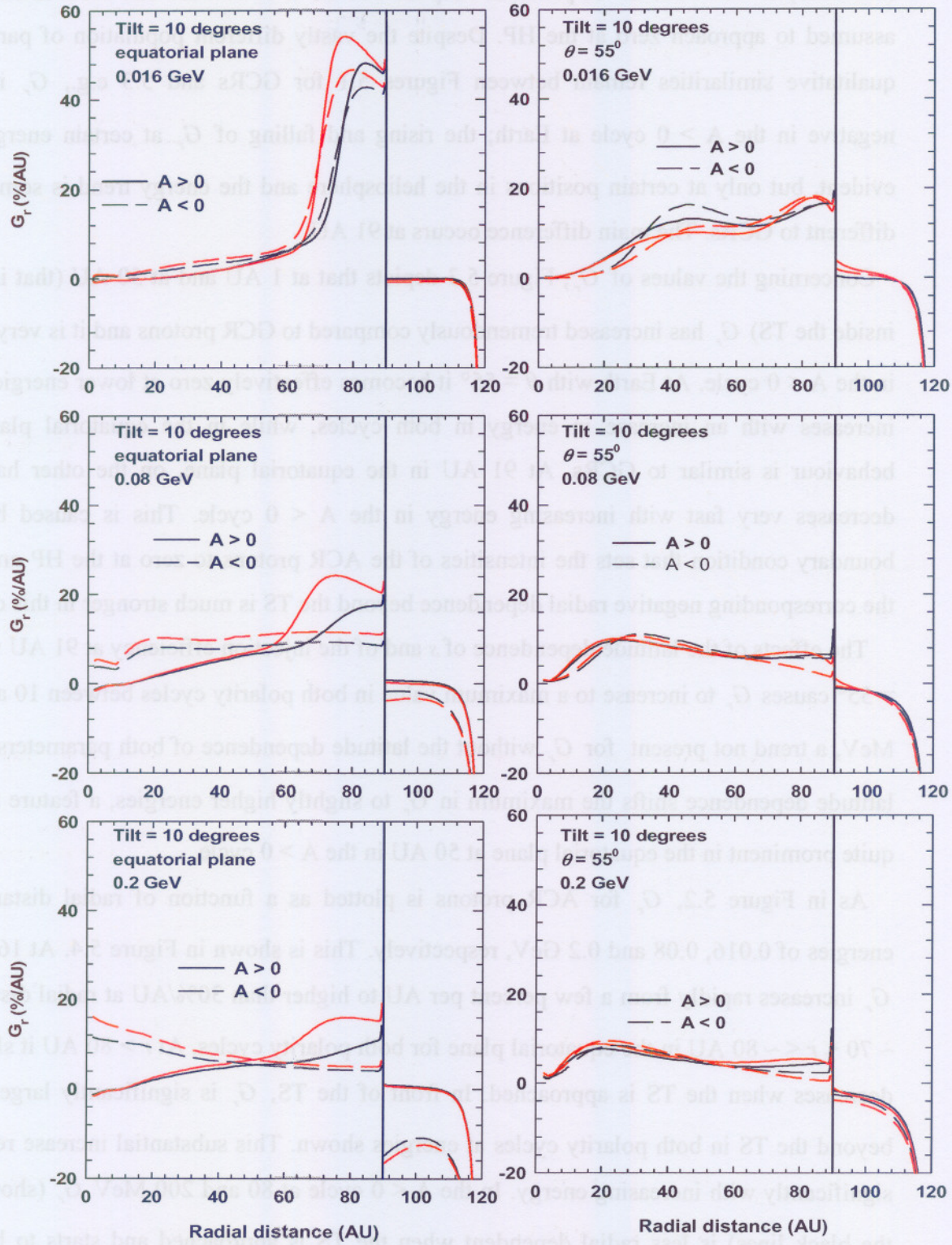

Figure 5.4. Left panels: Computed radial gradients for ACR protons as a function of radial distance for solar minimum conditions and for both polarity cycles in the equatorial plane at 0.016, 0.08 and 0.2 GeV respectively. Right panels: Similar but at $\theta = 55°$. The two sets of solutions are without a latitude dependence (black lines) and with a latitude dependence of both s and the injection efficiency (red lines). The TS is at 90 AU.

(red lines) as was done in the previous chapter. The TS is at 90 AU. The ACR intensity is assumed to approach zero at the HP. Despite the vastly different population of particles, qualitative similarities remain between Figures 5.1 for GCRs and 5.3 e.g., G_r is still negative in the A > 0 cycle at Earth; the rising and falling of G_r at certain energies is evident, but only at certain positions in the heliosphere and the energy trend is somewhat different to GCRs. The main difference occurs at 91 AU.

Concerning the values of G_r, Figure 5.3 depicts that at 1 AU and at 50 AU (that is well inside the TS) G_r has increased tremendously compared to GCR protons and it is very large in the A < 0 cycle. At Earth with $\theta = 55°$ it becomes effectively zero at lower energies and increases with an increase in energy in both cycles, while in the equatorial plane its behaviour is similar to GCRs. At 91 AU in the equatorial plane, on the other hand, it decreases very fast with increasing energy in the A < 0 cycle. This is caused by the boundary condition that sets the intensities of the ACR protons to zero at the HP and that the corresponding negative radial dependence beyond the TS is much stronger in this cycle.

The effects of the latitude dependence of s and of the injection efficiency at 91 AU with $\theta = 55°$ causes G_r to increase to a maximum value in both polarity cycles between 10 and 30 MeV, a trend not present for G_r without the latitude dependence of both parameters. This latitude dependence shifts the maximum in G_r to slightly higher energies, a feature that is quite prominent in the equatorial plane at 50 AU in the A > 0 cycle.

As in Figure 5.2, G_r for ACR protons is plotted as a function of radial distance at energies of 0.016, 0.08 and 0.2 GeV, respectively. This is shown in Figure 5.4. At 16 MeV G_r increases rapidly from a few percent per AU to higher than 30%/AU at radial distances $\sim 70 < r < \sim 80$ AU in the equatorial plane for both polarity cycles. At $r > 80$ AU it slightly decreases when the TS is approached. In front of the TS, G_r is significantly larger than beyond the TS in both polarity cycles at energies shown. This substantial increase reduces significantly with increasing energy. In the A < 0 cycle at 80 and 200 MeV G_r (shown by the black lines) is less radial dependent when the TS is approached and starts to have a similar behaviour as GCRs at 0.2 GeV, as one would anticipate.

The latitude dependence of s and the injection efficiency increases G_r inside the TS in the equatorial plane and this increase is large in the A > 0 cycle but only close to the TS, while in the A < 0 cycle this is evident up to the TS. Beyond the TS this latitude

dependence decreases G_r somewhat in both polarity cycles. Between the two approaches G_r do not differ in the inner heliosphere in the A > 0 cycle in the equatorial plane, while the corresponding intensities showed a factor ~ 10 difference (see Figure 4.8). At $\theta = 55°$, the changes introduced by the latitude dependence of s and the injection efficiency seem rather insignificant but the scale of the graphs in mind, the changes are not negligible at 16 MeV as the TS is approached. At energies greater than 0.016 GeV also at $\theta = 55°$, G_r (red lines) decreases when the TS is approached in the A < 0 cycle so that the difference reduces between G_r up-stream and down-stream of the TS. The global effect of the TS is to decrease G_r for ACR protons when crossing into the heliosheath. Beyond the TS it remains almost radially independent until when the boundary condition makes it very large negative. In the equatorial plane a stronger radial dependence occurs with increasing energy. Beyond the TS the radial gradients are without a significant HMF polarity dependence. This is in contrast to G_r showing a strong radial and polarity dependence in the inner heliosphere in the equatorial plane, but insignificant at $\theta = 55°$.

In Figure 5.5 two sets of solutions are depicted for G_r as a function of radial distance for ACR protons at energies of 0.016, 0.08 and 0.2 GeV similar to Figure 5.4, first without a latitude dependence (black lines) of both s and the injection efficiency and with $V \propto 1/r^2$ in the heliosheath, then with a latitude dependence of both s and the injection efficiency (red lines) and with $V \propto 1/r^3$ in the heliosheath similar to Figure 4.10. When $V \propto 1/r^3$ in the heliosheath, additional acceleration of ACR protons occurs in the heliosheath (Langner et al, 2006b). Therefore, interest in this figure is based on what happens in the heliosheath where this acceleration of particles occurs. As anticipated, G_r (red lines) remains positive at 16 MeV in both polarity cycles until very close to the HP where it drops sharply to negative values due to the boundary condition as explained before. However at energies of 0.08 and 0.2 GeV, as a rule of thumb, drifts and diffusion have a significant effect such that they somewhat cancel the effect of adiabatic acceleration in the heliosheath and completely in the A < 0 cycle at both energies, while in the A > 0 cycle this effect is still prominent in the equatorial plane, but only at radial distances up to ~ 10 AU away from the TS at $\theta = 55°$ and at 0.08 GeV. This is so because the adiabatic acceleration due to $V \propto 1/r^3$ in the heliosheath in this model is not extreme, hence its effects are seemingly more pronounced only at low energies and become easily unrecognizable at high energies especially when taking also

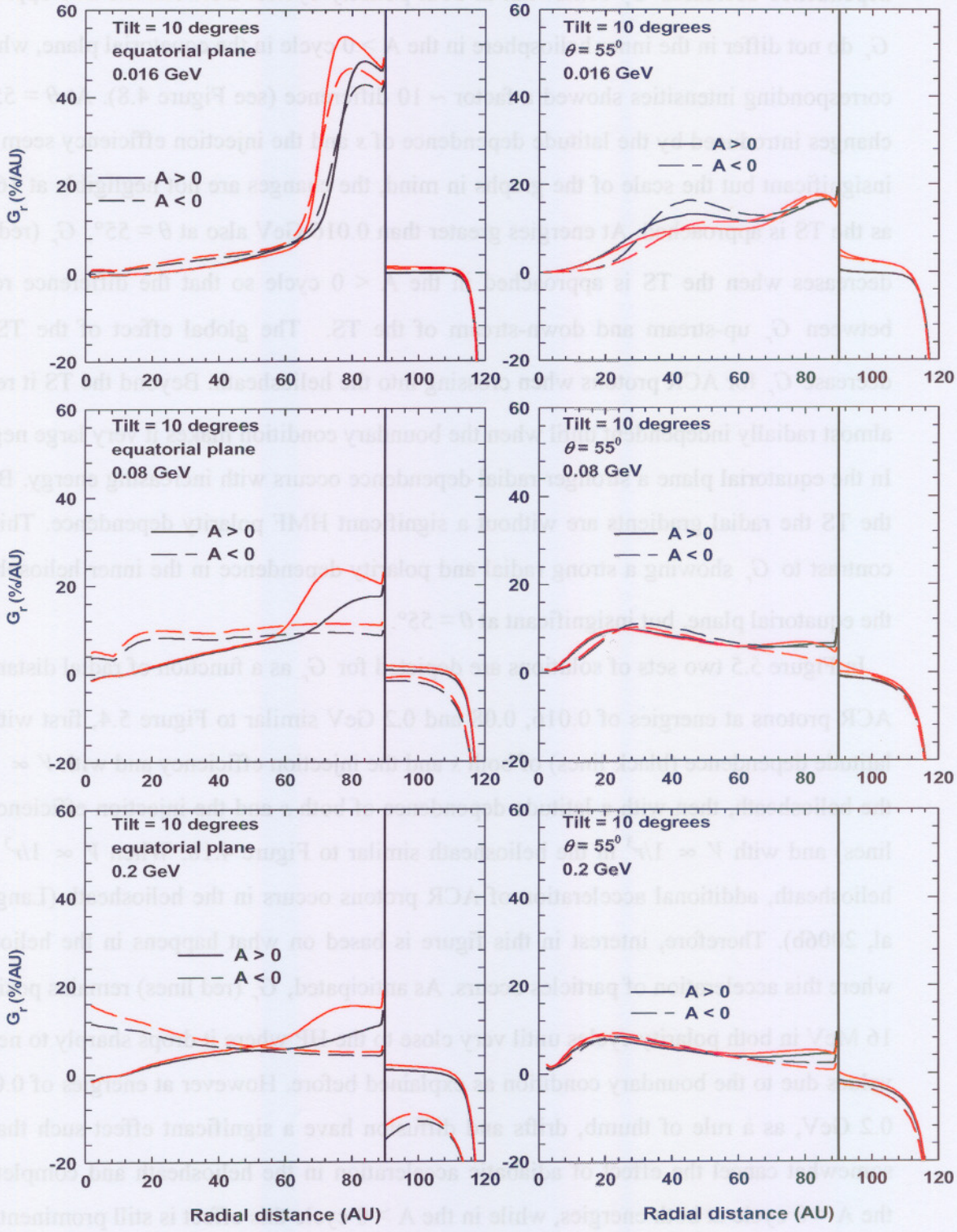

Figure 5.5. Left panels: Similar to Figure 5.4. Right panels: Similar but at $\theta = 55°$. Solutions are shown, first, without a latitude dependence (black lines) and with $V \propto 1/r^2$ in the heliosheath, and then with a latitude dependence of both s and for the injection efficiency (red lines), together with $V \propto 1/r^3$ in the heliosheath. The TS is at 90 AU.

other modulation effects into consideration. Over and above, it is interesting to note from Figure 5.5 that G_r (red lines) is always larger than G_r (black lines).

5.2.2 The latitudinal gradients

The local and non-local latitudinal (polar) gradients are defined following the same convention as before. The local gradient at a given radial distance r is given by

$$G_\theta = \frac{1}{rJ}\frac{\Delta J}{\Delta \theta}, \tag{5.4}$$

and is expressed in units of % $AU^{-1}degree^{-1}$. The non-local gradient between polar angles $\theta_2 > \theta_1$ is given by

$$G_\theta^* = \frac{1}{r}\frac{\Delta \ln J}{\Delta \theta} = \frac{1}{r}\frac{\ln(J_2/J_1)}{\theta_2 - \theta_1}. \tag{5.5}$$

Usually the observed latitudinal gradient, G_λ, in terms of heliolatitude, is related to G_θ by

$$G_\lambda = -rG_\theta, \tag{5.6}$$

expressed in %/degree.

In the A > 0 cycle, positively charged particles drift primarily inwards over the poles and outwards along the HCS. Their intensities are therefore in drift dominated models higher usually in the polar regions than in the equatorial plane, causing a negative G_θ (in terms of polar angle; but positive in terms of heliolatitude), while in the A < 0 cycle the drift direction reverses, so that G_θ is then positive. In contrast to the predictions of the earlier drift models for A > 0 cycles, small proton latitudinal gradients have been measured by Ulysses in the inner heliosphere (Heber et al., 1996; McKibben et al., 1996), and in particular at low energies. Burger et al. (2000) illustrated that in order to produce the correct magnitude and rigidity dependence of the observed latitudinal CR gradient measured by Ulysses, an enhanced latitudinal transport is required (see also Kota and Jokipii, 1995; Potgieter et al., 1997). In a Fisk-type HMF (Fisk, 1996), which is probably a more realistic HMF geometry for solar minimum conditions, the latitudinal transport is supposedly more effective than in a Parker field. To simulate this kind of latitudinal transport when a Parker field is used, $K_{\perp\theta}$ also needs to be enhanced.

In the rest of the chapter, the latitudinal gradients for ACR and GCR protons in the heliosphere are computed using the numerical model discussed in Chapter 3. These latitudinal gradients were found to be very small at large radial distances because of the

term $1/r$ in Equation (5.4), so that for illustrative purposes the computed gradients are multiplied by the appropriate radial distance r, and expressed in %/degree when plotted as a function of kinetic energy. This does not change the behaviour of the latitudinal gradients qualitatively, but quantitatively the computed values (magnitude) increase by a factor of r.

Figure 5.6 shows for GCR protons the computed rG_θ, hereafter referred to as the latitudinal (polar) gradient, as a function of kinetic energy for both polarity cycles in the equatorial plane and $\theta = 55°$ at radial distances 1, 50 and 91 AU, respectively, and for solar minimum conditions. As before, two sets of solutions are shown, a set without a latitude dependence (black lines) and a set with a latitude dependence of s (red lines). The TS is again at 90 AU and the HP, where the LIS is specified, is at 120 AU. Evident from this figure is that inside off the TS the polar gradient in the equatorial plane indicates a systematic behaviour and qualitative trend based on the two drift cycles and it clearly reverses sign with each polarity reversal. It is positive in the $A < 0$ cycle and negative in the $A > 0$ cycle at all energies. At energies less than ~ 10 MeV the difference between the two cycles dissipates as the polar gradients converge to zero. Its maximum value in the $A < 0$ cycle and minimum value in the $A > 0$ cycle shift to lower energies with increasing r; evident from comparing 50 AU with 1 AU. This happens also at 91 AU in the equatorial plane for the $A > 0$ cycle, but it does not show the mentioned pattern for the $A < 0$ cycle. Beyond the TS it is negative at energies < ~ 0.1 GeV in both cycles and approaches zero at high energies.

At $\theta = 55°$ and 1 AU, its qualitative behaviour look much similar to the equatorial plane, except that the maximum and minimum values of the latitudinal gradient in the $A < 0$ and $A > 0$ cycle are shifted to higher and lower energies respectively. What is interesting at $\theta = 55°$ is that the trend characterized by a negative latitudinal gradient at lower energies and nearly zero at high energies becomes evident at 50 AU, whereas in the equatorial plane this is only seen at 91 AU. This makes the polarity reversal dependence of the polar gradient for GCR protons, as explained before, significant only at energies greater than 0.1 GeV.

The latitude dependence of s has almost no effect on the polar gradient of GCR protons at 1 AU in both polarity cycles, but the effect increases with radial distance and become more prominent at lower energies. At 91 AU in the equatorial plane, the peculiar behaviour is again prominent for the $A < 0$ cycle only.

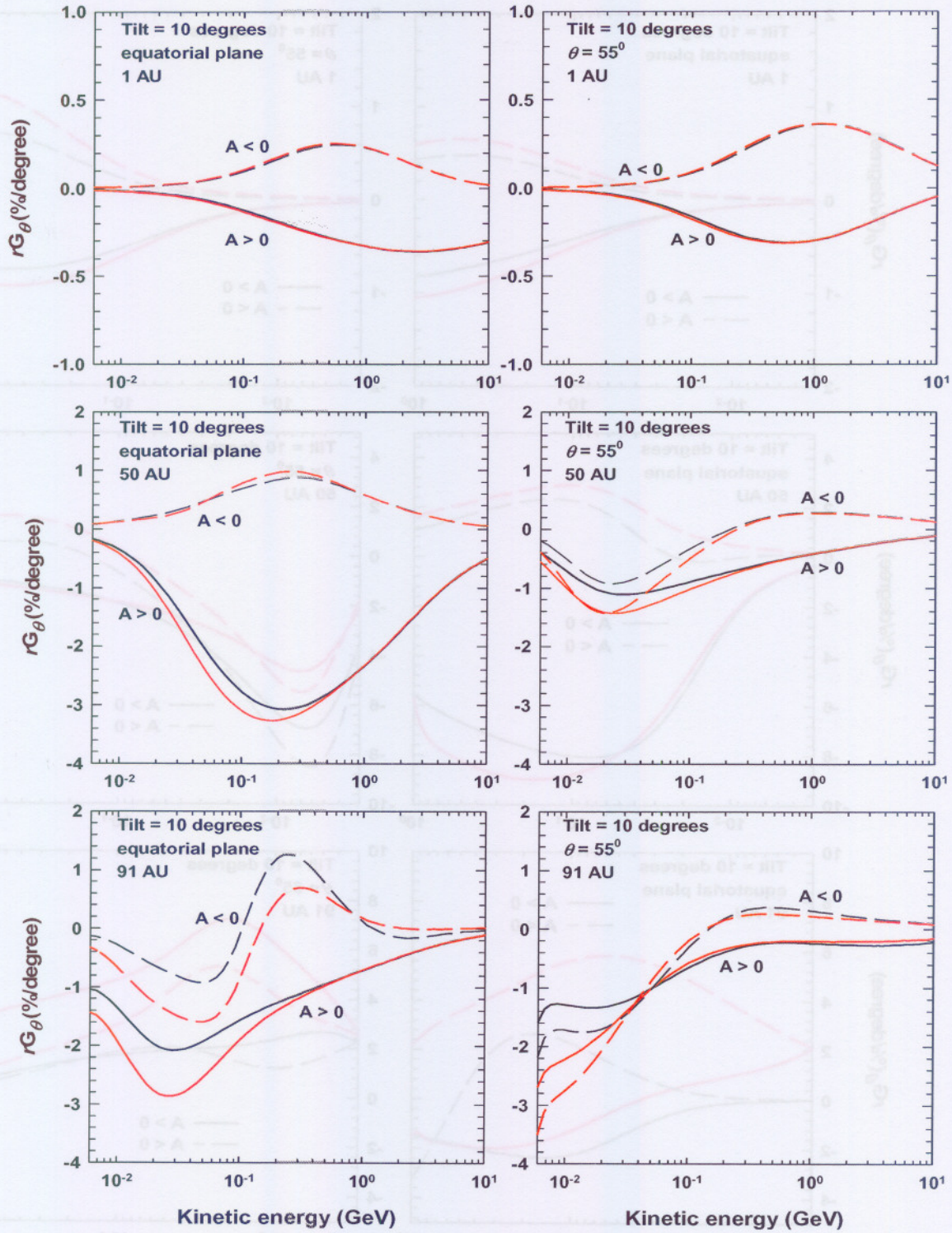

Figure 5.6. Left panels: Computed rG_θ for GCR protons, in %/degree, as a function of kinetic energy for both polarity cycles in the equatorial plane at radial distances 1, 50 and 91 AU, respectively, and for solar minimum conditions. Right panels: Similar but at θ = 55°. Black lines are without a latitude dependence and red lines are with a latitude dependence of both s and the injection efficiency. The TS is at 90 AU.

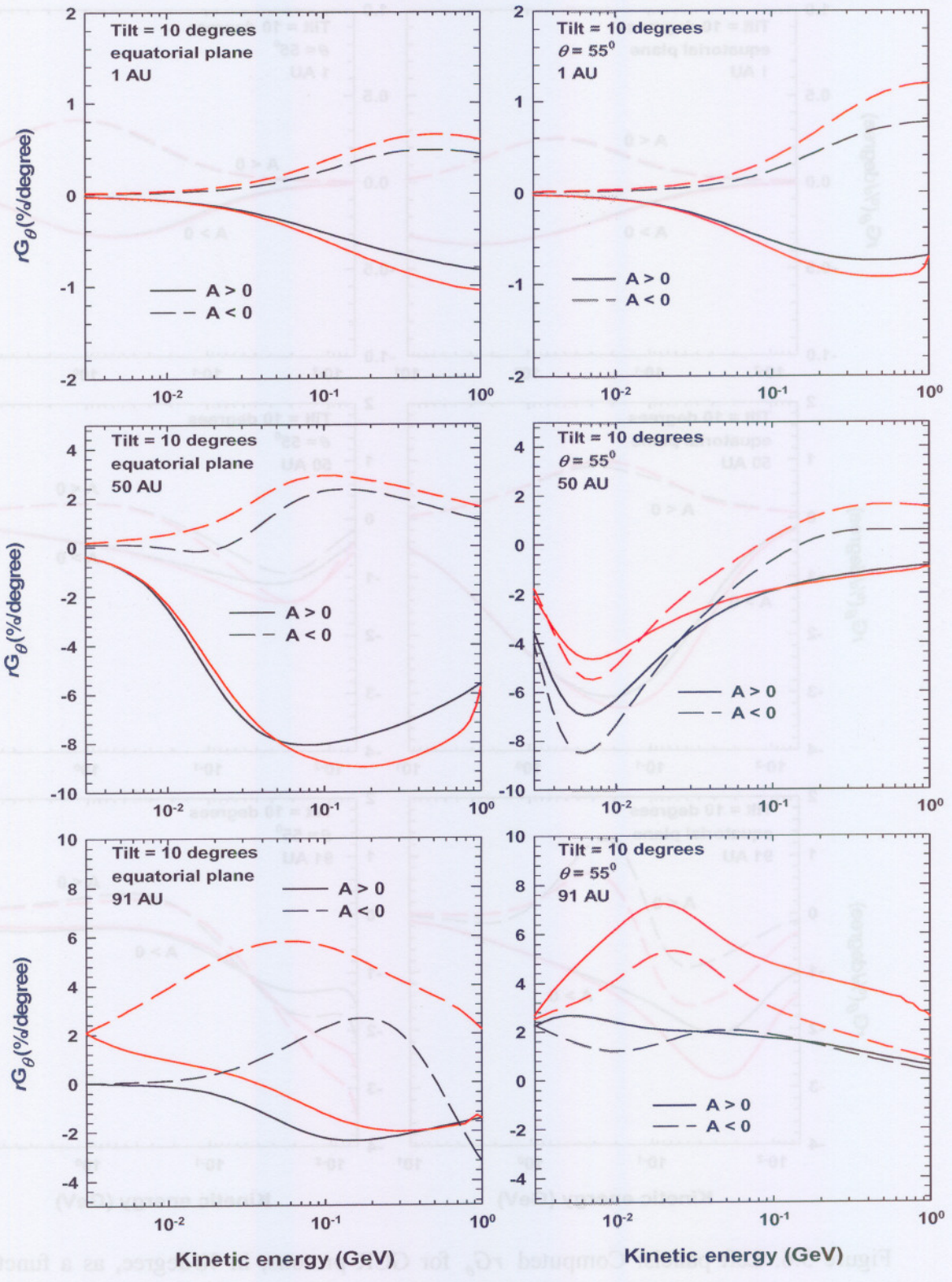

Figure 5.7. Left panels: Similar to Figure 5.6 but for ACR protons. Right panels: Similar but at $\theta = 55°$.

Figure 5.7 is similar to Figure 5.6 but for ACR protons. The red lines indicate the solutions with the latitude dependence of both s and the injection efficiency. The systematic behaviour up-stream of the TS, as in Figure 5.6, is also evident in this figure. Interesting is that at 91 AU the polar gradient is now significantly large and that it is positive at all energies at $\theta = 55°$ for both polarity cycles in contrast to GCR protons. The effect of the latitude dependence of both s and the injection efficiency on the polar gradients is clearly more pronounced at 91 AU; the polar gradient beyond the TS is qualitatively and quantitatively changed in both cycles. Its maximum is shifted to higher energies in the A > 0 cycle and to lower energies in the A < 0 cycle at all radial distances. It is increased by a factor of more than ~ 2 between 5 and 50 MeV at 91 AU and the largest increases are in the A < 0 cycle in the equatorial plane, but in the A > 0 cycle at $\theta = 55°$.

5.3 Summary and conclusions

In this Chapter the local radial and latitudinal (polar) gradients were studied for GCR and ACR protons in the heliosphere, computed using the numerical model described in Chapter 3. The effects of the latitudinal dependence of the compression ratio of the TS and injection efficiency of the ACR source, developed in Chapter 4, as well as adiabatic acceleration of particles in the heliosheath ($V \propto 1/r^3$) on this gradient were also studied. It was found that the radial gradient of GCR protons varies with polarity in the equatorial plane and increases with decreasing radial distance in the inner heliosphere in the A < 0 cycle. This radial gradient was found to be larger in the A < 0 cycle than in the A > 0 cycle at radial distances of $r <$ ~ 40 AU. Whereas at $\theta = 55°$ the trend as a function of radial distance in both polarity cycles was found to be similar. Similar results were found for ACR protons, but at different energies.

When crossing the TS into the heliosheath, the radial gradient was found to change abruptly and this effect was found to vary significantly with particle energy for GCRs, while for ACRs it was found to decrease at all energies of interest in the heliosheath.

The latitude dependence of s and injection efficiency was found to increase and to shift the maximum radial gradient to lower energies for GCRs but to higher energies for ACRs inside the TS. When the latitude dependence of these two parameters was combined with $V \propto 1/r^3$ in the heliosheath, causing additional acceleration of particles, it was found that the effects of this adiabatic acceleration in the heliosheath on the radial gradient for ACR

protons were only prominent at 16 MeV, whereas at 0.08 and 0.2 GeV they were found to have been cancelled by increasing modulation effects such as drifts and diffusion.

Inside (up-stream of) the TS in the equatorial plane, the polar gradient for both GCRs and ACRs was found to display variations in a systematic way with the 11-year solar activity cycle. Beyond the TS at 91 AU for GCRs, it was found to have negative values at lower energies and nearly zero at higher energies in both cycles. This behaviour was found to be different for ACRs at 91 AU.

The latitude dependence of s and injection efficiency was found to increase and to shift the maximum polar gradient for ACRs to higher energies in the $A > 0$ and to lower energies in the $A < 0$ cycle, while for GCRs this effect was found not to vary with polarity cycle.

In the next Chapter, the gradients discussed here will be used to calculate and to further investigate to what extent they affect the cosmic ray anisotropies in the heliosphere.

Chapter 6

Cosmic ray anisotropies in the heliosphere

6.1 Introduction

In the previous chapters CR modulation was studied in the heliosphere using a 2D time dependent shock acceleration model (discussed in Chapter 3) with emphasis on the effects of the TS on the modulated spectra and intensity gradients of GCR and ACR protons when a latitude dependence of the compression ratio s and injection efficiency, developed in Chapter 4, is assumed. The purpose of this chapter is to investigate the energy and spatial dependence of various physical components (due to convection, diffusion etc.) of the anisotropy vector and to illustrate how they change across the TS. Effects of the latitude dependence of s and the injection efficiency on the two components of the anisotropy vector are also studied.

The observation of the directional distribution of energetic and CR particles has been done with the Voyager spacecraft over a long period. Since 2002, when the first flux enhancements of charged particles associated with the approach of V1 to the TS were observed, these anisotropy measurements have become of special interest (McDonald et al., 2003; Krimigis et al., 2003). They play an important role in the understanding of the magnetic field and shock structure and the basics of the modulation of CR at and beyond the TS. These observations serve as motivation for this modeling study but without fine-tuning the parameters to fit observations.

6.2 Anisotropies

The diffusive streaming of particles with momentum p in the solar wind frame of reference is given by

$$\boldsymbol{S}_p = -\mathbf{K}.\nabla U_p, \tag{6.1}$$

with $\mathbf{K}$ and U_p the diffusion tensor discussed in Chapter 3 and the differential cosmic-ray number density $U_p = 4\pi p^2 f$, respectively. Thus in the solar wind frame the cosmic rays are scattered without change of particle speed as they interact with the quasi-static magnetic

irregularities moving with the solar wind (Gleeson and Webb, 1978). However, the scattering centers in the solar wind move with velocity **V** relative to a stationary observer. Thus, the stationary observer records a streaming

$$\boldsymbol{S}_p = 4\pi p^2 \left(C\mathbf{V}f - \mathbf{K}.\nabla f \right), \tag{6.2}$$

where

$$C = -\frac{1}{3}\frac{\partial \ln f}{\partial \ln p}, \tag{6.3}$$

is the Compton-Getting factor (Gleeson and Axford, 1968).

In heliocentric spherical coordinates, neglecting the azimuthal component, Equation (6.2) becomes

$$\boldsymbol{S}_p = 4\pi p^2 \left(CVf\boldsymbol{e}_r - K_{rr}\frac{\partial f}{\partial r}\boldsymbol{e}_r + \frac{K_A \sin\psi}{r}\frac{\partial f}{\partial \theta}\boldsymbol{e}_r - K_A \sin\psi \frac{\partial f}{\partial r}\boldsymbol{e}_\theta - \frac{K_{\theta\theta}}{r}\frac{\partial f}{\partial \theta}\boldsymbol{e}_\theta \right). \tag{6.4}$$

The anisotropy vector in spherical coordinates in terms of $\boldsymbol{S}_p$ is given by

$$\boldsymbol{\xi} = \frac{3\boldsymbol{S}_p}{v 4\pi p^2 f}$$

$$= \frac{3}{v}\left(CV\boldsymbol{e}_r - K_{rr}\frac{\partial f}{f\partial r}\boldsymbol{e}_r + \frac{K_A \sin\psi}{rf}\frac{\partial f}{\partial \theta}\boldsymbol{e}_r - \frac{K_A \sin\psi}{f}\frac{\partial f}{\partial r}\boldsymbol{e}_\theta - \frac{K_{\theta\theta}}{rf}\frac{\partial f}{\partial \theta}\boldsymbol{e}_\theta \right)$$

$$= \frac{3}{v}\left(CV\boldsymbol{e}_r - K_{rr}G_r\boldsymbol{e}_r + K_A \sin\psi G_\theta \boldsymbol{e}_r - K_A \sin\psi G_r \boldsymbol{e}_\theta - K_{\theta\theta}G_\theta \boldsymbol{e}_\theta \right), \tag{6.5}$$

where v is the particle speed, with G_r and G_θ the cosmic ray gradients as discussed in Chapter 5. Equation (6.5) can be separated into the radial and the latitudinal anisotropy vectors given by

$$\boldsymbol{\xi} = \xi_r \boldsymbol{e}_r + \xi_\theta \boldsymbol{e}_\theta . \tag{6.6}$$

These components are studied individually below, using the 2D shock acceleration model discussed in Chapter 3.

6.3 Radial component of the anisotropy vector

The radial component of the anisotropy vector in Equation (6.6), according to Equation (6.5) is given by

$$\xi_r = \frac{3}{v}(CV - K_{rr}G_r + K_A \sin\psi G_\theta) . \tag{6.7}$$

Terms on the right hand of Equation (6.7) describe the contributions caused by the convection (Compton-Getting) anisotropy, diffusion anisotropy and drift anisotropy, respectively. The drift anisotropy changes sign with the HMF polarity cycle, causing a 22-year effect in the radial anisotropy (see e.g., Lemmer, 1982; Potgieter, 1984; Potgieter and Moraal, 1985; van Staden and Potgieter, 1991). Apart from the three coefficients ($K_{||}$, $K_{\perp r}$ and K_A), the last two terms depend on the sign and magnitude of the radial and latitudinal gradients, which are strongly dependent on energy and position in the heliosphere as was illustrated in the previous chapter.

6.3.1 Energy dependence of the radial anisotropy

Figure 6.1 shows the energy dependence of the radial anisotropy ξ_r (solid lines) for GCR protons, in %, in the equatorial plane for both polarity cycles and for solar minimum conditions (α = 10°) at radial distances of 1, 50 and 91 AU. Also shown, in %, and according to Equation (6.7), is the Compton-Getting anisotropy $3CV/v$ (dash-dot-dash lines), diffusion anisotropy $3K_{rr}G_r/v$ (long dashed lines) and drift anisotropy $3K_A \sin\psi\, G_\theta/v$ (dotted lines) in comparison to the energy dependence of ξ_r. The TS is at 90 AU and the HP, where the LIS is specified, is at 120 AU. The TS compression ratio s = 3.2 at all latitudes.

For a typical power law intensity spectrum of the form $P^{-2.5}$ ($f \propto P^{-4.5}$), the Compton-Getting factor $C \approx 1.5$, so that in a solar wind with V = 400 km s^{-1}, and for relativistic particles ($v \approx c = 3.\ 10^8$ m.s^{-1}), the Compton-Getting anisotropy is ~ 0.6% (Moraal et al., 2005), as shown in Figure 6.1. The Compton-Getting anisotropy increases from either a relatively small negative value or from zero at low energies to ~ 0.6% at relativistic proton energies in the equatorial plane at 1 and 50 AU. At 91 AU, as an example beyond the TS, it decreases by a factor of ~ s to become ~ 0.2% at relativistic energies as anticipated. This is obviously because V is compressed across the TS. This serves as an example that the computations are reproducing the basic features of the theory as given above.

It is evident from Figure 6.1 that ξ_r at 1 AU in the A > 0 cycle at energies < ~ 0.8 GeV is dominated by the Compton-Getting anisotropy. At energies < ~ 40 MeV ξ_r becomes negligibly small. At energies above ~ 0.8 GeV diffusion and especially drifts have an increasingly significant effect on ξ_r and cancel a large fraction of the Compton-Getting

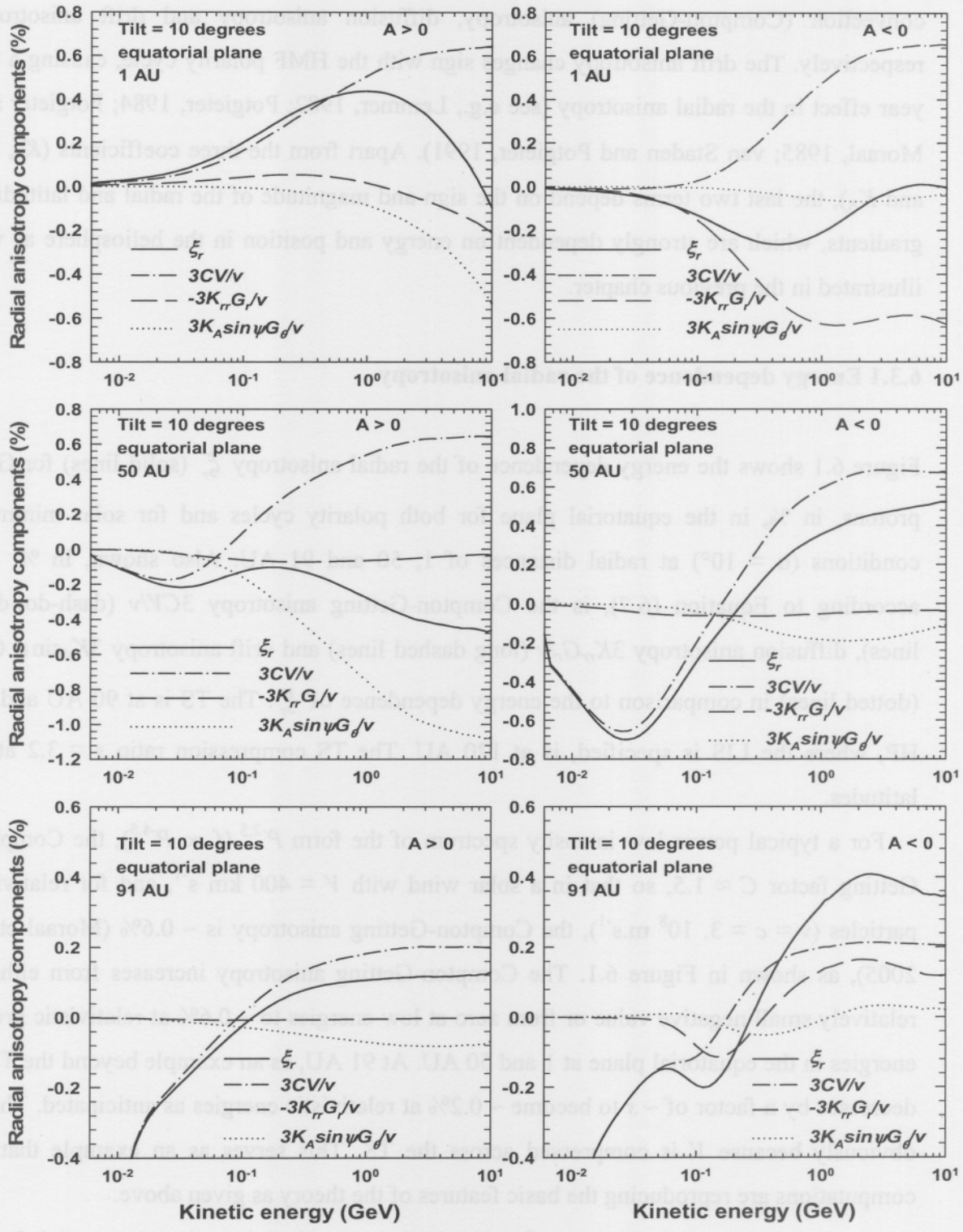

Figure 6.1. Shown is ξ_r (solid lines) for GCR protons, in %, as a function of kinetic energy for solar minimum conditions ($\alpha = 10°$), for both polarity cycles in the equatorial plane at 1, 50 and 91 AU respectively. Shown also, in %, is the Compton-Getting anisotropy $3CV/v$ (dash-dot-dash lines), diffusion anisotropy $3K_{rr}G_r/v$ (long dashed lines) and drift anisotropy $3K_A \sin\psi\, G_\theta/v$ (dotted lines). The TS is at 90 AU and the HP, where the LIS is specified, is at 120 AU. The TS compression ratio $s = 3.2$ at all latitudes.

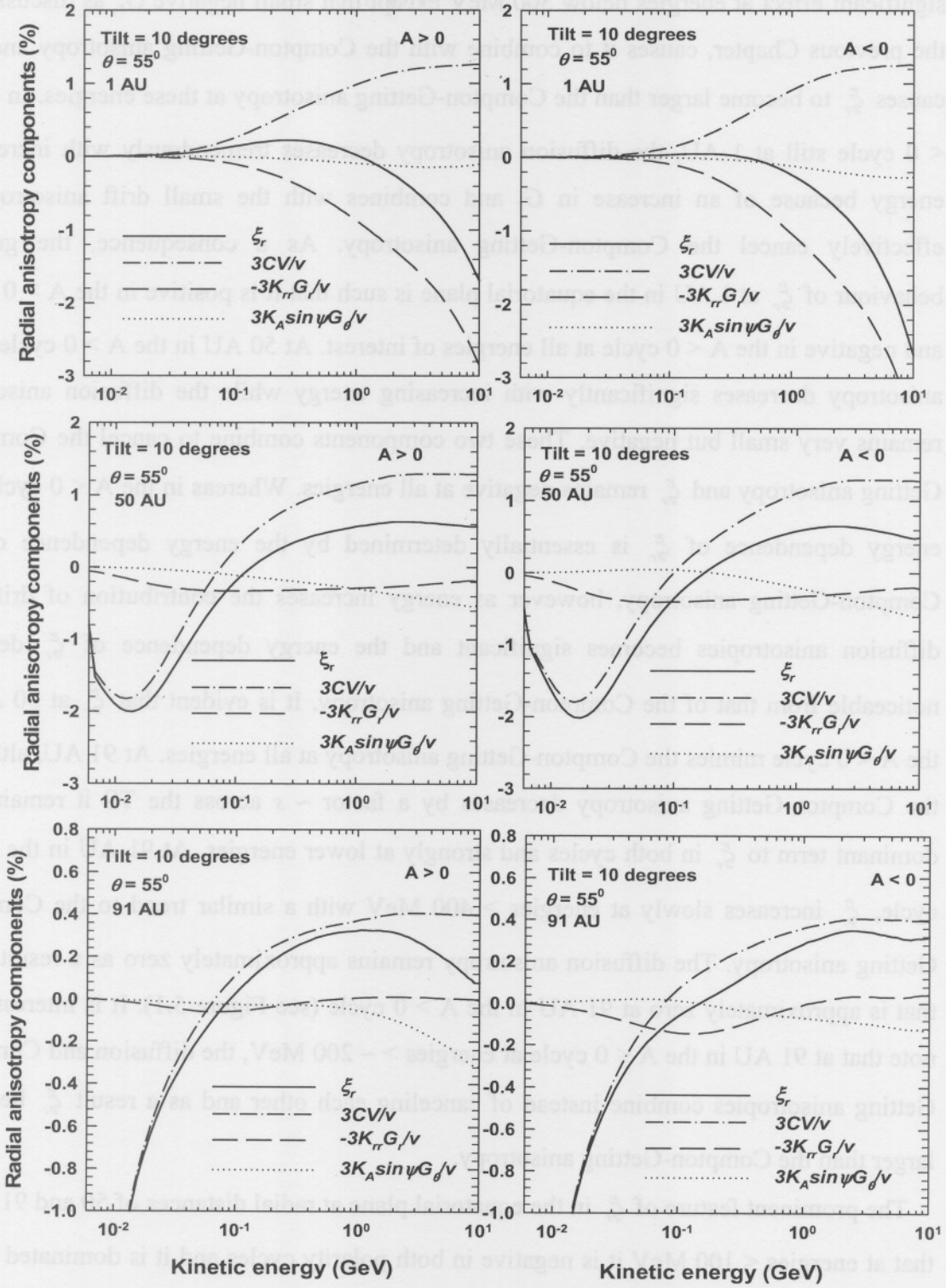

Figure 6.2. Similar to Figure 6.1, but at $\theta = 55°$.

anisotropy so that ξ_r decreases considerably. The diffusion anisotropy does not have a significant effect at energies below 500 MeV except that small negative G_r, as discussed in the previous Chapter, causes it to combine with the Compton-Getting anisotropy and this causes ξ_r to become larger than the Compton-Getting anisotropy at these energies. In the A < 0 cycle still at 1 AU, the diffusion anisotropy decreases tremendously with increasing energy because of an increase in G_r and combines with the small drift anisotropy to effectively cancel the Compton-Getting anisotropy. As a consequence, the general behaviour of ξ_r at 1 AU in the equatorial plane is such that it is positive in the A > 0 cycle and negative in the A < 0 cycle at all energies of interest. At 50 AU in the A > 0 cycle, drift anisotropy decreases significantly with increasing energy while the diffusion anisotropy remains very small but negative. These two components combine to cancel the Compton-Getting anisotropy and ξ_r remains negative at all energies. Whereas in the A < 0 cycle, the energy dependence of ξ_r is essentially determined by the energy dependence of the Compton-Getting anisotropy, however as energy increases the contribution of drift and diffusion anisotropies becomes significant and the energy dependence of ξ_r deviates noticeable from that of the Compton-Getting anisotropy. It is evident that ξ_r at 50 AU in the A < 0 cycle mimics the Compton-Getting anisotropy at all energies. At 91 AU, although the Compton-Getting anisotropy decreases by a factor $\sim s$ across the TS it remains the dominant term to ξ_r in both cycles and strongly at lower energies. At 91 AU in the A > 0 cycle, ξ_r increases slowly at energies > 400 MeV with a similar trend to the Compton-Getting anisotropy. The diffusion anisotropy remains approximately zero as a result of G_r that is approximately zero at 91 AU in the A > 0 cycle (see Figure 5.1). It is interesting to note that at 91 AU in the A < 0 cycle at energies > ~ 200 MeV, the diffusion and Compton-Getting anisotropies combine instead of canceling each other and as a result ξ_r becomes larger than the Compton-Getting anisotropy.

The prominent feature of ξ_r in the equatorial plane at radial distances of 50 and 91 AU is that at energies < 100 MeV it is negative in both polarity cycles and it is dominated by the Compton-Getting anisotropy. This can be understood by considering the spectra of GCRs illustrated in Chapter 4. At 1 AU the intensities $J \propto E$ at lower energies and this is known as the adiabatic limit of modulation. The Compton-Getting effect (Equation 6.3) becomes approximately zero at lower energies due to this limit. However, at radial distances of 50

and 91 AU the spectral shape deviate and become steeper than the adiabatic limit at lower energies. This causes the Compton-Getting effect at 50 and 91 AU to be negative, and hence the corresponding Compton-getting anisotropy becomes large negative. This has a pronounced effect on ξ_r at these energies in a sense that it is always negative.

Figure 6.2 is similar to Figure 6.1, but ξ_r is plotted at $\theta = 55°$. Evident from Figure 6.2 is that ξ_r is overall significantly larger than in the equatorial plane. Conspicuous is that because of the very small G_θ at this latitude, the drift anisotropy is less than 0.01% in the A > 0 cycle and less than 0.03% in the A < 0 cycle at 1 AU and at all energies. As a result ξ_r becomes a competition between the Compton-Getting and diffusion anisotropies.

According to Figure 6.2, ξ_r decreases exceptionally at low and intermediate energies in both polarity cycles at 1 AU when compared to its value in the equatorial plane. At high energies it becomes large negative and this is due to the large diffusion anisotropy seen in this figure, and not the drifts anisotropy, usually the dominant effect at high energies. At radial distances of 50 and 91 AU the trend of ξ_r is similar, the energy dependence of ξ_r is determined by the energy dependence of the Compton-Getting anisotropy and it is negative at lower energies and becomes positive at high energies in both polarity cycles.

Figure 6.3 is similar to Figure 6.1 but for ACR protons. As for GCR at 1 AU in the A > 0 cycle, the energy dependence of ξ_r is determined by the energy dependence of the Compton-Getting anisotropy. Evident at energies < 20 MeV at 1 AU in the A > 0 cycle is that ξ_r is changing gradually but to increase significantly above this energy to become > 1% at energies > 200 MeV. In the A < 0 cycle at 1 AU and at energies < 100 MeV, ξ_r is dominated by the diffusion anisotropy, but at energies higher than this the Compton-Getting anisotropy is significantly increased such that ξ_r cannot be determined by only one term. The global behaviour of ξ_r for ACRs at 1 AU in the equatorial plane is similar to that of GCRs in a sense that it is positive in the A > 0 cycle and negative in the A < 0 cycle. At 50 AU the qualitative behaviour of ξ_r for ACR is similar to GCR protons but quantitative differences occur.

As expected significant differences between the two species occur at 91 AU. For ACR at 91 AU the intensity is still very close to $J \propto E^{-1.18}$ which is the energy dependence at the TS, hence the Compton-Getting anisotropy becomes large positive at energies before the spectral cut-off. What is evident in Figure 6.3 is that at this position ξ_r is positive at all

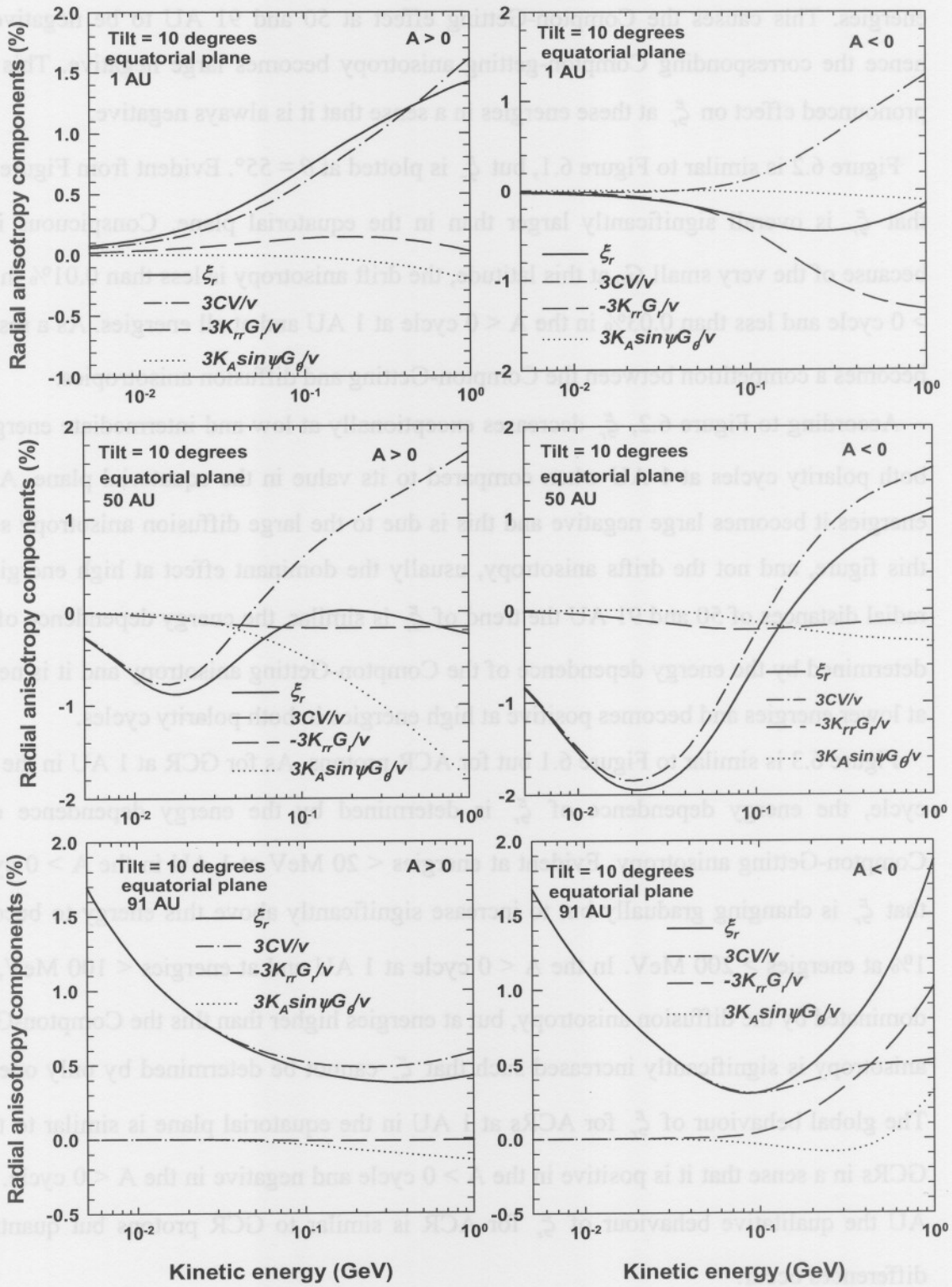

Figure 6.3. The computed radial anisotropy for ACR protons, in %, as a function of kinetic energy for solar minimum conditions ($\alpha = 10°$) and for both polarity cycles in the equatorial plane at radial distances 1, 50 and 91 AU respectively. The TS is at 90 AU. The TS compression ratio $s = 3.2$ at all latitudes.

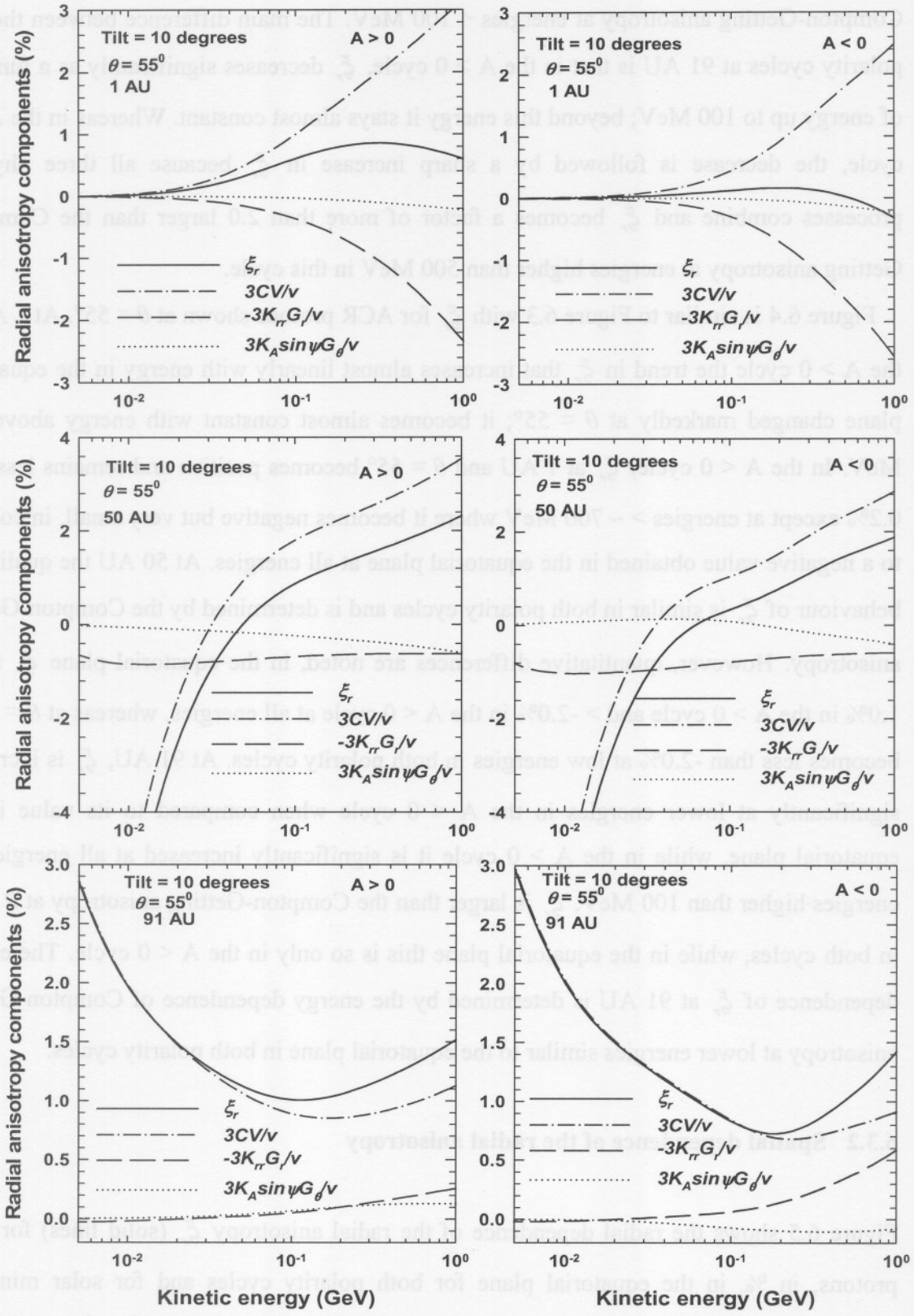

Figure 6.4. Same as Figure 6.3, but at $\theta = 55°$.

energies in both polarity cycle, and it is determined by the energy dependence of the Compton-Getting anisotropy at energies < 100 MeV. The main difference between the two polarity cycles at 91 AU is that in the A > 0 cycle, ξ_r decreases significantly as a function of energy up to 100 MeV; beyond this energy it stays almost constant. Whereas in the A < 0 cycle, the decrease is followed by a sharp increase in ξ_r because all three physical processes combine and ξ_r becomes a factor of more than 2.0 larger than the Compton-Getting anisotropy at energies higher than 500 MeV in this cycle.

Figure 6.4 is similar to Figure 6.3 with ξ_r for ACR protons shown at $\theta = 55°$. At 1 AU in the A > 0 cycle the trend in ξ_r that increases almost linearly with energy in the equatorial plane changed markedly at $\theta = 55°$; it becomes almost constant with energy above 100 MeV. In the A < 0 cycle, ξ_r at 1 AU and $\theta = 55°$ becomes positive and remains less than 0.2% except at energies > ~ 700 MeV where it becomes negative but very small, in contrast to a negative value obtained in the equatorial plane at all energies. At 50 AU the qualitative behaviour of ξ_r is similar in both polarity cycles and is determined by the Compton-Getting anisotropy. However, quantitative differences are noted, in the equatorial plane ξ_r is > -1.0% in the A > 0 cycle and > -2.0% in the A < 0 cycle at all energies, whereas at $\theta = 55°$ it becomes less than -2.0% at low energies in both polarity cycles. At 91 AU, ξ_r is increased significantly at lower energies in the A < 0 cycle when compared to its value in the equatorial plane, while in the A > 0 cycle it is significantly increased at all energies. At energies higher than 100 MeV, ξ_r is larger than the Compton-Getting anisotropy at $\theta = 55°$ in both cycles, while in the equatorial plane this is so only in the A < 0 cycle. The energy dependence of ξ_r at 91 AU is determined by the energy dependence of Compton-Getting anisotropy at lower energies similar to the equatorial plane in both polarity cycles.

6.3.2 Spatial dependence of the radial anisotropy

Figure 6.5 shows the radial dependence of the radial anisotropy ξ_r (solid lines) for GCR protons, in %, in the equatorial plane for both polarity cycles and for solar minimum conditions ($\alpha = 10°$) at energies of 0.2, 0.5 and 1.0 GeV respectively. Also shown, in %, is the Compton-Getting anisotropy $3CV/v$ (dash-dot-dash lines), diffusion anisotropy $3K_{rr}G_r/v$ (long dashed lines) and drift anisotropy $3K_A \sin\psi\, G_\theta/v$ (dotted lines) in comparison with ξ_r.

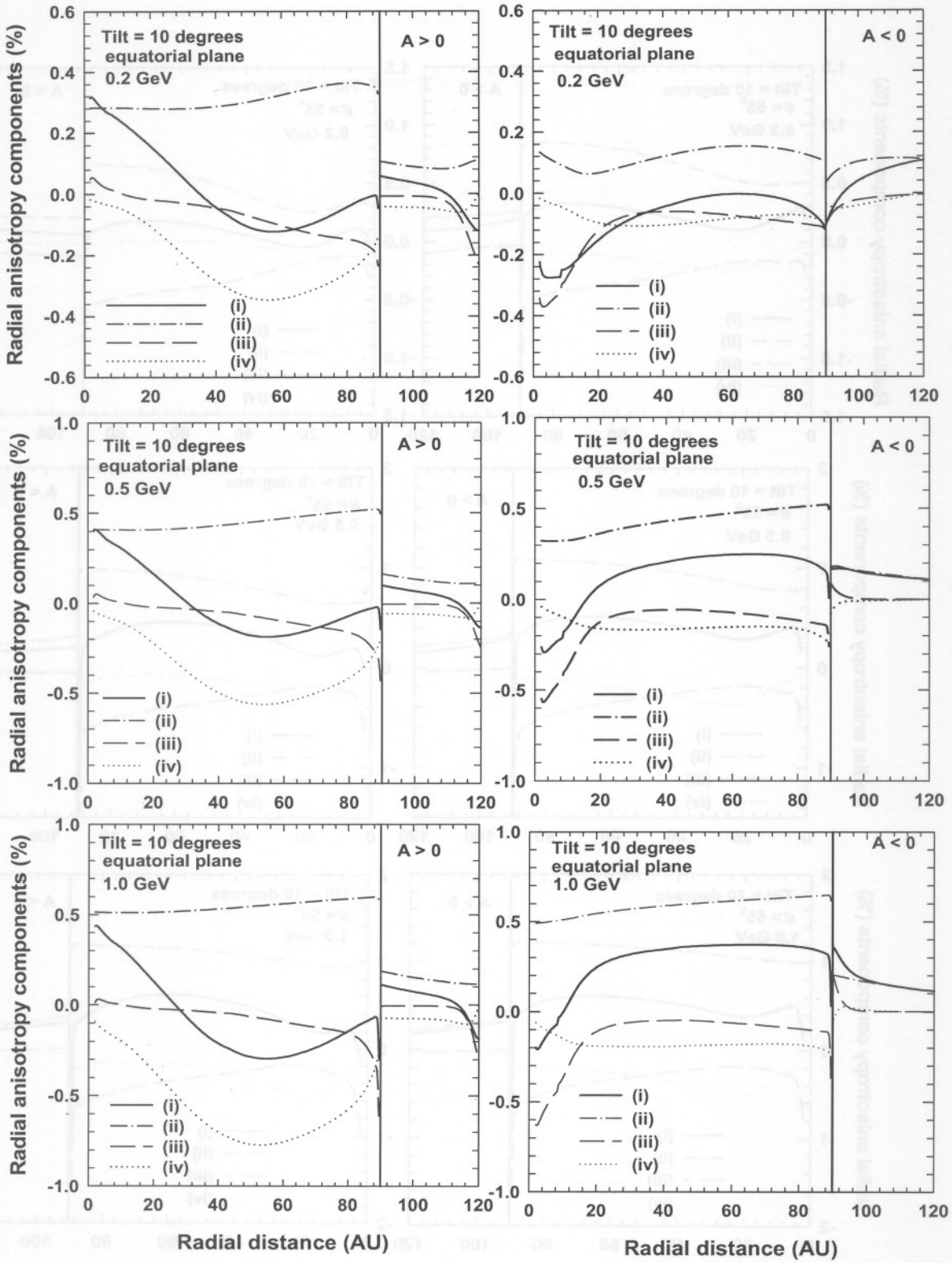

Figure 6.5. Shown is ξ_r (solid line marked by (i)) for GCR protons, in %, as a function of radial distance for solar minimum conditions ($\alpha = 10°$) and for both polarity cycles in the equatorial plane at energies of 0.2, 0.5 and 1.0 GeV, respectively. Shown also, in %, is the Compton-Getting anisotropy $3CV/v$ (dash-dot-dash line (ii)), diffusion anisotropy $3K_{rr}G_r/v$ (long dashed line (iii)) and drift anisotropy $3K_A \sin\psi\, G_\theta/v$ (dotted line (iv)). As before the TS is at 90 AU and the HP, where the LIS is specified, is at 120 AU. The TS compression ratio $s = 3.2$ at all latitudes.

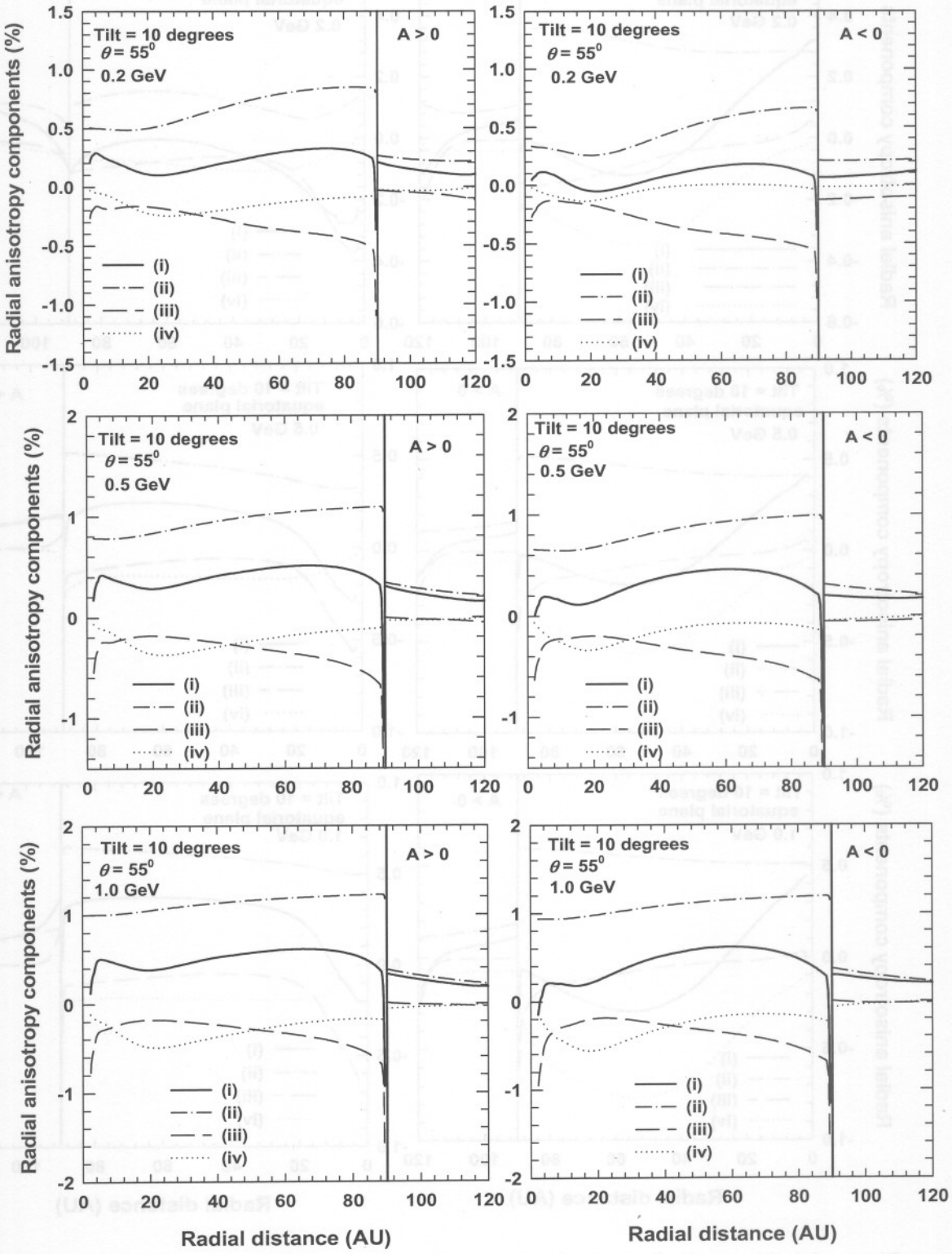

Figure 6.6. Similar to Figure 6.5, but at $\theta = 55°$.

The TS is at 90 AU and the HP, where the LIS is specified, is at 120 AU. The TS compression ratio $s = 3.2$ at all latitudes.

Figure 6.5 shows that the magnitude and direction of ξ_r strongly depends on the position in the heliosphere and the energy of particles. For example, during the A > 0 cycle, it decreases from a positive value in the inner heliosphere (up to 40 AU) to a negative value in the outer heliosphere, where it reaches minimum values of ~ -0.12% and ~ -0.3% at energies of 0.2 and 1.0 GeV, respectively, around 50 AU, to increase towards the TS. For the A < 0 cycle, ξ_r increases from a negative value in the inner regions of the heliosphere to a positive value in the outer heliosphere where it increases slowly until close to the shock.

At the TS, ξ_r changes abruptly to somewhat larger values beyond the shock especially in the A > 0 cycle, primarily because of the abrupt changes in the intensity gradients. Beyond the TS, in the heliosheath, ξ_r remains positive and less than 0.1% but with a slowly decreasing trend in the A > 0 cycle. This is so until close to the HP where it decreases significantly to negative values in the A > 0 cycle. In the A < 0 cycle the trend just in front of the TS depends on the particle energy, for example, at 0.2 GeV ξ_r increases abruptly in front of the TS but gradually when the HP is approached, while at 1.0 GeV it abruptly decreases but converges to ~ 0.1% when the HP is approached.

It is evident from Figure 6.5 that in the equatorial plane the model predicts for the inner heliosphere (< 40 AU) a large difference in the direction of ξ_r (positive and negative values) for the two polarity cycles, caused by drifts. The largest difference occurs at small radial distances from the Sun (close to Earth). These directions are easily explained, following intuitively the contribution made by drifts to ξ_r. However, in the outer heliosphere the direction of ξ_r becomes more complicated and cannot be easily explained using intuitive arguments.

The Compton-Getting anisotropy upwind of the TS is significantly larger than ξ_r, except close to the Earth. Beyond the TS it is no longer the case because of the drop in the solar wind speed at the TS, but it is still larger than ξ_r at 0.2 and 0.5 GeV in both polarity cycles.

Take note that for ξ_r a few AUs in front and beyond the shock (70-110 AU) in the equatorial plane, the downstream ξ_r in the A > 0 cycle is always larger than the upstream value at all energies of interest, but always lower than the downstream Compton-Getting anisotropy and it is directed outward at 0.5 and 1.0 GeV in the A < 0 cycle, in the direction

of solar wind flow, both upstream and downstream of the TS. Similar results were obtained by Jokipii and Giacalone (2004). In the A > 0 cycle, ξ_r in the equatorial plane is directed sunward in the upstream region and in the direction of flow in the downstream region.

Figure 6.6 is similar to Figure 6.5 but at θ = 55°. Evidently, ξ_r remains positive throughout the heliosphere at all energies of interest in both polarity cycles but becomes small negative at 0.2 GeV in the A < 0 cycle only between radial distances of ~15 and ~30 AU, and also at 1.0 GeV very close to the Sun. The large difference in ξ_r between the two polarity cycles obtained for the equatorial regions has been considerably reduced at θ = 55°. This is due to smaller latitudinal gradients in this region which reduces the effects of the drift anisotropy, hence ξ_r in this region at both polarity cycles and energies behaves qualitatively similar. This similar behavior for the two cycles is further caused by the enhancement of V by a factor of 2.0 towards the polar regions which increases the Compton-Getting anisotropy and causes ξ_r to be determined by competition between only the Compton-Getting anisotropy and the diffusion anisotropy especially in the outer heliosphere, with drifts contributing implicitly through G_r. ξ_r in this region can be easily scaled as a constant multiplied by the Compton-Getting anisotropy. The main result is that at θ = 55° ξ_r for GCRs is directed in the direction of flow and it is large in the upstream region than in the downstream region in both polarity cycles.

At the TS, the abrupt change in ξ_r especially in the A > 0 cycle for the equatorial plane has been significantly reduced at θ = 55°. While in the heliosheath, ξ_r decreases slowly with distance and becomes flat when the HP is approached in both cycles.

Figure 6.7 is similar to Figure 6.5 but for ACR with ξ_r shown at energies of 0.016, 0.08 and 0.2 GeV, respectively. It is evident that at 0.016 GeV the drift anisotropy is negligible and ξ_r is only a competition of the Compton-Getting and diffusion anisotropy. At this energy the Compton-Getting anisotropy is very small at $r < \sim 20$ AU in both polarity cycles and it decreases with distance to reach a minimum value, after which it increases sharply from negative values at $r > \sim 80$ AU to even become positive very close to the TS and remains so in the heliosheath. The decrease of the Compton-Getting anisotropy in the inner heliosphere is stronger in the A < 0 cycle than in the A > 0 cycle. The trend of ξ_r is similar to the Compton-Getting anisotropy as for GCRs at lower energies, but as the shock is approached the diffusion anisotropy contributes effectively to ξ_r but its contribution is such

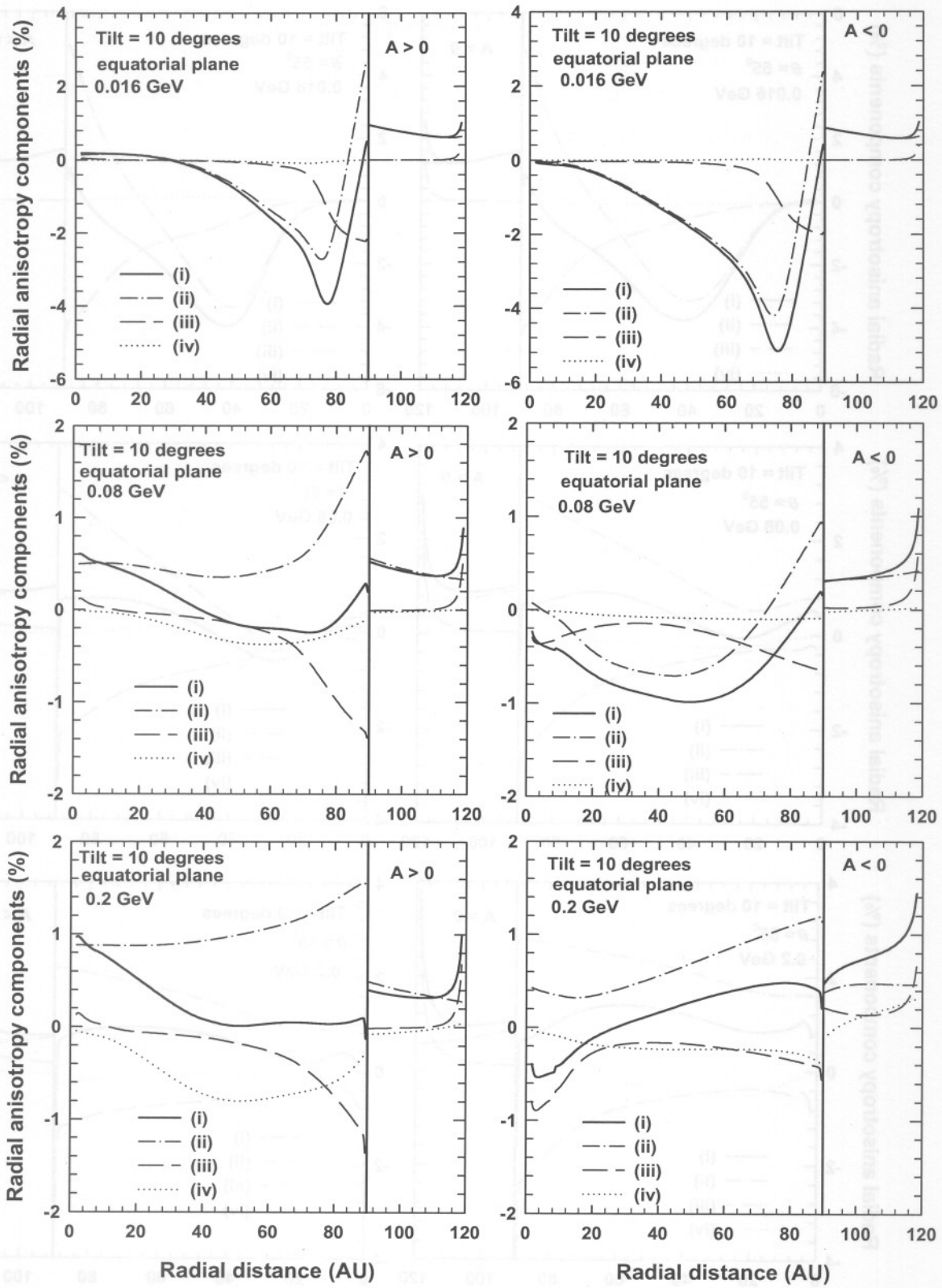

Figure 6.7. Similar to Figure 6.5 but for ACR protons and at energies of 0.016, 0.08 and 0.2 GeV respectively.

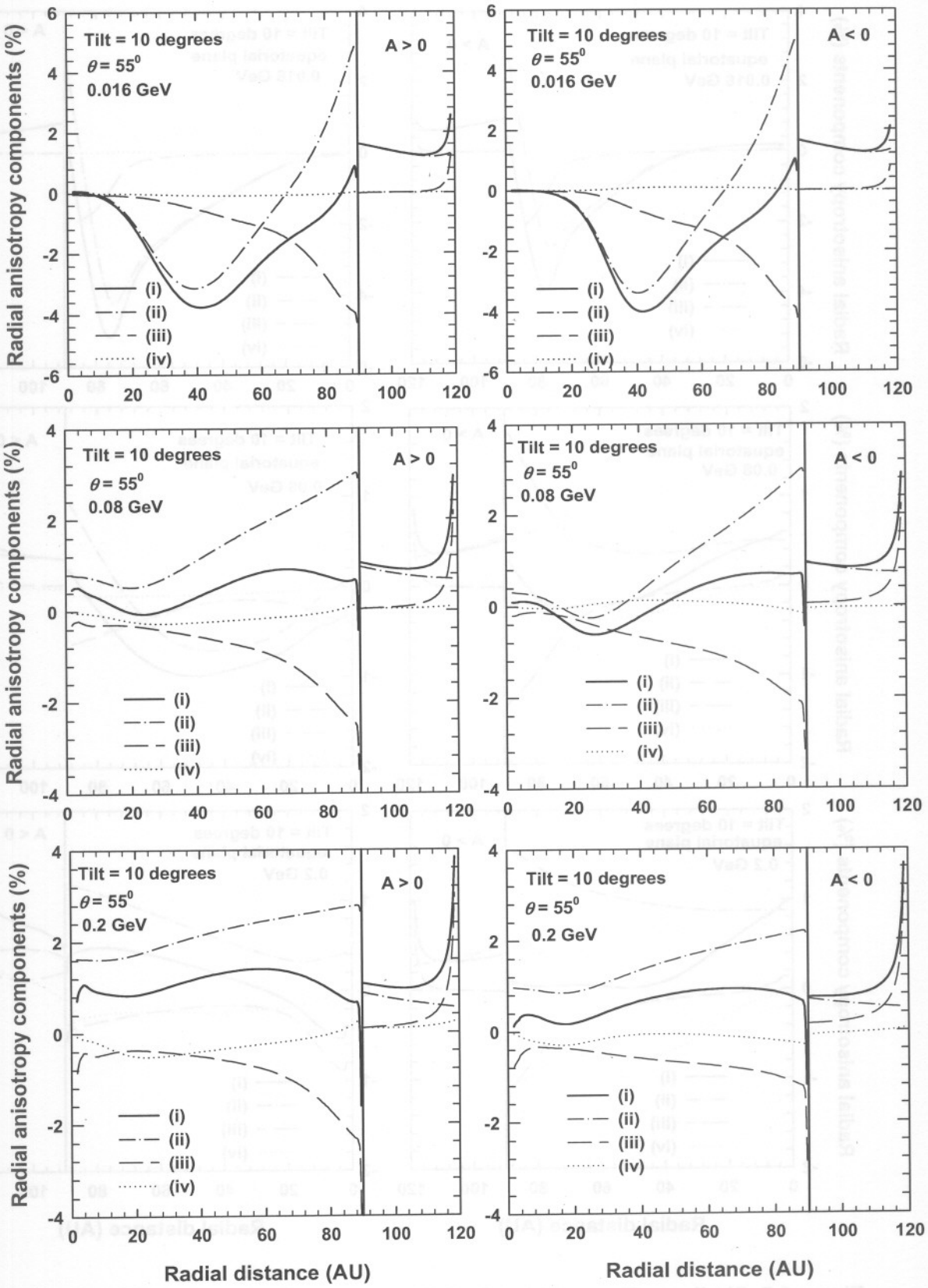

Figure 6.8. Similar to Figure 6.7 but at $\theta = 55°$.

that it combines with instead of canceling the Compton-Getting anisotropy and ξ_r decreases further. This is due to the negative Compton-Getting anisotropy at this energy and positions.

According to Figure 6.7, ξ_r at 0.08 GeV decreases up to a radial distance of ~ 50 AU for the A < 0 cycle and up to ~ 70 AU for the A > 0 cycle, from where it increases to larger values in response to the sharp increase in the Compton-Getting anisotropy. At this energy the drift anisotropy contributes but still insignificant in the A < 0 cycle, while the diffusion anisotropy becomes prominent close to the TS similar to 0.016 GeV. This leaves the Compton-Getting anisotropy to dominate ξ_r for the most part of the heliosphere. In the A > 0 cycle, ξ_r is directed away from the Sun for most part of the heliosphere, changing direction to be sunward in the outer heliosphere, changes again to be away from the Sun at radial distances of $r >$ ~ 80 AU and remains so in the heliosheath. While in the A < 0 cycle, ξ_r is directed in the sunward direction for most part of the heliosphere in the upstream region until close to the TS where the direction changes and it remains directed away from the Sun in the heliosheath. Notice the difference in ξ_r between the two drift cycles in the inner heliosphere at 0.08 GeV, it is positive in the A > 0 cycle and negative in the A < 0 cycle and it decreases in both cycles in contrast to the increasing and decreasing ξ_r in the A < 0 cycle and A > 0 cycle, respectively, for GCRs as illustrated in Figure 6.5. At 0.2 GeV, the qualitative picture begins to look similar to the 0.2 GeV GCRs shown in Figure 6.5. In the outer heliosphere ($r >$ 40 AU) ξ_r becomes almost constant with distance until when the TS is reached in the A > 0 cycle, while in the A < 0 cycle it increases with distance similar to GCRs at this energy. Quantitatively, important differences remain between the two species. ξ_r is directed away from the Sun in the A > 0 cycle at all radial distances in contrast to GCR at the same energy. However, in the A < 0 cycle the general behaviour of ξ_r is similar between the two species. When the HP is approached, ξ_r increases sharply in both cycles but this sharp increase decreases with energy.

Figure 6.8 is similar to Figure 6.7 but at $\theta = 55°$. It is evident that at 0.016 GeV the minimum reached in ξ_r is shifted from a radial distance of ~ 80 AU in the equatorial plane to ~ 40 AU at $\theta = 55°$ in both polarity cycle. ξ_r at this energy is directed in the direction of the Sun inside off the TS until very close to the TS where it changes to be away from the Sun just before the TS is crossed and it stays like that in the heliosheath. At 0.08 GeV, the diffusion anisotropy is more pronounced in the sense that the sharp increase of ξ_r when the

shock is approached in response to a sudden increase in the Compton-Getting anisotropy in the equatorial plane is absent at $\theta = 55°$, actually ξ_r decreases very slowly in the A > 0 cycle while it even flattens in the A < 0 cycle when the TS is approached. At this latitude the drift anisotropy is negligible especially at 0.016 and 0.08 GeV as anticipated. Close to the Sun, ξ_r at 0.08 GeV is directed away from the Sun in both drift cycles, but changes to be sunward in the A < 0 cycle beyond 10 AU and changes again to be away from the Sun throughout the heliosphere beyond 40 AU. While in the A > 0 it remains directed away from the Sun throughout the heliosphere.

At 0.2 GeV at $\theta = 55°$, ξ_r is directed away from the Sun in the direction of flow at all radial distances. This might be due to the increased solar wind speed which causes the Compton-Getting anisotropy to overwhelm the diffusion anisotropy. The drift anisotropy is still very small even at 0.2 GeV and this is obviously a consequence of small latitudinal gradients. When the TS is approached ξ_r in the A > 0 cycle decreases faster than in the A < 0 cycle.

When comparing ξ_r in front and beyond the shock as before it is found that the downstream ξ_r is greater than the upstream anisotropy at all energies of interest and for both polarity cycles. This led Jokipii and Giacalone (2004) to the conclusion that the radial anisotropy of particles accelerated at the TS, such as the ACRs, is not simply related to the speed of the background plasma.

6.4 Latitudinal component of the anisotropy vector

The latitudinal component of the anisotropy vector according to Equations (6.6) and Equation (6.5) is given by

$$\xi_\theta = -\frac{3}{v}(K_{\perp\theta} G_\theta + K_A \sin\psi G_r). \tag{6.8}$$

Terms on the right hand describe the anisotropy caused by the streaming of particles in the polar direction and the drift anisotropy, respectively. It follows that at low energies drifts become negligible ($K_A \to 0$) so that the latitudinal anisotropy is only determined by G_θ and $K_{\perp\theta}$. Since $K_{\perp\theta}$ increases significantly off the equatorial plane, the latitudinal anisotropy component may dominate the anisotropy vector off the equatorial plane especially at low energies. However, at high energies drifts dominate (K_A becomes large)

and the drift anisotropy term $3K_A \sin\psi G_r / v$ in Equation (6.8) has a significant contribution to ξ_θ. Also following from Equation (6.8) is that this drift anisotropy term changes sign with the HMF polarity cycles.

In this section the model is used to study terms in Equation (6.8), in particular to what extent each term determines ξ_θ and to further illustrate how ξ_θ for GCR and ACR protons behave as a function of energy at different radial distances in the heliosphere.

Figure 6.9 shows the energy dependence of ξ_θ (solid lines marked by (i)) for GCR protons given by Equation (6.8), in %, in the equatorial plane for both polarity cycles and for solar minimum conditions ($\alpha = 10°$) at radial distances of 1, 50 and 91 AU. Also shown, in %, is the drift anisotropy $3K_A \sin\psi G_r / v$ (dotted line (ii)) and the anisotropy due to streaming caused by diffusion of particles in the polar direction $3K_{\perp\theta} G_\theta / v$ (medium dashed line (iii)), in comparison to the total value of ξ_θ. As before, the TS is at 90 AU and the HP, where the LIS is specified, is at 120 AU. The TS compression ratio $s = 3.2$ at all latitudes.

It is evident from Figure 6.9 that ξ_θ is dominated by $3K_{\perp\theta} G_\theta / v$ at lower energies at 1 and 50 AU for both polarity cycles. However, at high energies drifts dominate as stated above and the drift anisotropy term $3K_A \sin\psi G_r / v$ has a significant effect on ξ_θ and can dominate even at 1 AU, especially in the A < 0 cycle. Beyond the TS (91 AU) at energies > ~ 100 MeV, the energy dependence of ξ_θ is determined by the energy dependence of the drift anisotropy $3K_A \sin\psi G_r / v$ especially in the A < 0 cycle.

Figure 6.9 shows that at 1 AU in the A > 0 cycle, the drift anisotropy is approximately zero at energies below 1.0 GeV and that the energy dependence of ξ_θ is determined by $3K_{\perp\theta} G_\theta / v$ at these energies. Above 1.0 GeV drifts have a significant influence and the energy dependence of ξ_θ begin to deviate significantly from that of $3K_{\perp\theta} G_\theta / v$ and it assumes a decreasing trend with increasing energy. In the A < 0 cycle and at 1 AU, the energy dependence of ξ_θ is dominated by the drift anisotropy at energies > 1.0 GeV. Drifts in this cycle increases ξ_θ contrary to the opposite drift cycle. ξ_θ in the A > 0 cycle increases slightly up to energies of ~ 30 MeV, above this energy it increases rapidly

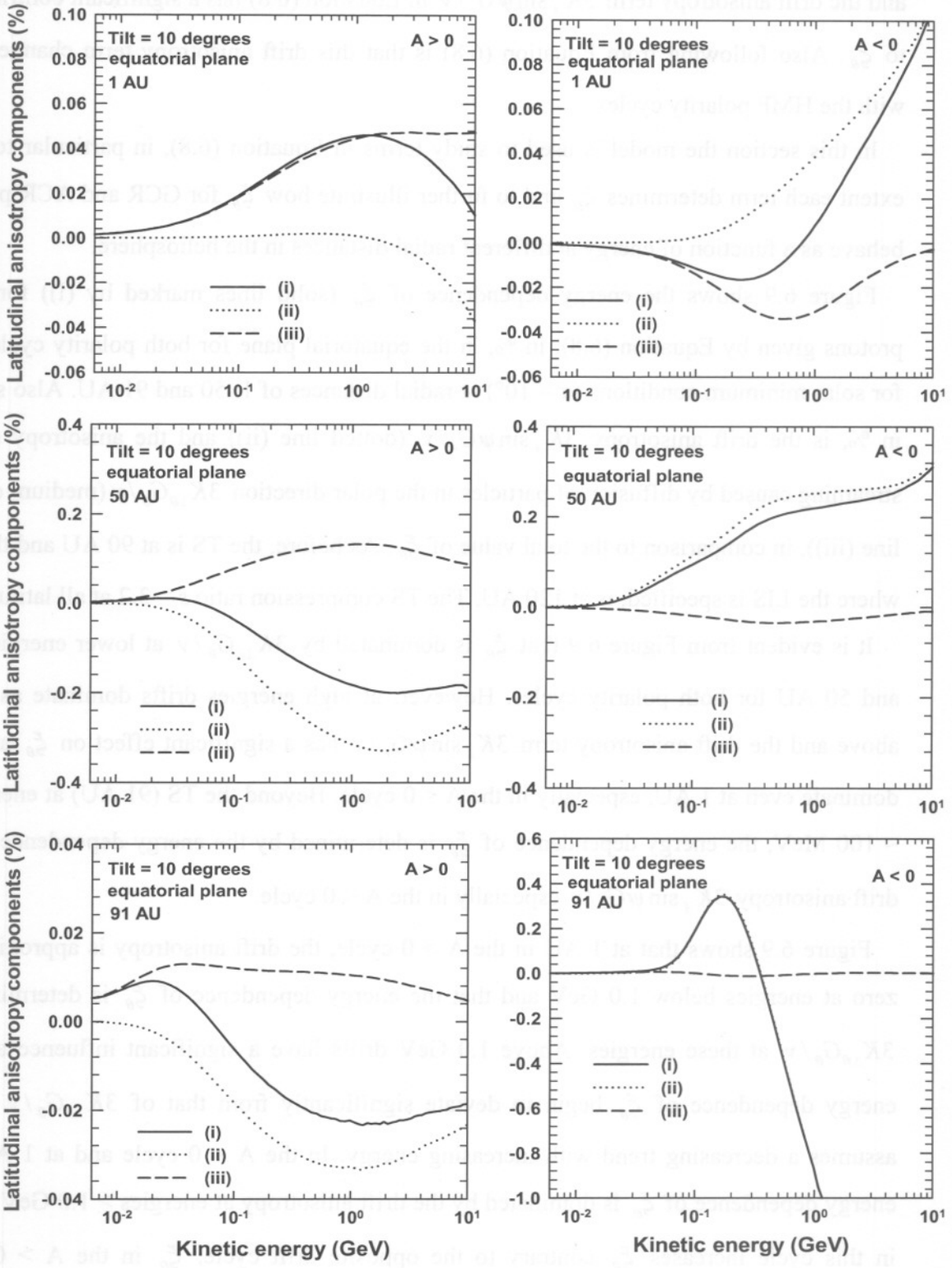

Figure 6.9. Shown is ξ_θ (solid line (i)) for GCR protons, in %, as a function of kinetic energy for solar minimum conditions ($\alpha = 10°$) and for both polarity cycles in the equatorial plane at radial distances of 1, 50 and 91 AU respectively. Shown also, in %, is $3K_A \sin\psi\, G_r/v$ (dotted line (ii)) and $3K_{\perp\theta}G_\theta / v$ (medium dashed line (iii)). The HP is at 120 AU and the TS at 90 AU. The TS compression ratio $s = 3.2$ at all latitudes.

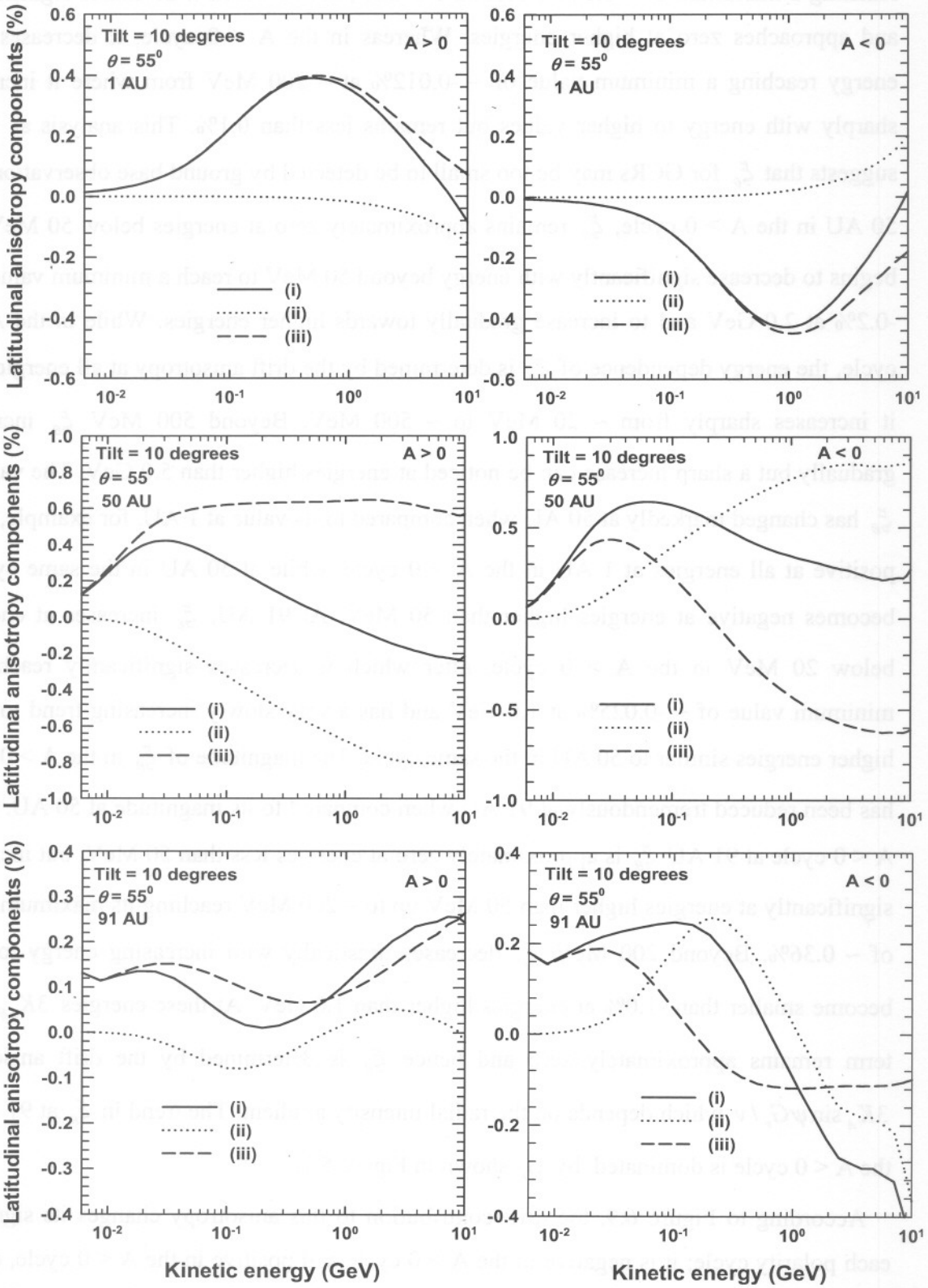

Figure 6.10. Similar to Figure 6.9 but at $\theta = 55°$.

reaching a maximum of ~ 0.044% around 1.0 GeV, above which it decreases significantly and approaches zero at higher energies. Whereas in the A < 0 cycle, it decreases with energy reaching a minimum value of ~ -0.012% at ~ 200 MeV from where it increases sharply with energy to higher values but remains less than 0.1%. This analysis at 1 AU suggests that ξ_θ for GCRs may be too small to be detected by ground base observations. At 50 AU in the A > 0 cycle, ξ_θ remains approximately zero at energies below 50 MeV and begins to decrease significantly with energy beyond 50 MeV to reach a minimum value of ~ -0.2% at 2.0 GeV and to increase gradually towards higher energies. While in the A < 0 cycle, the energy dependence of ξ_θ is determined by the drift anisotropy at all energies and it increases sharply from ~ 20 MeV to ~ 500 MeV. Beyond 500 MeV ξ_θ increases gradually but a sharp increase can be noticed at energies higher than 5.0 GeV. The value of ξ_θ has changed markedly at 50 AU when compared to its value at 1 AU, for example, ξ_θ is positive at all energies at 1 AU in the A > 0 cycle, while at 50 AU in the same cycle it becomes negative at energies higher than 50 MeV. At 91 AU, ξ_θ increases at energies below 20 MeV in the A > 0 cycle, after which it decreases significantly reaching a minimum value of ~ -0.025% at 1.0 GeV and has a very slowly increasing trend towards higher energies similar to 50 AU in the same cycle. The magnitude of ξ_θ in the A > 0 cycle has been reduced tremendously at 91 AU when compared to its magnitude at 50 AU. In the A < 0 cycle at 91 AU ξ_θ is approximately zero at energies less than 50 MeV, but increases significantly at energies higher than 50 MeV up to ~ 200 MeV reaching its maximum value of ~ 0.36%. Beyond 200 MeV ξ_θ decreases drastically with increasing energy to even become smaller than -1.0% at energies higher than 1.0 GeV. At these energies $3K_{\perp\theta}G_\theta / v$ term remains approximately zero and hence ξ_θ is determined by the drift anisotropy $3K_A \sin\psi G_r / v$ which depends on the radial intensity gradient. The trend in ξ_θ at 91 AU in the A < 0 cycle is dominated by G_r shown in Figure 5.1.

According to Figure 6.9, the drift contribution to this anisotropy changes its sign with each polarity cycle; it is negative in the A > 0 cycle and positive in the A < 0 cycle, except at 91 AU in the A < 0 cycle where it becomes positive at intermediate energies and negative at high energies. This is an attribute of G_r that has a mixture of both signs (negative and positive) in this polarity cycle.

The analysis of ξ_θ in the equatorial plane suggest that in drift modulation models the drift anisotropy $3K_A \sin\psi G_r / v$ has a significant role in determining ξ_θ, especially beyond 1 AU, particularly in the A < 0 cycle.

This global 2D analysis of ξ_θ for GCRs in the equatorial plane at the energies shown suggests that in the A > 0 cycle it is only easily observable in the middle heliosphere by spacecrafts. In the A < 0 cycle, it is easily detectable also in the heliosheath at energies above ~ 50 MeV. Close to the HP (not shown) ξ_θ increases because of a sharp increase in G_r in the A > 0 cycle and hence it should be detectable.

Figure 6.10 is similar to Figure 6.9 with ξ_θ now plotted at $\theta = 55°$. It is interesting to note that at 1 AU ξ_θ is dominated by $3K_{\perp\theta}G_\theta / v$ at all energies and for both polarity cycles. The term $3K_A \sin\psi G_r / v$ plays no significant role especially at energies below 1.0 GeV. At higher energy its effects are more noticeable as ξ_θ deviates with increasing energy from the value of $3K_{\perp\theta}G_\theta / v$ term. Furthermore, ξ_θ at 1 AU switches sign with the HMF and this is directed by the latitudinal gradient G_θ as required.

Figure 6.10 illustrates that in the energy range where ξ_θ is dominated by $3K_{\perp\theta}G_\theta / v$ the magnitude of ξ_θ increases remarkably, for example, at 1 AU in the A > 0 cycle ξ_θ reaches a maximum value of ~ 0.4% at an energy of ~ 600 MeV which is a factor of ~ 9.0 higher than its maximum value of ~ 0.044% reached in the equatorial plane. At 50 AU ξ_θ increases with energy reaching a maximum of 0.4% at energy of ~ 30 MeV and ~ 70 MeV in the A > 0 cycle and A < 0 cycle respectively. Beyond these energies it decreases to negative values in the A > 0 cycle beyond 1.0 GeV while in the A < 0 cycle it remains positive. At 91 AU in the A > 0 cycle, ξ_θ decreases with energy up to ~ 20 MeV similar to the equatorial plane but with different magnitude, from there it decreases up to ~ 100 MeV to increase again at energies beyond this reaching a value larger than 0.2% at energies higher than 2.0 GeV. In the opposite drift cycle ξ_θ increases from the low energy side up to ~ 100 MeV where it reaches a maximum value of ~ 0.24%, from where it drops sharply with increasing energy to negative values. The peak in ξ_θ in the equatorial plane in the A < 0 cycle is not present at $\theta = 55°$, but a similar peak in $3K_A \sin\psi G_r / v$ compared to that in the equatorial plane is evident and is widened.

The increased magnitude of ξ_θ for GCR protons at θ = 55° indicates that it may be observable at all radial distances during both polarity cycles.

Figure 6.11 is similar to Figure 6.9 but shows ξ_θ for ACR protons. It is evident from this figure that the behaviour of ξ_θ for ACRs in the equatorial plane at 1 AU is similar to GCRs in sense that it is positive at all energies less than 1.0 GeV in the A > 0 cycle and negative in the A < 0 cycle. But in terms of magnitude differences exist between the two species, for example, ACRs reach a maximum of ~ 0.1% in the A > 0 cycle and a minimum of ~ -0.035% in the A < 0 cycle. Also at 50 AU the behaviour is still similar to GCRs except for differences in the magnitude. However, at 91 AU significant differences occur, ξ_θ for ACRs is approximately zero at energies below ~ 50 MeV and decreases to negative values above this energy in the A > 0 cycle. In the A < 0 cycle it is zero at energies < ~ 40 MeV, changing drastically above this energy to large negative values. The difference with GCRs in this cycle is that the peak reached by ξ_θ for GCRs is not present for ACRs and the decrease in ξ_θ occurs at lower energies for ACRs than for GCRs. Furthermore, $3K_{\perp\theta}G_\theta / v$ increases sharply at energies > 300 MeV but not enough to have an effect on ξ_θ. As for GCRs, the energy dependence of ξ_θ for ACRs is determined by the energy dependence of mainly $3K_A \sin\psi G_r / v$ beyond 1 AU in the equatorial plane.

Figure 6.12 is similar to Figure 6.11 but at θ = 55°. Figure 6.12 illustrates that ξ_θ increases significantly when compared to its value in the equatorial plane, it reaches a maximum value of ~ 1.0% in the A > 0 cycle and a minimum of ~ -1.0% in the A < 0 cycle at 1 AU. It is also evident that $3K_A \sin\psi G_r / v$ remains approximately zero at 1 AU and that the energy dependence of ξ_θ is essentially determined by the energy dependence of $3K_{\perp\theta}G_\theta / v$ inside off the TS (1 and 50 AU). At 91 AU, the energy dependence of ξ_θ is determined by the energy dependence of $3K_A \sin\psi G_r / v$ and ξ_θ is approximately zero at lower energies but decreases with increasing energy in both polarity cycles but more significantly in the A < 0 cycle. It can be noted from Figure 6.12 that $3K_A \sin\psi G_r / v$ increases steadily with energy at a radial distance of 50 AU in the A < 0 cycle but decreases steadily with energy in the A > 0 cycle. At 50 AU, ξ_θ reaches a maximum of larger than 2.0% at low energies in both polarity cycles.

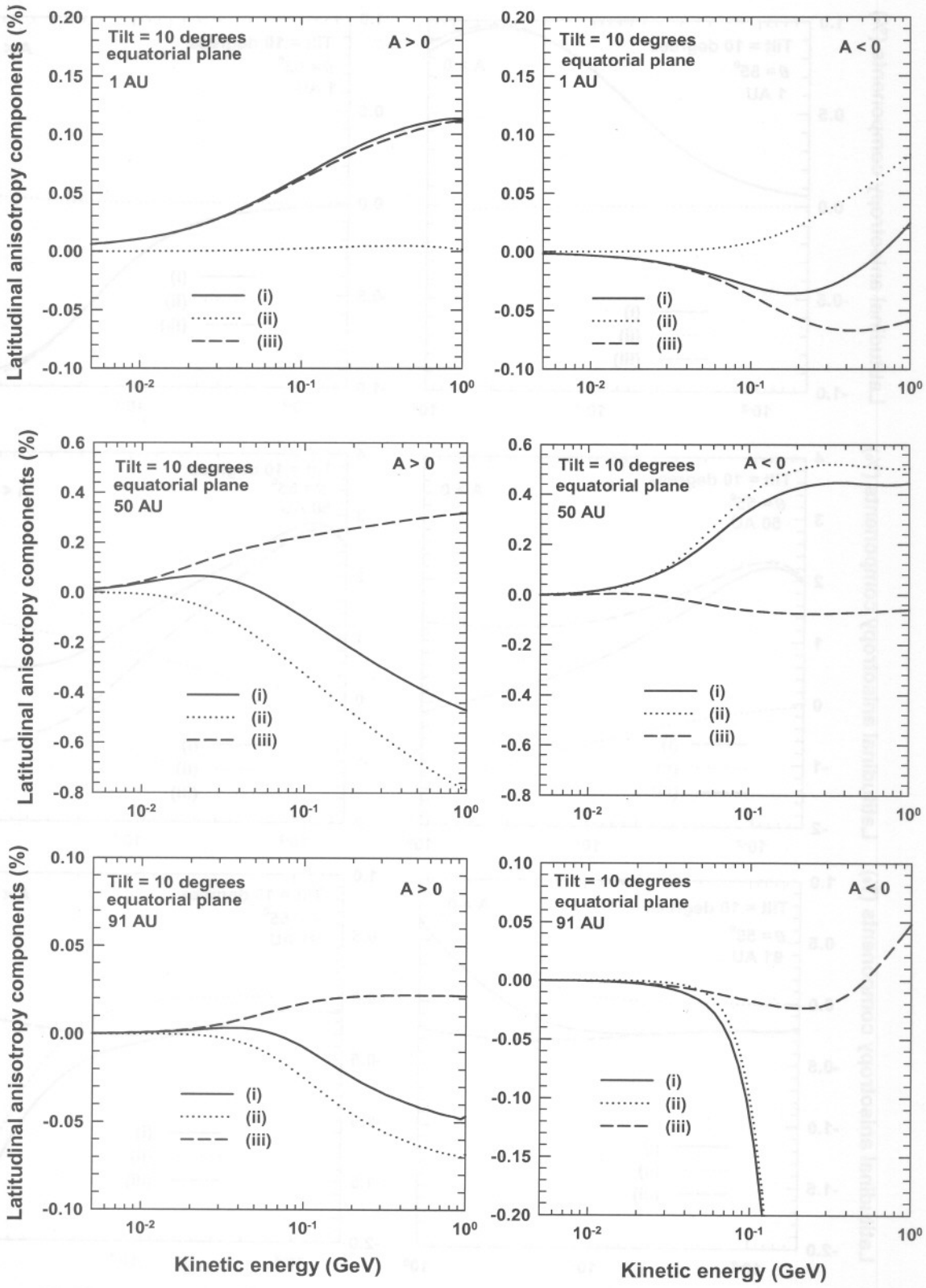

Figure 6.11. Similar to Figure 6.9, but for ACR protons.

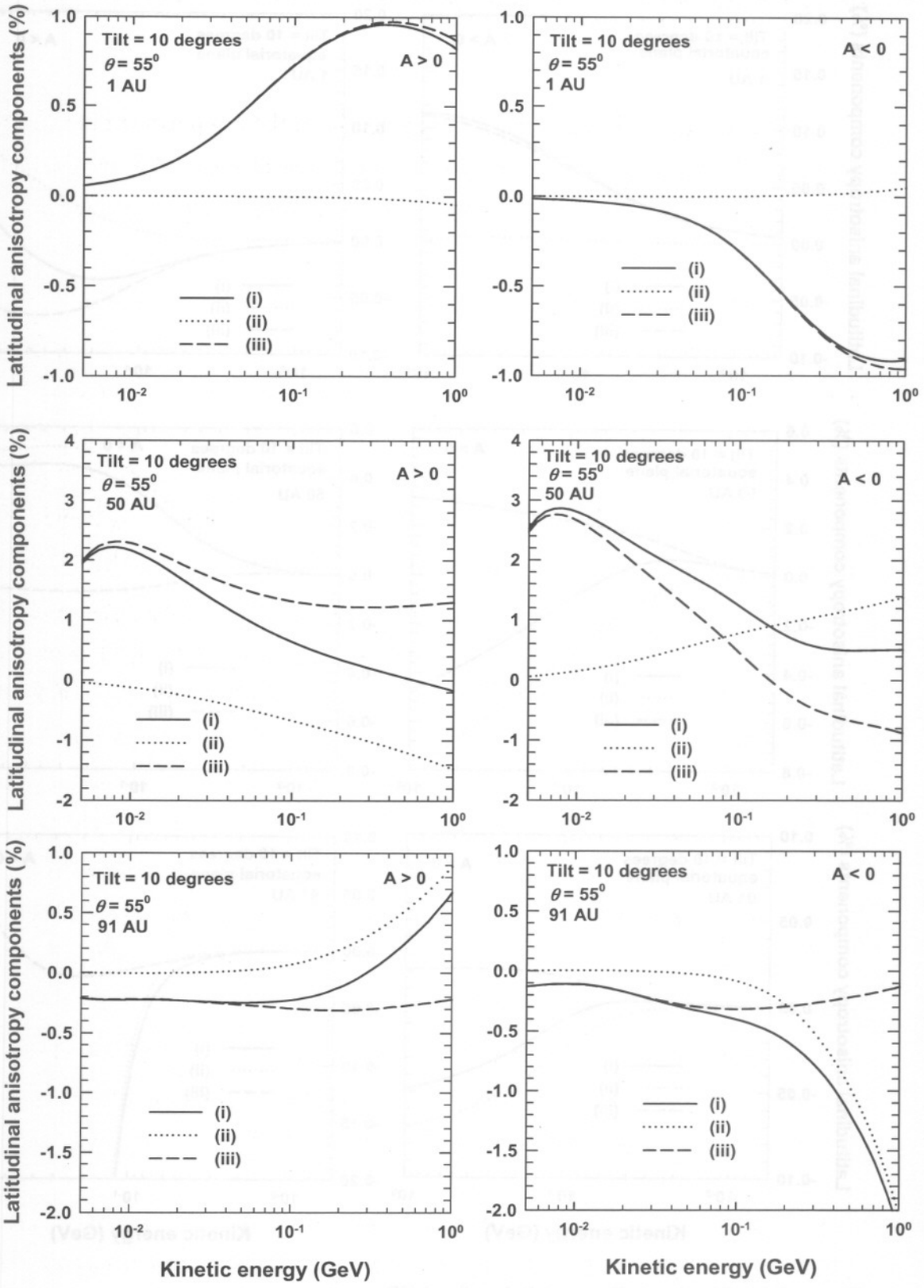

Figure 6.12. Similar to Figure 6.11 but at $\theta = 55°$.

6.5 The effects of the latitude dependence of the compression ratio and the injection efficiency on CR anisotropies.

In this section, the effects of the latitude dependence of the compression ratio s and of the injection efficiency, discussed in Chapter 4 and shown in Figure 4.3, on the radial and latitudinal anisotropies of GCR and ACR protons at different energies and radial distances in the heliosphere are studied and illustrated.

The computed ξ_r for GCR protons are shown in Figure 6.13 as a function of kinetic energy for both polarity cycles in the equatorial plane (left panel) and $\theta = 55°$ (right panel), at radial distances of 1, 50 and 91 AU, respectively, and for solar minimum conditions ($\alpha = 10°$). Two sets of anisotropies are shown, first without a latitude dependence (black lines) and then with a latitude dependence of s (red lines). As before, the TS is at 90 AU and the HP, where the LIS is specified, is located at 120 AU. Evident from this figure is that the effects of the latitude dependence of s on ξ_r for GCRs are only just noticeable at energies $< \sim 400$ MeV at 1 AU in both polarity cycles and latitudes. When the distance is increased to 50 AU these effects become accentuated, more prominently at $\theta = 55°$ in both cycles. In the equatorial plane at 50 AU these effects are only noticeable at energies < 100 MeV in the A > 0 cycle, whereas in the A < 0 cycle they are prominent up to 1.0 GeV. At $\theta = 55°$ and 50 AU the differences become prominent up to 1.0 GeV in both polarity cycles. Above 1.0 GeV the differences diminish in both polarity cycles at 50 AU. At 91 AU, which is a special case beyond the TS, these effects are prominent at all energies in both polarity cycles and latitudes except in the A > 0 cycle in the equatorial plane where the difference between the two approaches becomes insignificant at energies above 400 MeV. Significant differences between ξ_r with and without the latitude dependence of s increases with decreasing energy and it is large in the A < 0 cycle than in the A > 0 cycle. In general, differences between the two approaches become unnoticeable at energies above ~ 1.0 GeV upwind of the TS (at 1 and 50 AU), but beyond the TS (at 91 AU) they are noticeable at all energies and more profoundly in the A < 0 cycle.

In terms of magnitude of the difference between the two approaches, there is an energy region where ξ_r with the latitude dependent s is larger or smaller than that without. At 50

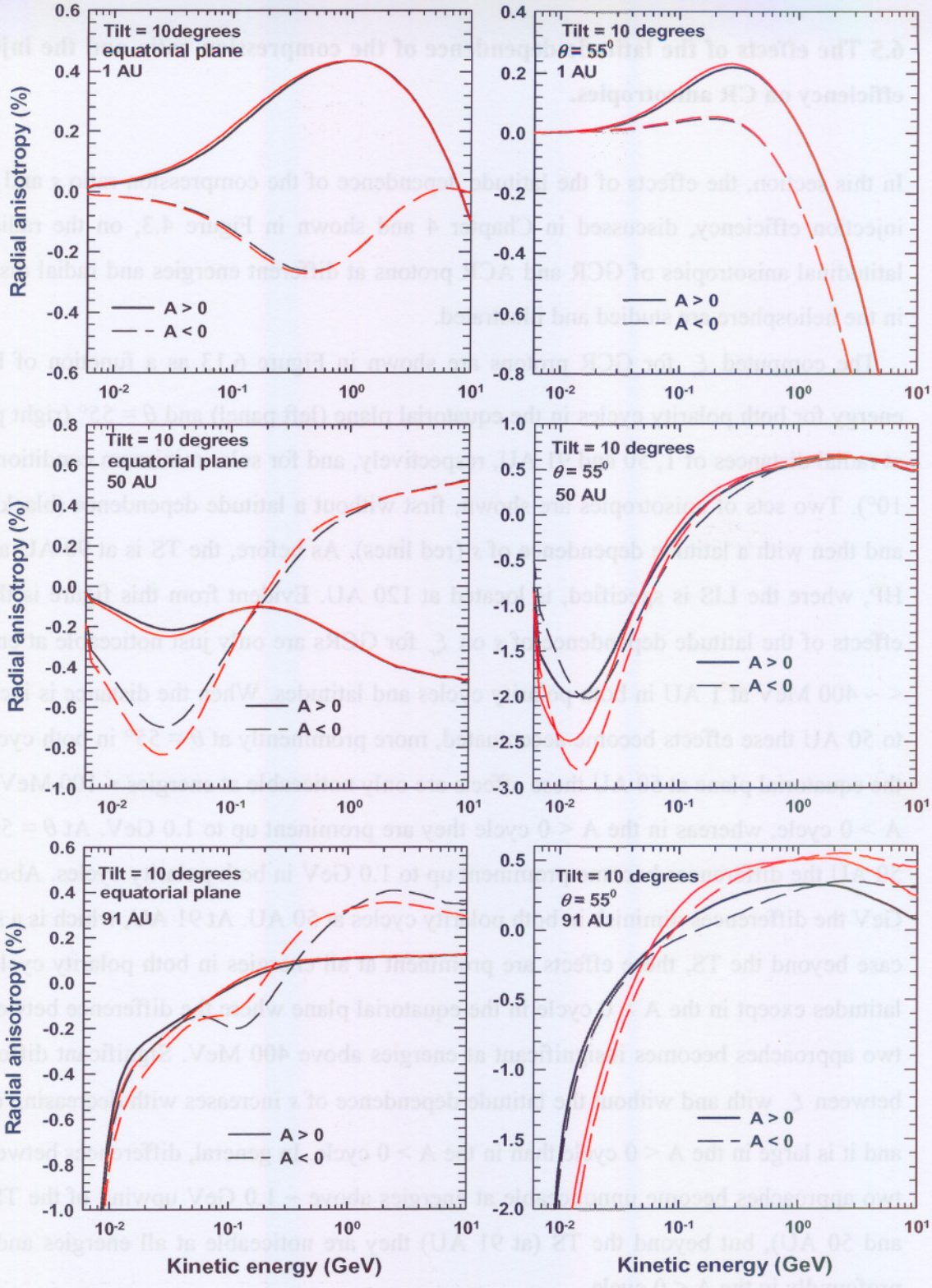

Figure 6.13. Computed ξ_r for GCR protons as a function of kinetic energy for both polarity cycles in the equatorial plane (left panel) and $\theta = 55°$ (right panel) at radial distances of 1, 50 and 91 AU respectively, and for solar minimum conditions ($\alpha = 10°$). Two sets of anisotropies are shown, first without a latitude dependence (black lines) and second with a latitude dependence of s (red lines). The TS is at 90 AU and the HP, where the LIS is specified, is at 120 AU.

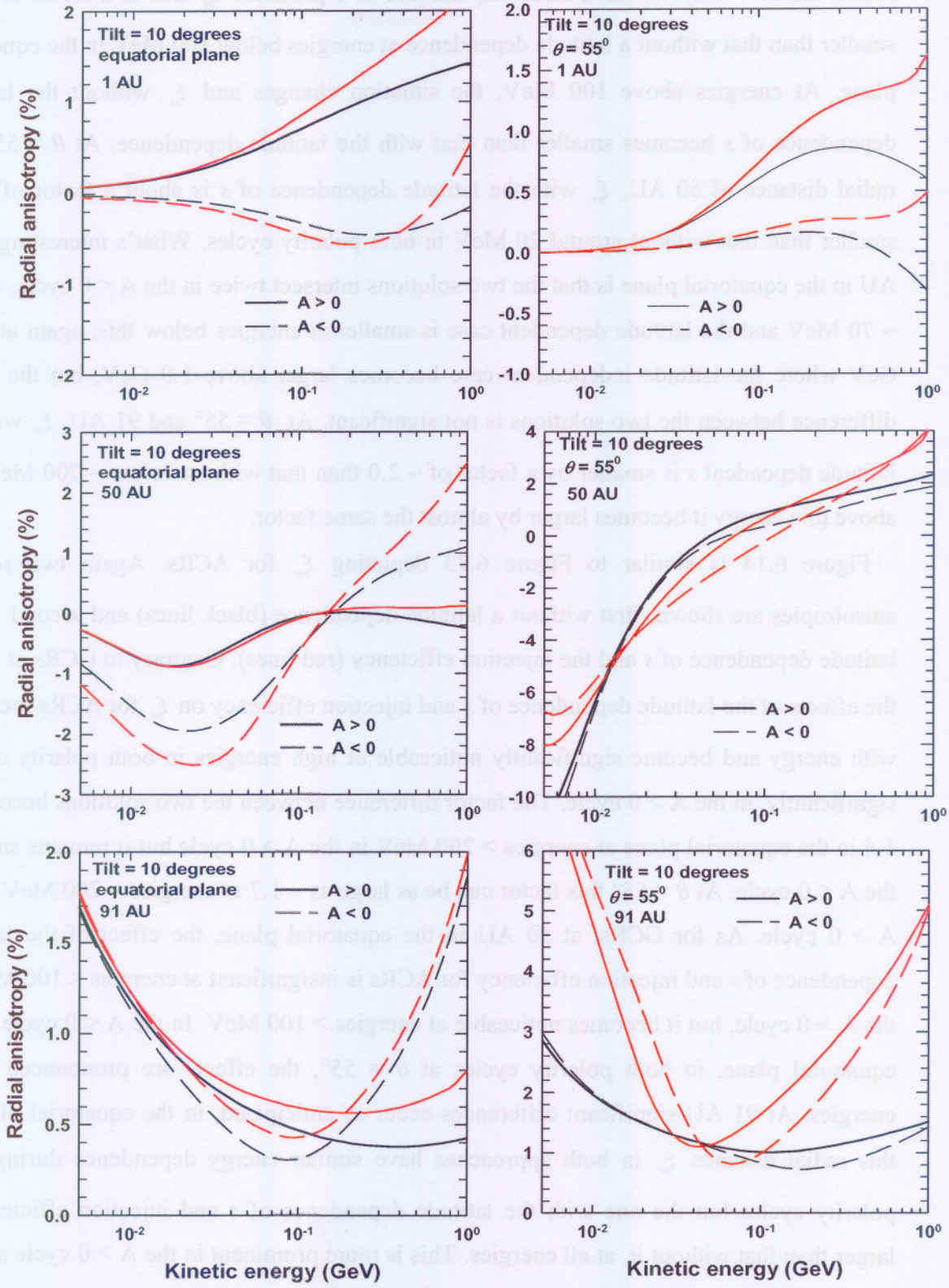

Figure 6.14. Similar to Figure 6.13 with ξ_r now shown for ACRs. Two sets of anisotropies are shown, first without a latitude dependence (black lines) and second with a latitude dependence of s and the injection efficiency (red lines).

AU in the A < 0 cycle, the latitude dependence of s produces ξ_r that is a factor of ~ 1.3 smaller than that without a latitude dependence at energies below 100 MeV in the equatorial plane. At energies above 100 MeV, the situation changes and ξ_r without the latitude dependence of s becomes smaller than that with the latitude dependence. At $\theta = 55°$ and radial distance of 50 AU, ξ_r with the latitude dependence of s is about a factor of ~ 2.0 smaller than that without around 20 MeV in both polarity cycles. What's interesting at 91 AU in the equatorial plane is that the two solutions intersect twice in the A < 0 cycle, first at ~ 70 MeV and the latitude dependent case is smaller at energies below this, again at ~ 1.0 GeV where the latitude independent case becomes larger above 1.0 GeV, but the factor difference between the two solutions is not significant. At $\theta = 55°$ and 91 AU, ξ_r with the latitude dependent s is smaller by a factor of ~ 2.0 than that without below ~ 700 MeV and above this energy it becomes larger by almost the same factor.

Figure 6.14 is similar to Figure 6.13 depicting ξ_r for ACRs. Again two sets of anisotropies are shown, first without a latitude dependence (black lines) and second with a latitude dependence of s and the injection efficiency (red lines). Contrary to GCRs at 1 AU, the effects of the latitude dependence of s and injection efficiency on ξ_r for ACRs increases with energy and become significantly noticeable at high energies in both polarity cycles, significantly in the A > 0 cycle. The factor difference between the two solutions becomes ~ 1.4 in the equatorial plane at energies > 200 MeV in the A > 0 cycle but it remains small in the A < 0 cycle. At $\theta = 55°$ this factor can be as large as ~ 1.7 at energies > 200 MeV in the A > 0 cycle. As for GCRs, at 50 AU in the equatorial plane, the effect of the latitude dependence of s and injection efficiency for ACRs is insignificant at energies < 100 MeV in the A > 0 cycle, but it becomes noticeable at energies > 100 MeV. In the A < 0 cycle in the equatorial plane, in both polarity cycles at $\theta = 55°$, the effects are pronounced at all energies. At 91 AU significant differences occur as anticipated, in the equatorial plane at this radial distance ξ_r in both approaches have similar energy dependence during both polarity cycles but the one with the latitude dependence of s and injection efficiency is larger than that without it, at all energies. This is more prominent in the A > 0 cycle at high energies. At $\theta = 55°$ the latitude dependence of the two parameters changes the energy dependence of ξ_r markedly in both polarity cycles and quantitatively it increases ξ_r by a factor of more than ~ 2.0 at both high and lower energy regions. However, between ~ 30 MeV and ~ 50 MeV the latitude dependence of s and injection efficiency produces ξ_r that

is slightly lower than that without in the A > 0 cycle and this occurs between ~ 40 MeV and ~ 100 MeV in the A < 0 cycle.

Figure 6.15 shows the computed ξ_θ for solar minimum conditions (α = 10°) for GCR protons as a function of kinetic energy for both polarity cycles in the equatorial plane (left panel) and θ = 55° (right panel) at radial distances of 1, 50 and 91 AU respectively. Again the two sets of anisotropies are shown. Very small differences in ξ_θ between the two solutions can be noticed at low energies at 1 AU in both polarity cycles similar to ξ_r for the same species. This emphasizes the fact that the latitude dependence of s may not at all affect modulation of GCRs at Earth. At 50 AU in the equatorial plane (left panel), no difference between the two solutions is noted in the A > 0 cycle at all energies, while in the A < 0 cycle some differences are noted at energies < 1.0 GeV. However, at θ = 55° and 50 AU significant difference are noted, only < ~ 200 MeV in the A > 0 cycle, to the extent that ξ_θ with a latitude dependence of s is a factor of ~ 1.4 larger than that without, at energies < ~ 40 MeV, whereas in the A < 0 cycle this factor approaches ~ 2.0 at lower energies. The difference between the two drift cycles at θ = 55° and 50 AU is that in the A < 0 cycle the effect of the latitude dependence of s is noted at all energies and it has a decreasing trend with energy. Interesting is that up-stream of the TS the energy dependence of ξ_θ for GCRs seem not to be qualitatively changed by the latitude dependence of s in both polarity cycles. At 91 AU in the equatorial plane in the A > 0 cycle ξ_θ for GCRs is very small in the context of the scale used so that the effect of the latitude dependence of s on it cannot be seen. However in the A < 0 cycle the effect is accentuated, decreasing ξ_θ at energies < 1.0 GeV. At θ = 55° and 91 AU, the effect is pronounced and the energy dependence of ξ_θ changes markedly especially at energies below 200 MeV. Quantitatively, ξ_θ with a latitude dependence of s increases by a factor of about ~ 4.0 at energies below ~ 200 MeV in the A > 0 cycle while in the A < 0 cycle this factor can be as large as ~ 5 at lower energies but it decreases significantly with increasing energy.

Figure 6.16 is similar to Figure 6.15 with ξ_θ now depicted for ACR protons. Two sets of anisotropies are shown as before. It is evident that at 1 AU significant differences can be noted between the two solutions, unlike for GCRs, and these differences increase with energy similar to ξ_r for the same species at 1 AU, and it is pronounced at θ = 55° especially

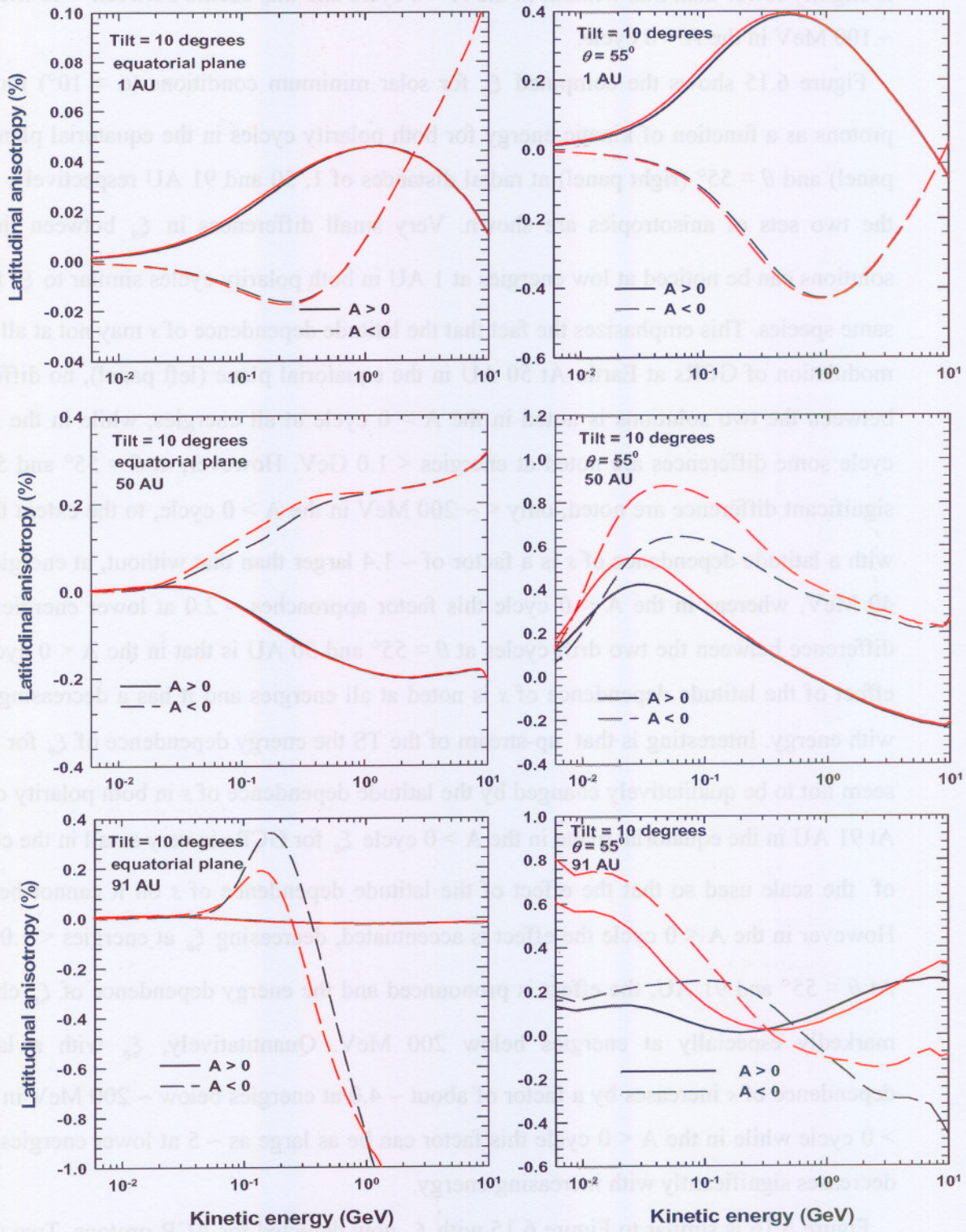

Figure 6.15. Computed ξ_θ for GCR protons as a function of kinetic energy for both polarity cycles in the equatorial plane (left panel) and $\theta = 55°$ (right panel) at radial distances of 1, 50 and 91 AU respectively, and for solar minimum conditions ($\alpha = 10°$). Two sets of anisotropies are shown, first without a latitude dependence (black lines) and second with a latitude dependence of s (red lines). The TS is at 90 AU and the HP, where the LIS is specified, is at 120 AU.

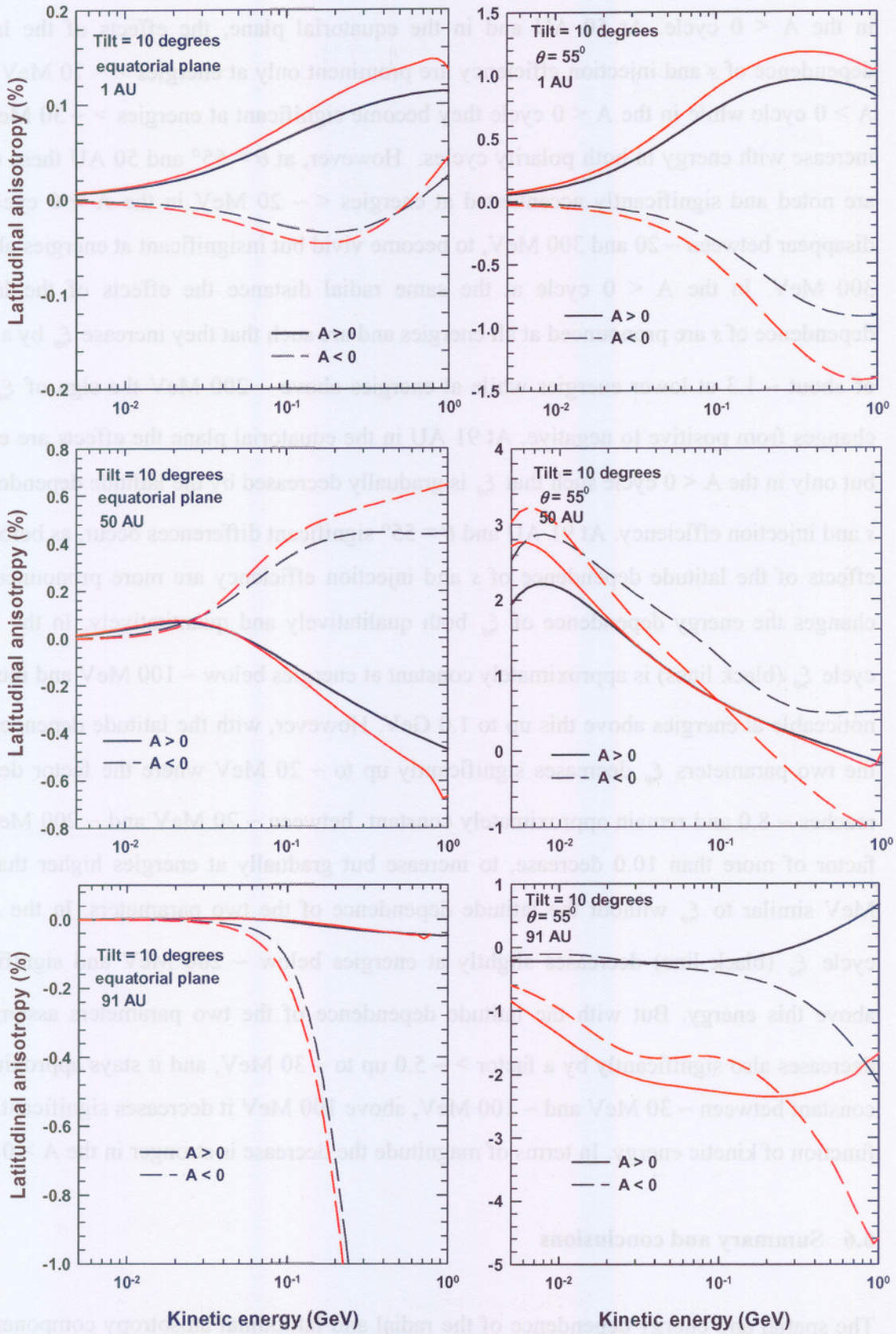

Figure 6.16. Similar to Figure 6.15 with ξ_θ shown for ACR protons. Two sets of anisotropies are shown, first without a latitude dependence (black lines) and second with a latitude dependence of s and injection efficiency (red lines).

in the A < 0 cycle. At 50 AU and in the equatorial plane, the effects of the latitude dependence of s and injection efficiency are prominent only at energies > ~ 70 MeV in the A > 0 cycle while in the A < 0 cycle they become significant at energies > ~ 30 MeV and increase with energy in both polarity cycles. However, at $\theta = 55°$ and 50 AU these effects are noted and significantly accentuated at energies < ~ 20 MeV in the A > 0 cycle, but disappear between ~ 20 and 300 MeV, to become vivid but insignificant at energies above ~ 300 MeV. In the A < 0 cycle at the same radial distance the effects of the latitude dependence of s are pronounced at all energies and are such that they increase ξ_θ by a factor of about ~ 1.3 at lower energies while at energies above ~ 200 MeV the sign of ξ_θ even changes from positive to negative. At 91 AU in the equatorial plane the effects are evident but only in the A < 0 cycle such that ξ_θ is gradually decreased by the latitude dependence of s and injection efficiency. At 91 AU and $\theta = 55°$ significant differences occur, as before, the effects of the latitude dependence of s and injection efficiency are more pronounced and changes the energy dependence of ξ_θ both qualitatively and quantitatively. In the A > 0 cycle ξ_θ (black lines) is approximately constant at energies below ~ 100 MeV and increases noticeable at energies above this up to 1.0 GeV. However, with the latitude dependence of the two parameters ξ_θ decreases significantly up to ~ 20 MeV where the factor decrease reaches ~ 8.0 and remain approximately constant between ~ 20 MeV and ~ 200 MeV at a factor of more than 10.0 decrease, to increase but gradually at energies higher than 200 MeV similar to ξ_θ without the latitude dependence of the two parameters. In the A < 0 cycle ξ_θ (black line) decreases slightly at energies below ~ 200 MeV and significantly above this energy. But with the latitude dependence of the two parameters assumed ξ_θ decreases also significantly by a factor > ~ 5.0 up to ~ 30 MeV, and it stays approximately constant between ~ 30 MeV and ~ 100 MeV, above 100 MeV it decreases significantly as a function of kinetic energy. In terms of magnitude the decrease is stronger in the A > 0 cycle.

6.6 Summary and conclusions

The spatial and energy dependence of the radial and latitudinal anisotropy components for both GCRs and ACRs are computed with a TS-modulation model. This is done at radial distances of 1, 50 and 91 AU and at energies of 0.016, 0.08, 0.2, 0.5 and 1.0 GeV respectively. These anisotropy components are first computed without a latitude

dependence of the compression ratio of the TS and for the injection efficiency of the source of the ACRs, and then with a latitudinal dependence of both the compression ratio and injection efficiency. Results are shown close to the equatorial plane and at $\theta = 55°$.

The magnitude and direction of the radial anisotropy strongly depends on the position in the heliosphere and the energy of particles, e.g. ξ_r is positive in the A > 0 cycle but negative in the A < 0 cycle at 1 AU for both GCRs and ACRs close to the equatorial plane, but at $\theta = 55°$ it is positive at energies below 1.0 GeV and negative above this energy during both polarity cycles.

The energy dependence of ξ_r for both GCRs and ACRs at 50 and 91 AU, and for both latitudes is found to be essentially determined by the Compton-Getting anisotropy in both polarity cycles and stronger at low energies, and this behaviour for ξ_r is an attribute of the spectral shape at these radial distances. However at Earth, the energy dependence for ξ_r for both species in the equatorial plane is found to be dominated by the energy dependence of diffusion anisotropy in the A < 0 cycle at energies < ~ 100 MeV, while in the A > 0 cycle it remains dominated by the Compton-Getting anisotropy. Whereas at $\theta = 55°$, where the drift anisotropy is found to be negligible, the energy dependence of ξ_r for GCRs is dominated by the diffusion anisotropy at Earth in both polarity cycle at energies > 1.0 GeV. But ξ_r for ACRs is still dominated by the Compton-Getting anisotropy in the A > 0 cycle, while in the A < 0 cycle the balance between the Compton-Getting and diffusion anisotropy is almost reached and ξ_r is found to be approximately zero at all energies of interest.

The main effect of the TS on ξ_r for ACRs is to increase its value when crossing into the heliosheath in both polarity cycles, while for GCRs this is only true in the A > 0 cycle and in the equatorial plane. In all cases ξ_r becomes positive beyond the TS for quite a distance. Closer to the HP, ξ_r becomes negative for GCRs in the A > 0 cycle in the equatorial plane, while for ACRs it remains positive. At $\theta = 55°$, ξ_r stays positive for GCRs throughout the heliosphere at all energies of interests and both drift cycles except at small radial distances close to the Sun in the A < 0 cycle for 0.2 GeV. For ACRs, it is positive at 0.2 GeV throughout the heliosphere, whereas at 0.08 GeV in the A < 0 cycle and at 0.016 GeV in both polarity cycles, it can either be positive or negative at certain distances.

The analysis of ξ_r for a few AUs in front and behind the shock (70-110 AU) requires that ξ_r for ACR protons in the downstream region, where the solar wind is low, is larger than the upstream value for both polarity cycles, and close to the equatorial plane and at $\theta = 55°$.

The effects on ξ_r of making the compression ratio latitude dependent for GCRs become unnoticeable at energies above ~ 1.0 GeV upstream of the TS (at 1 and 50 AU), but beyond the TS (at 91 AU) they are noticeable at all energies, and more profoundly in the A < 0 cycle. At Earth these effects are insignificant at all energies for GCR protons, but for ACR protons they are significant even at Earth and more prominently at 91 AU. The analysis of the latitudinal dependence of the compression ratio and the injection efficiency strongly indicates that these two parameters can change the magnitude of the radial anisotropy as well as its direction (sign) at certain energies and positions for both GCRs and ACRs, causing a rather complicated picture for ξ_r.

The magnitude of ξ_θ for GCR protons at Earth is very small in both polarity cycles and this may suggest that it may not be easily observable in the equatorial plane, however at $\theta =$ 55° the magnitude increased significantly and it is dominated by the anisotropy due to diffusion of particles in the polar direction at lower energies at all radial distances of interests. Similar arguments hold for ACR protons. It is found that at 91 AU and at energies > ~ 100 MeV the energy dependence of ξ_θ for both GCRs and ACRs is dominated by the energy dependence of drift anisotropy especially in the A < 0 cycle.

The effects of the latitude dependence of s and injection efficiency on ξ_θ for GCRs are insignificant at 1 AU in both polarity cycles, but significant for ACRs. However, at 50 and 91 AU these effects become accentuated especially at lower energies and change the trend of ξ_θ both qualitatively and quantitatively for both GCRs and ACRs at 91 AU. Quantitatively, ξ_θ with a latitude dependent s increases by a factor of about ~ 4.0 at low energies in the A < 0 cycle for GCRs while for ACRs this factor can be as large as ~ 8.0.

Chapter 7

Summary and conclusions

After introducing the study of modulation of galactic and the anomalous component of cosmic rays protons in the heliosphere in **Chapter 1**, an overview was given in **Chapter 2** of the Sun, the solar wind, the heliospheric magnetic field, the heliospheric current sheet, solar cycle variations, the heliosphere and its geometry and charged particles in the heliosphere. A concise discussion was also given about selected spacecraft missions.

In **Chapter 3**, a discussion of the transport processes combined in the transport equation (Parker, 1965), as well as a brief discussion of the 2D shock acceleration model used for this work was given. A description of diffusive shock acceleration, and the diffusion tensor constructed by Langner (2004), used in this work, was also given.

In **Chapter 4**, the hydrodynamic modelling results of Scherer et al. (2006) were used to establish the latitude dependence of the TS compression ratios and the injection efficiency (source strength) of ACRs (see Equation 4.1 and Figure 4.3). Modulation effects associated with the latitude dependences of these two parameters on GCRs and ACRs were computed, using the 2D shock acceleration model of Langner (2004), comparing them to those without latitude dependence for both the termination shock parameters. The computations were shown for both polarity cycles in the equatorial plane and at $\theta = 55°$, and for solar minimum conditions.

It was found that for GCR protons in the equatorial plane the effects of the latitude dependent s were insignificant up-stream of the shock in the A > 0 cycle, with the effects almost disappearing completely at Earth, compared to the A < 0 cycle. But these effects were enhanced at $\theta = 55°$ at the TS position and at 50 AU especially in the A < 0 cycle, with the intensities reaching about a factor of ~ 2 higher at energies < ~ 80 MeV at the TS position. Furthermore, the effect of the latitude dependence of s was found to shift the maximum in the spectra slightly to lower energies in the heliosphere.

For ACRs, first the effects of only the latitude dependent s were shown in the equatorial plane and $\theta = 55°$. It was found that they are more significant in the inner heliosphere, with the intensities about a factor of ~ 10 less; and this difference was found to be larger in the A > 0 cycle than in the A < 0 cycle, in contrast to GCRs. The computational results in addition to the difference in intensities were focused on the effects of the latitude dependence of s,

emphasizing three issues: (1) The power-law dependence of the ACR spectra at the TS position; (2) The enhancement of the CR intensity, a "bump" (more correctly a change in the shock spectral index with increasing energy), in the spectrum just below the cut-off energy (before the roll-over starts) of ACR at the TS position, which is prominent for the A < 0 cycle but almost absent in the A > 0 drift cycle, also found by Steenkamp (1995) and Langner (2004). le Roux et al. (1996) and later also Florinski and Jokipii (2003) showed that a similar "bump" could also be obtained in purely spherically symmetric geometry with no drifts; and (3) the high-energy cut-off of the shock spectra. The two solutions, with and without the latitude dependence of s, were found to have the same required spectral index in the equatorial plane, but at $\theta = 55°$ the latitude dependence of s produced a much steeper spectra. For the cut-off energies, this latitude dependence was found to shift the cut-off energies to lower energies, more significantly at $\theta = 55°$. The "bump" was found to be largely diminished in the equatorial plane even in the A < 0 cycle, whereas at $\theta = 55°$ it reappeared only in the A < 0 cycle.

Second, s was kept constant over latitudes and only the injection efficiency (source of ACRs) was varied. The intensities upstream of the TS were reduced by a factor of ~ 5 and this factor was larger in the A < 0 cycle than in the A > 0 cycle. The cut-off energies have been shifted to lower energies as in the case discussed above. The "bump" before the cut-off energy was found to have been wiped out even at $\theta = 55°$ in the A < 0 cycle.

Third, the latitude dependences of s and the injection efficiency were combined. In this case the cut-off energies have been further shifted to lower energies. The "bump" before the cut-off energies was wiped out in the equatorial plane, but it reappeared at $\theta = 55°$ and this time in both drift cycles. This was similar to what Florinski and Jokipii (2003) found using a purely spherically symmetric geometry with no drifts. And finally, the latitude dependences of s and the injection efficiency were combined with the stronger decreasing V in the heliosheath, $V \propto 1/r^3$. The qualitative picture looked similar to the one when only the latitude dependences of s and the injection efficiency were assumed and $V \propto 1/r^2$ in the heliosheath, except as a function of radial distance and at 16 MeV, where the intensities showed a slight increase in the heliosheath that was obviously caused by the negative divergence of **V**.

In **Chapter 5** the radial and latitudinal intensity gradients were computed and it was found that the radial gradient of GCR protons varied with polarity in the equatorial plane and increased with decreasing radial distance in the inner heliosphere in the A < 0 cycle. This radial gradient was larger in the A < 0 cycle than in the A > 0 cycle at radial distances

of $r < \sim 40$ AU. Whereas at $\theta = 55°$ the trend as a function of radial distance in both polarity cycles was similar. Similar results to these were found for ACR protons, but at different energies. When crossing the TS into the heliosheath, the radial gradient changed abruptly and this effect varied significantly with particle energy for GCRs, while for ACRs the radial gradient decreased at all energies of interest in the heliosheath.

The latitude dependences of s and injection efficiency increased and shifted the maximum radial gradient to lower energies for GCRs and to higher energies for ACRs upstream of the TS. When the latitude dependences of these two parameters were combined with $V \propto 1/r^3$ in the heliosheath, it was found that the effects of adiabatic acceleration in the heliosheath on the radial gradient for ACR protons were only prominent at 16 MeV, whereas at 0.08 and 0.2 GeV (the three energies investigated) they were cancelled by increasing modulation effects such as drifts and diffusion.

The polar gradient for both GCRs and ACRs was found to display variations in a systematic way with the 11-year polarity cycle inside the TS in the equatorial plane. Beyond the TS at 91 AU for GCRs, it has negative values at lower energies and nearly zero at higher energies in both cycles. This behaviour was different for ACRs at 91 AU.

The latitude dependence of s and injection efficiency increased and shifted the maximum polar gradient for ACRs to higher energies in the $A > 0$ and to lower energies in the $A < 0$ cycle, while for GCRs this effect was found not to vary with polarity cycle.

In **Chapter 6** it was found that the magnitude and direction of the radial anisotropy strongly depended on the position in the heliosphere and the energy of particles, e.g. ξ_r was positive in the $A > 0$ cycle but negative in the $A < 0$ cycle at 1 AU for both GCRs and ACRs close to the equatorial plane. But at $\theta = 55°$ it was positive at energies below 1.0 GeV and negative above this energy during both polarity cycles. The energy dependence of ξ_r for both GCRs and ACRs at 50 and 91 AU, and for both latitudes was essentially determined by the Compton-Getting anisotropy in both polarity cycles and stronger at low energies, and this behaviour for ξ_r was an attribute of the spectral shape at these radial distances. However at Earth, the energy dependence for ξ_r for both species in the equatorial plane was dominated by the energy dependence of the diffusion anisotropy in the $A < 0$ cycle at energies $< \sim 100$ MeV, while in the $A > 0$ cycle it remained dominated by the Compton-Getting anisotropy. At $\theta = 55°$, where the drift anisotropy was negligible, the energy dependence of ξ_r for GCRs was dominated by the diffusion anisotropy at Earth in

both polarity cycle at energies > 1.0 GeV. But ξ_r for ACRs was still dominated by the Compton-Getting anisotropy in the A > 0 cycle, while in the A < 0 cycle the balance between the Compton-Getting and diffusion anisotropy was almost reached and ξ_r was approximately zero at all energies of interest.

The main effect of the TS on ξ_r for ACRs was to increase its value when crossing into the heliosheath in both polarity cycles, while for GCRs this was only true in the A > 0 cycle and in the equatorial plane. In all cases ξ_r became positive beyond the TS for quite a distance. Closer to the HP, ξ_r became negative for GCRs in the A > 0 cycle in the equatorial plane, while for ACRs it remained positive. At $\theta = 55°$, ξ_r stayed positive for GCRs throughout the heliosphere at all energies of interests and drifts cycles except at small radial distances close to the Sun in the A < 0 cycle for 0.2 GeV. For ACRs, it was positive at 0.2 GeV throughout the heliosphere, whereas at 0.08 GeV in the A < 0 cycle and at 0.016 GeV in both polarity cycles, it could either be positive or negative at certain distances.

The analysis of ξ_r for a few AUs in front and behind the shock (70-110 AU) required that ξ_r for ACR protons in the downstream region, where the solar wind speed was low, was larger than the upstream value for both polarity cycles.

The effects on ξ_r of making the compression ratio latitude dependent for GCRs were unnoticeable at energies above ~ 1.0 GeV up-stream of the TS (at 1 and 50 AU), but beyond the TS (at 91 AU) they were noticeable at all energies, and more profoundly in the A < 0 cycle. At Earth these effects were insignificant at all energies for GCR protons, but for ACR protons they were significant even at Earth and more prominently at 91 AU. The analysis of the latitudinal dependence of s and the injection efficiency strongly indicated that these two TS parameters could change the magnitude of the radial anisotropy as well as its direction (sign) at certain energies and positions for both GCRs and ACRs, causing a rather complicated picture for ξ_r.

The magnitude of ξ_θ for GCR protons at Earth was very small in both polarity cycles and this may suggest that it may not be easily observable in the equatorial plane, however at $\theta =$ 55° the magnitude increased significantly and it was dominated by the anisotropy due to diffusion of particles in the polar direction at lower energies at all radial distances of interests. Similar arguments held for ACR protons. At 91 AU and at energies > ~ 100 MeV

the energy dependence of ξ_θ for both GCRs and ACRs was dominated by the energy dependence of drift anisotropy especially in the A < 0 cycle.

The effects of the latitude dependence of s and injection efficiency on ξ_θ for GCRs were insignificant at 1 AU in both polarity cycles, but significant for ACRs. However, at 50 and 91 AU these effects became accentuated especially at lower energies and changed the trend of ξ_θ qualitatively and quantitatively for both GCRs and ACRs at 91 AU. Quantitatively, ξ_θ with a latitude dependent s increased by a factor of about ~ 4.0 at low energies in the A < 0 cycle for GCRs while for ACRs this factor could be as large as ~ 8.0.

It is concluded that:

- The establishment of the latitude dependences of the compression ratio and the injection efficiency (source strength of ACR) is important for modulation models with diffusive shock acceleration and it enables an improved description of the modulation of ACRs beyond the TS.
- This work is a theoretical study, hence the computations were not for the purpose of fitting observations. However, the latitude dependence of the compression ratio and the injection efficiency illustrated that it is possible to obtain a TS spectrum for ACRs at θ = 55° that qualitatively resembles V1 observations, emphasizing that this model improvement contains certain new features of the TS particles as observed by V1. (See also Langner and Potgieter, 2006).
- The enhancement in the ACR spectrum, the "bump" just below the cut-off energy, before the roll-over starts, is prominent for the A < 0 cycle in the equatorial plane. The cause of this feature should be investigated further.
- The global anisotropy vector of both GCRs and ACRs was successfully computed and illustrated for the outer heliosphere during solar minimum conditions and for opposite magnetic polarity cycles. The slower solar wind speed beyond the TS causes interesting global effects on the anisotropy vector. The anisotropy vector evidently depends on many factors in a complicated way, so care must be taken when interpreting it.
- The numerical modeling study of the acceleration of cosmic ray particles at the TS helps to improve our knowledge of cosmic ray modulation in the heliosheath. However, the understanding of the physics in this rather complex region is just at its beginning.

For future studies the following recommendations are made:

- Extend the study to include solar maximum conditions.
- Inclusion of a non-radial solar wind velocity in the heliosheath in the present 2D model. This also means that the magnetic field geometry in the heliosheath will have to be re-investigated.
- Investigate the additional modulation and acceleration effects that a stochastic acceleration approach in the heliosheath could produce.
- Altering the 2D code to study diffusive shock acceleration at the TS as a function of azimuthal angle instead of polar angle so that the suggestion of McComas and Schwadron (2006) about effective acceleration of ACRs in the flanks of the heliosphere can directly be modeled and thus evaluated.
- The extension of the 2D time-dependent shock acceleration model into 3D. This would be a major accomplishment.
- Further investigation of the increase in ACRs intensities and the peculiar temporal behaviour of the anisotropies (Giacalone and Jokipii, 2006) beyond the TS.
- Incorporating the end results of the HD modeling that have been done in the local group (Ferreira and Scherer, 2006) into the transport model as described for this work.

REFERENCES

Axford, W. I., E. Leer, and G. Skadron, The acceleration of cosmic rays by shock waves, *Proc. 15th Inter. Cosmic Ray Conf. (Plovdiv), 11*, 132, 1977.

Balogh, A., E. J. Smith, B. T. Tsurutani, D. J. Southwood, R. J. Forsyth, and T. S. Horbury, The Heliospheric Magnetic Field Over the south polar region of the Sun, *Science, 268* (5213), 1007, 1995.

Balogh, A., R. G. Marsden, and E. J. Smith, (Eds.), The heliosphere near solar minimum: The Ulysses perspective, 411 pp., Springer-Praxis, London, 2001.

Baranov, V. B., and Y. G. Malama, Model of solar wind interaction with the local interstellar medium: Numerical solution of self-consistent problem, *J. Geophys. Res., 98*(A9), 15, 1993.

Bell, A. R., The acceleration of cosmic rays in shock fronts – I, *Monthly Notices of the Royal Astronomical Society, 182*, 147, 1978a.

Bell, A. R., The acceleration of cosmic rays in shock fronts – II, *Monthly Notices of the Royal Astronomical Society, 182*, 443, 1978b.

Bieber, J. W., W. H. Matthaeus, C. W. Smith, W. Wanner, M-B. Kallenrode, and G. Wibberenz, Proton and electron mean free paths: The Palmer consensus revisited, *Astrophys. J., 420*(1), 294, 1994.

Biermann, L., Kometenschwiefe und solare Korpuskularstrahlung, *Zeit. Astrophys., 29*, 274, 1951.

Biermann, L., The solar wind and the interplanetary media, in *Space Astrophysics*, edited by W. Liller, McGraw-Hill, New York, 150, 1961.

Borrmann, T., Ein hydrodynamisches 3D-mehrkomponente modell der Heliosphaere and ihrer wechselwirkung mit kosmicher strahlung, *Ph.D Thesis, Ruhr-Universität Bochum*, Germany , 2005.

Borrmann, T., and H. Fichtner, On the dynamics of the heliosphere on intermediate and long time-scales, *Adv. Space Res., 35*(12), 2091, 2005.

Burger, R. A., On the theory and application of drift motion of charged particles in inhomogenous magnetic fields, *Ph.D. thesis, Potchefstroom University for C.H.E.*, South Africa, 1987.

Burger, R. A., Cosmic-ray modulation and the heliospheric magnetic field, *Adv. Space Res., 35*, 636, 2005.

Burger, R. A., and M. Hattingh, Effects of Fisk-type heliospheric magnetic field on the latitudinal transport of cosmic rays, *Proc. 27th Inter. Cosmic Ray Conf. (Hamburg)*, 9, 3698, 2001.

Burger, R. A., and M. Hattingh, Toward a realistic diffusion tensor for galactic cosmic rays, *Astrophys. J.,505*(1), 244, 1998.

Burger, R. A., and M. Hitge, The effect of a Fisk-type heliospheric magnetic field on cosmic-ray modulation , *Astrophys. J. Lett., 617*, L73, 2004.

Burger, R. A., and M. S. Potgieter , The calculation of neutral sheet drift in two-dimensional cosmic-ray modulation model, *Astrophys. J., 339*(1), 501, 1989.

Burger, R. A., M. S. Potgieter, and B. Heber, Rigidity dependence of cosmic-ray proton latitudinal gradients measured by the Ulysses spacecraft: Implications for the diffusion tensor, *J. Geophys. Res., 105*(A12), 27447, 2000.

Burlaga, L. F., N. F. Ness, M. H. Acuna, R. P. Lepping, J. E. P. Connerney, E. C. Stone, F. B. McDonald, Crossing the termination shock into the heliosheath: Magnetic fields, *Science, 309*, 2027, 2005.

Caballero-Lopez, R. A., and H. Moraal, Limitations of the force field equation to describe cosmic ray modulation, *J. Geophys. Res, 109*(A1), 1101, 2004.

Casadei, D., and V. Bindi, The origin of cosmic ray electrons and electrons, *Astrophys. J., 612*, 262, 2004.

Chenette, D. L., T. F. Conlon, and J. A. Simpson, Burst of relativistic electrons from Jupiter observed in interplanetary space with time variation of planetary rotation period, *J. Geophys. Res.*, *79*, 3551, 1974.

Cliver, E. W., Solar energetic particles: Acceleration and transport, *AIP Conference Proc.*, 516, 103, 2000.

Coroniti, F. V., C. F. Kennel, F. L. Scarf, and E. J. Smith, Whistler mode turbulence in the disturbed solar wind, *J. Geophys. Res., 87*, 6029, 1982.

Decker, R. B., S. M. Krimigis, E. C. Roelof, M. E. Hill, T. P. Armstrong, G. Gloeckler, D. C. Hamilton, L. J. Lanzerotti, Voyager 1 in the foreshock, termination shock, and heliosheath, *Science, 309*, 2020, 2005.

Desai, M. I., M. E. Wiedenbeck, C. M. S. Cohen, J. E. Mazur, J. R. Dwyer, R. E. Gold and S. M. Krimigis, Spectral properties of heavy ions associated with the passage of interplanetary shocks at 1 AU, *Astrophys. J., 611*, 1156, 2004.

Dröge, W., Particle scattering by magnetic fields, *Space Sc. Rev.*, 93, 121, 2000.

Dröge, W., Probing heliospheric diffusion coefficients with solar energetic particles, *Adv. Space Res., 35*, 532, 2005.

Drury, L., An introduction to the theory of diffusive shock acceleration of particles in tenuous plasmas, *Rep. Prog. Phys., 46*, 973, 1983.

Earl, J. A., The diffusive idealization of charged-particle transport in random magnetic fields, *Astrophys. J., 193*, 231, 1974.

Ferreira, S. E. S., A study of the modulation of cosmic ray electrons in the heliosphere, *M.Sc. dissertation, Potchefstroom University for C.H.E.*, South Africa, 1998.

Ferreira, S. E. S., The heliospheric transport of galactic cosmic rays and jovian electrons, *Ph.D. thesis, Potchefstroom University for C.H.E.*, South Africa, 2002.

Ferreira, S. E. S., and M. S. Potgieter, Modulation over a 22-year cosmic ray cycle: On the tilt angles of the heliospheric current sheet, *Adv. Space Res.*, *32*, 657-662, 2003.

Ferreira, S. E. S., and M. S. Potgieter, Long-term cosmic ray modulation in the Heliosphere, *Astrophys. J.*, *603*, 744, 2004.

Ferreira, S. E. S., M. S. Potgieter, K. Scherer, Modulation of cosmic-ray electrons in a nonspherical and irregular heliosphere, *Astrophys. J.*, *607*, 1014, 2004.

Ferreira, S. E. S., M. S. Potgieter, R. A. Burger, and B. Heber, Modulation effects of anisotropic perpendicular diffusion on cosmic ray electron intensities in the heliosphere, *J. Geophys. Res., 105*(A8), 18305, 2000.

Ferreira, S. E. S., M. S. Potgieter, R. A. Burger, B. Heber, and H. Fichtner, Modulation of jovian and galactic electrons in the heliosphere 1. Latitudinal transport of few MeV electrons, *J. Geophys. Res.*, *106* (A11), 24979, 2001a.

Ferreira, S. E. S., M. S. Potgieter, R. A. Burger, B. Heber, H. Fichtner, and C. Lopate, Modulation of jovian and galactic electrons in the heliosphere: 2. Radial transport of a few MeV electrons, *J. Geophys. Res.*, *106* (A12), 29313, 2001b.

Ferreira, S. E. S., and K. Scherer, Modulation of cosmic-ray electrons in the outer heliosphere, *Astrophys. J.*, *616*, 1215, 2004.

Ferreira, S. E. S., and K. Scherer, Time evolution of galactic and anomalous cosmic-ray spectra in a dynamic heliosphere, *Astrophys. J.*, *642*, 1256, 2006.

Fichtner, H. Anomalous cosmic rays: Messengers from the outer heliosphere, *Space Sci. Rev.*, *95* (3/4), 639, 2001.

Fichtner, H., M. S. Potgieter, S. E. S. Ferreira, and R. A. Burger, On the propagation of jovian electrons in the heliosphere: transport modeling in 4-D phase space, *Geophys. Res. Lett., 27*(11), 1611, 2000.

Fichtner, H., S. R. Sreenivasan, and H. J. Fahr, Cosmic ray modulation and a non-spherical heliospheric shock, *Astron. Astrophys., 308*, 248, 1996.

Fisk, L. A., Solar modulation of galactic cosmic rays, *J. Geophys. Res., 76*, 221, 1971.

Fisk, L. A., Solar modulation of galactic cosmic rays. 4. Latitude dependent modulation, *J. Geophys. Res., 81*, 4646, 1976.

Fisk, L. A., Motion of the footpoints of heliospheric magnetic field lines at the Sun: Implications for recurrent energetic particle events at high heliographic latitudes, *J. Geophys. Res., 101* (A7), 15547, 1996.

Fisk, L. A., Journey into the unknown beyond, *Science, 309*, 2016, 2005.

Fisk, L. A., B. Koslovsky, and R. Ramaty, An interpretation of the observed Oxygen and Nitrogen enhancements in low-energy cosmic rays, *Astrophys. J., 190*, L35, 1974.

Florinski, V., and J. R. Jokipii, Cosmic-ray spectra at spherical termination shocks, *Astrophys. J., 591*, 454, 2003.

Florinski, V., G. P. Zank, J. R. Jokipii, E. C. Stone, A. C. Cummings, Do anomalous cosmic rays modify the termination shock?, *Astrophys. J., 610*, 1169, 2004.

Fujii, Z., and F. B. McDonald, Radial diffusion coefficients and the distance to the modulation boundary for galactic and anomalous cosmic rays, *Adv. Space Res., 27(3)*, 559, 2001.

Fujii, Z., and F. B. McDonald, The radial intensity gradients of galactic and anomalous cosmic rays, *Adv. Space Res., 23*(3), 437, 1999.

Garcia-Munoz, M., G. M. Mason, and J. A. Simpson, The abundances of galactic cosmic-ray Carbon, Nitrogen, and Oxygen and their astrophysical implications, *Astrophys. J., 184*, 967, 1973a.

Garcia-Munoz, M., G. M. Mason, and J. A. Simpson, A new test for solar modulation theory: the 1972 May-July low-energy galactic cosmic-ray proton and Helium spectra, *Astrophys. J., 182*, L81, 1973b.

Garcia-Munoz, M., G. M. Mason, and J. A. Simpson, The anomalous 1972 low-energy galactic cosmic ray proton and Helium spectra, *Proc. 13th Inter. Cosmic Ray Conf. (Denver), 2*, 1304, 1973c.

Gazis, P. R., A. Barnes, J. D. Mihalov, and A. J. Lazarus, Solar wind velocity and temperature in the outer heliosphere, *J. Geophys. Res., 99* (A4), 6561, 1994.

Gazis, P. R., A. Barnes, J. D. Mihalov, and A. J. Lazarus, The structures of the inner heliosphere from Pioneer, Venus and IMP observations, in *Solar Wind*, edited by E. Marsch and R. Schwenn, Pergamon Press., New York, 183, 1991.

Giacalone, J., The physics of particle acceleration by collisionless shocks, *Plan. Space Sci., 51*(11), 659, 2003.

Giacalone, J., The efficient acceleration of thermal protons by perpendicular shocks, *Astophys. J., 628*, L37, 2005.

Giacalone, J., and J. R. Jokipii, Energetic particle intensities and anisotropies near the solar wind termination shock, *Astrophys. J., 649*, L137, 2006.

Giacalone, J., and J. R. Jokipii, Injection and acceleration at non-parallel shocks, *29th Inter. Cosmic Ray Conf. (Pune), 00*, 101, 2005.

Giacalone, J., and J. R. Jokipii, The Transport of cosmic rays across a turbulent magnetic field, *Astophys. J., 520*(1), 204, 1999.

Giacalone, J., and J. R. Jokipii, The transport of energetic particles and cosmic rays in the heliosphere, *Adv. Space Res., 27*(3), 461, 2001.

Giacalone, J., J. R. Jokipii, and J. Kóta, Particle drifts in a fluctuating magnetic field, *Proc. 26th Inter. Cosmic Ray Conf. (Salt Lake City), 7*, 37, 1999.

Gil, A., and M. V. Alania, 27-day variations of cosmic rays for the minima epochs of solar activity: Experimental and 3-D drift modeling results, *Proc. 27th Inter. Cosmic Rays Conf. (Hamburg), 9*, 3725, 2001.

Gleeson, L. J., and W. I. Axford, Cosmic rays in the interplanetary medium, *Astrophys. J., 149*, L115, 1967.

Gleeson, L. J., and W. I. Axford, The Compton-Getting effect, *Astrophys. Space Sci., 2*, 431, 1968.

Gleeson, L. J., and G. M. Webb, Energy changes of cosmic rays in the interplanetary region, *Astrophysics and Space Science, 58*, 21, 1978.

Gosling, J. T., J. R. Asbridge, S. J. Bame, W. C. Feldman, R. D. Zwickl, G. Paschmann, N. Sckopke, R. J. Hynds, Interplanetary ions during an energetic storm particle event-The distribution function from solar wind thermal energies to 1.6 MeV, *J. Geophys. Res.,86*, 547, 1981.

Haasbroek, L. J., Modulation of cosmic rays in the heliosphere: A model study for the Ulysses mission (in Afrikaans), *M.Sc. dissertation, Potchefstroom University for C.H.E.*, South Africa, 1993.

Haasbroek, L. J., The transport and acceleration of charged particles in the heliosphere, *Ph.D. thesis, Potchefstroom University for C.H.E.*, South Africa, 1997.

Haasbroek, L. J., M. S. Potgieter, and J. A. le Roux, Acceleration of galactic and Jovian electrons at the heliospheric solar wind termination shock, *Adv. Space Res.*, *19* (6), 953, 1997a.

Haasbroek, L. J., M. S. Potgieter, and J. A. le Roux, Some modulation effects of termination shock accelerated galactic and jovian electrons, *Proc. 25th Inter. Cosmic Ray Conf. (Durban)*, *2*, 29,1997b.

Hasselmann, K., and G. Wibberenz, A note on the parallel diffusion coefficient, *Astrophys. J., 162*, 1049, 1970.

Hasselmann, K., and G. Wibberenz, Scattering of charged particles by random electromagnetic fields, *Zeitschrift für Geophysik, 34*, 353, 1968.

Hattingh, M., Drift of cosmic rays at a wavy neutral sheet in the heliosphere (in Afrikaans), *M.Sc. dissertation, Potchefstroom University for C.H.E.*, South Africa, 1993.

Hattingh, M., The modulation of galactic cosmic rays in a three-dimensional heliosphere, *Ph.D. thesis*, *Potchefstroom University for C.H.E.*, South Africa, 1998.

Hattingh, M., and R. A. Burger, A new simulated wavy neutral sheet drift model, *Adv. Space Res., 13* (9), 213, 1995.

Heber, B., J. M. Clem, R. Müller-Mellon, H. Kunow, S. E. S. Ferreira, and M. S. Potgieter, Evolution of the galactic cosmic ray electron to proton ratio: Ulysses COSPIN/KET observations, *Geophys. Res. Lett., 30* (19), ULY 6-1, 2003.

Heber, B., W. Dröge, P. Ferrando, L. J. Haasbroek, H. Kunow, R. Müller-Mellon, C. Paizis, M. S. Potgieter, A. Raviart, and G. Wibberenz, Spatial variation of > 40MeV/n nuclei fluxes observed during the ULYSSES rapid latitude scan, *Astron. Astrophys., 316*, 538, 1996.

Heber, B., A. Raviart, C. Paizis, M. Bailk, W. Dröge, R. Ducros, Modulation of galactic cosmic ray particles observed onboard Ulysses spacecraft, *Proc. 23rd Inter. Cosmic Ray Conf. (Calgary), 461*, 1993.

Hoeksema, J. T., Large scale structure of the heliospheric magnetic field: 1976-1991, In Marsh, E. and R. Schwenn eds. Solar wind seven. *Pergamon press, New York*, 191, 1992.

Hovestadt, D., O. Vollmer, G. Gloeckler, and C. Y. Fan, Measurement of elemental abundance of very low energy solar cosmic rays, *Proc. 13th Inter. Cosmic Ray Conf. (Denver)*, *2*, 1498, 1973.

Hu, Y. Q., S. R. Habbal, Y. Chen, and X. Li, Are coronal holes the only source of fast solar wind at solar maximum? *J. Geophys. Res.*, *108*(A10), SSH8-1, 2003.

Hundhausen, A. J., An interplanetary view of coronal holes, in *Coronal Holes and High Speed Streams*, edited by J. B. Zirker, Colorado Associated Univ. Press., Colorado, 114, 1977.

Jokipii, J. R., Cosmic-ray propagation. I. Charged particles in a random magnetic field, *Astrophys. J., 146*, 480, 1966.

Jokipii, J. R., Propagation of cosmic rays in the solar wind, *Rev. Geophys. Space Physics, 9*, 27, 1971.

Jokipii, J. R., Particle drift, diffusion, and acceleration at shocks, *Astrophys. J., 255*, 716, 1982.

Jokipii, J. R., Particle acceleration at a termination shock 1. Application to the solar wind and the anomalous component, *J. Geophys. Res., 91*, 2929, 1986.

Jokipii, J. R., Rate of energy gain and maximum energy in diffusive shock acceleration, *Astrophys. J. Lett.,313*, 842, 1987.

Jokipii, J. R., and J. Giacalone, Radial streaming of anisotropies of charged particles accelerated at the solar wind termination shock, *Astrophys. J., 605*, L145, 2004.

Jokipii, J. R., and J. Kóta, The polar heliospheric magnetic field, *Geophys. Res. Lett., 16*, 1, 1989.

Jokipii, J. R., and J. Kóta, On the interpretation of the high cosmic-ray electron fluxes observed in 1986, *Proc. 22nd Inter. Cosmic Ray Conf. (Dublin), 3*, 569, 1991.

Jokipii, J. R., and J. Kóta, The maximum energy of anomalous cosmic rays, *Proc. 24th Inter. Cosmic Ray Conf. (Rome), 4*, 718, 1995.

Jokipii, J. R., J. Kóta, and E. Merényi, The gradient of galactic cosmic rays at the solar wind termination shock, *Astrophys. J., 405*, 782, 1993.

Jokipii, J. R, E. H. Levy, and W. B. Hubbard, Effects of particle drift on cosmic ray transport. I – General properties, application to solar modulation, *Astrophys. J., 213*, 861, 1977.

Jokipii, J. R., and E. N. Parker, On the convection, diffusion and adiabatic deceleration of cosmic rays in the solar wind, *Astrophys. J., 160*, 735, 1970.

Jokipii, J. R., and B. Thomas, Effects of drifts on the transport of cosmic rays. IV – Modulation by a wavy interplanetary current sheet, *Astrophys. J., 243*, 1115, 1981.

Jones, F. C., and D. C. Ellison, The plasma physics of shock acceleration, *Space Sci. Rev., 58*, 259, 1991.

Kobayashi, T., Y. Komori, K. Yoshida, and J. Nishimura, The most likely source of High-Energy Cosmic-Ray electron in Supernova remnants, *Astrophys. J., 601*, 340, 2004.

Kojima, M., H. Washmimi, H. Misawa, and K. Hakamada, Solar wind observed within 0.3 AU with interplanetary scintilation, in *Solar Wind*, edited by E. Marsch, and R. Schwenn, Pergamon Press., New York, 201, 1991.

Koyama, K., R. Petre, E. V. Gotthelf, U. Hwang, M. Matsuura, M. Ozaki, and S. S. Holt, Evidence for shock acceleration of high-Energy electrons in the supernova remnant SN:1006, *Nature, 378*, 255, 1995.

Krieger, A. S., A. F. Timothy, and E. C. Roelof, A Coronal Hole and Its Identification as the Source of a High Velocity Solar Wind Stream, *Solar Physics, 29*, 505, 1973.

Krimigis, S. M., R. B. Decker, M. E. Hill, T. P. Armstrong, G. Gloeckler, D. C. Hamilton, L. J. Lanzerotti, E. C. Roelof, Voyager 1 exited the solar wind at a distance of ~ 85 AU from the Sun, *Nature, 426*, 45, 2003.

Krüger, T. P. J., The effects of a Fisk-Parker hybrid magnetic field on cosmic rays in the heliosphere, *M.Sc. dissertation, North-West University (Potchefstroom Campus)*, South Africa, 2005.

Krymski, G. F., A regular mechanism for the acceleration of charged particles on the front of a shock wave, *Sov. Phys. Dokl., 243*, 1306, 1977.

Kóta , J., and J. R. Jokipii, 3-D simulation of heliospheric transport: A comparison of models, *Proc. 25th Inter. Cosmic Ray Conf. (Durban), 2*, 25, 1997.

Kóta , J., and J. R. Jokipii, Cosmic ray modulation and the structure of the heiospheric magnetic field, *Proc. 26th Inter. Cosmic Ray Conf. (Salt Lake City), 7*, 9, 1999.

Kóta, J., and J. R. Jokipii, 3D distribution of cosmic rays in the outer heliosphere, *Proc. 24th Inter. Cosmic Ray Conf. (Rome), 4*, 670, 1995.

Kóta, J., and J. R. Jokipii, Effects of drift on the transport of cosmic rays. VI – A three-dimensional model including diffusion, *Astrophys. J., 265*, 573, 1983.

Kóta, J., and J. R. Jokipii, The role of corotating interaction regions in cosmic-ray modulation, *Geophys. Res. Lett., 18*, 1797, 1991.

Langner, U. W., Effects of different local interstellar spectra on the heliospheric modulation of cosmic rays, *M.Sc. dissertation, Potchefstroom University for C.H.E.*, South Africa, 2000.

Langner, U. W., Effects of termination shock acceleration on cosmic rays in the heliosphere, *Ph.D. Thesis, Potchefstroom University*, South Africa, 2004.

Langner, U. W., and M. S. Potgieter, Modulation of galactic protons in an asymmetrical heliosphere, *Astrophys. J., 630*, 1114, 2005.

Langner, U. W., and M. S. Potgieter, Possible explanations of anomalous spectra observed with Voyager 1 crossing the solar wind termination shock, *AIP Conf. Proc., 858*, 241, 2006.

Langner, U. W., M. S. Potgieter, T. Borrmann, and H. Fichtner, Effects of different solar wind speed profiles in the heliosheath on the modulation of cosmic-ray protons, *Astrophys. J., 640*, 2006a.

Langner, U. W., M. S. Potgieter, H. Fichtner, and T. Borrmann, Modulation of anomalous protons: Effects of different solar wind speed profiles in the heliosheath, *J. Geophys. Res., 111*, 2006b.

Langner, U. W., M. S. Potgieter, and W. R. Webber, Modelling of 'barrier' modulation for cosmic ray protons in the outer heliosphere, *Adv. Space Res., 34*(1), 138, 2004.

Langner, U. W., M. S. Potgieter, and W. R. Webber, Modulation of cosmic ray protons in the heliosheath, *J. Geophys. Res., 108*(A10), 8039, 2003.

Lapidus, L., and G. F. Pinder, *Numerical solution of partial differential equations in science and engineering*, Wiley, New York, 1982.

le Roux, J. A., The solar modulation of galactic cosmic rays as described by a time-dependent drift model, *Ph.D. thesis, Potchefstroom University for C.H.E.*, South Africa, 1990.

le Roux, J. A., and H. Fichtner, A self consistent determination of the heliospheric termination shock structure in the presence of pickup, anomalous, and galactic cosmic ray protons, *J. Geophys. Res., 102*(A8), 17365, 1997.

le Roux, J. A., M. S. Potgieter, and V. S. Ptuskin, A transport model for the diffusive acceleration and modulation of anomalous cosmic rays in the heliosphere, *J. Geophys. Res., 101*, 4791, 1996.

Lemmer, M., Die invloed van die interpleenitêre magneetveld op die daaglikse variasie van kosmiese strale, *M.Sc. dissertation, Potchefstroom University for C.H.E.*, South Africa, 1982.

Longair, M. S., Cosmic rays and the Galactic radio background emission, in *Low Frequency Astrophysics from Space*, Springer-Verlag, 227, 1990.

Marsch, E., Kinetic physics of the solar wind plasma, in *Physics of the Inner Heliosphere*, edited by R. Schwenn and E. Marsch, Springer-Verlag, Berlin, 45, 1991.

Marsden, R. G. (Ed.), The 3-D Heliosphere at Solar Maximum, *Space Sci, Rev., 97*(1-4), 2001.

Marsden, R. G. (Ed.), The High Latitude Heliosphere, *Space Sci. Rev., 72*(1/2), 1995.

McComas, D. J., H. A. Elliot, J. T. Gosling, D. B. Reisenfield, R. M. Skoug, B. E. Goldstein, M. Neugebauer, and A. Balogh, Ulysses' second fast-latitude scan: Complexity near solar maximum and the reformation of polar coronal holes, *Geophys. Res. Lett., 29*(9), 4-1, 2002b.

McComas, D. J., H. A. Elliot, and R. Von Steiger, Solar wind from high-latitude coronal holes at solar maximum, *Geophys. Res. Lett., 29*(9), 28(1-4), 2002a.

McComas, D. J., and N. A., Schwadron, An explanation of the Voyager paradox: Particle acceleration at a blunt termination shock, *Geophys. Res. Lett., 33*, 4102, 2006.

McDonald, F. B., B. Heikkila, N. Lal, and E. C. Stone, The relative recovery of galactic and anomalous cosmic rays in the distant heliosphere: Evidence for modulation in the heliosheath, *J. Geophys. Res., 105*(A1), 1, 2000.

McDonald, F. B., E. C. Stone, A. C. Cummings, B. Heikkila, N. Lal, and W. R. Webber, Enhancements of energetic particles near the heliospheric termination shock, *Nature, 426*, 48, 2003.

McDonald, F. B., B. J. Teegarden, J. H. Trainor, and W. R. Webber, The Anomalous Abundance of Cosmic-Ray Nitrogen and Oxygen Nuclei at Low Energies, *Astrophys. J., 187*, L105, 1974.

McKibben, R. B., Cosmic-ray diffusion in the inner heliosphere, *Adv. Space Res., 35*, 518, 2005.

McKibben, R. B., J. J. Connell, C. Lopate, J. A. Simpson, M. Zhang, Observations of galactic cosmic rays and the anomalous helium during Ulysses passage from the south to the north solar pole, *Astron. Astrophys, 316*, 547, 1996.

Möbius, E., Pick-up of interstellar neutrals by the solar wind, *Adv. Space Res., 6*(1),199, 1986.

Möbius, E., D. Hovestadt, B. Klecker, M. Scholer, and G. Gloeckler, Direct observation of He(+) pick-up ions of interstellar origin in the solar wind, *Nature, 318*, 426, 1985.

Moeketsi, D. M., Modelling of galactic and jovian electrons in the heliosphere, *M.Sc. dissertation, North-West University (Potchefstroom Campus)*, South Africa, 2004.

Moeketsi, D. M., M. S. Potgieter, S. E. S. Ferreira, B. Heber, H. Fichtner, and V. K. Henize, The heliospheric modulation of 3-10 MeV electrons: Modeling changes in the solar wind speed in relation to perpendicular polar diffusion,Adv. *Space Res., 35*(4), 597, 2005.

Moraal, H., and W. I. Axford, Cosmic ray acceleration in supernova blast waves, *Astron. Astrophys., 125*(2), 204, 1983.

Moraal, H., R. A. Caballero-Lopez, K. G. McCracken, and J. E. Humble, The influence of cosmic-ray modulation at high heliospheric latitudes on the solar diurnal variation observed at Earth, *Astrophys. J., 629*, 556, 2005.

Moraal, H., J. R. Jokipii, and R. A. Mewaldt, Heliospheric effects on cosmic-ray electrons, *Astrophys. J., 367*, 191, 1991.

Moskalenko, I. V., A. W. Strong, J. F. Ormes, and M. S. Potgieter, Secondary antiprotons and propagation of cosmic rays in the galaxy and heliosphere, *Astrophys. J., 565*, 280, 2002.

Ndiitwani, D. C., A study of the modulation of galactic time-dependent cosmic rays in the heliosphere, *M.Sc. dissertation, North-West University (Potchefstroom Campus)*, South Africa, 2005.

Neugebauer, M., P. C. Liewer, E. J. Smith, R. M. Skoug, and T. H. Zurbuchen, Sources of the solar wind at solar activity maximum, *J. Geophys. Res., 107*, SSH13-1, 2002.

Ngobeni, M. D., and M. S. Potgieter, Cosmic ray anisotropies in the outer heliosphere, *Adv. Space Res., in press*, 2007.

Odstrcil, D., Modeling 3-D solar wind structure, *Adv. Space Res., 32*(4), 497, 2003.

Parker, E. N., Cosmic ray modulation by the solar wind, *Physical Rev., 110*, 1445, 1958.

Parker, E. N., Interplanetary dynamical processes, *Interscience*, New York, 1963.

Parker, E. N., Sudden expansion of the corona following a large solar flare and the attendant magnetic field and cosmic-ray effects, *Astrophys. J., 133*, 1014, 1961.

Parker, E. N., The passage of energetic charged particles through interplanery space, *Planet. Space Sci, 13*, 9, 1965.

Pauls, H. L., and G. P. Zank, Interaction of a nonuniform solar wind with local interstellar medium, *J. Geophys. Res., 101*(A8), 17081, 1996.

Pauls, H. L., and G. P. Zank, Interaction of a nonuniform solar wind with local interstellar medium 2. A two-fluid model, *J. Geophys. Res., 102*(A9), 19779, 1997.

Pauls, H. L., G. P. Zank, and L. L. Williams, Interaction of the solar wind with the local interstellar medium, *J. Geophys. Res., 100*(A11), 21595, 1995.

Pesses, M. E., J. R. Jokipii, and D. Eichler, Cosmic ray drift, shock wave acceleration and the anomalous component of cosmic rays, *Astrophys. J., 246*, L85, 1981.

Philips, J. L., A. Balogh, S. J. Bame, B. E. Goldstein, J. T. Gosling, J. T. Hoeksema, D. J. McComas, M. Neugebauer, N. R. Sheeley, and Y. M. Wang, Ulysses at 50° south: constant immersion in the high-speed solar wind, *Geophys. Res. Lett., 21*(12), 1105, 1994.

Philips, J. L., S. J. Bame, B. L. Barraclough, W. C. Feldman, B. E. Goldstein, J. T. Gosling, G. W. Hoogeveen, D. J. McComas, M. Neugebauer, and S. T. Suess, Ulysses solar wind plasma observations from pole to pole, *Geophys. Res. Lett., 22*(23), 3301, 1995.

Potgieter, M. S., The modulation of galactic cosmic rays as described by a three-dimensional drift model, *Ph.D. thesis, Potchefstroom University for C.H.E.*, South Africa, 1984.

Potgieter, M. S., Heliospheric terminal shock acceleration and modulation of the anomalous cosmic-ray component, *Adv. Space Res.,9*(12), 21, 1989.

Potgieter, M. S., The heliospheric modulation of galactic electrons: consequences of new calculations for the mean free path of electrons between 1 MeV and 10 GeV, *J. Geophys. Res., 101*, 24411, 1996.

Potgieter, M. S., The heliospheric modulation of cosmic ray protons: role of enhanced perpendicular diffusion during periods of minimum solar modulation, *J. Geophys. Res., 105*, 18295, 2000.

Potgieter, M. S., and H. Moraal, A drift model for the modulation of galactic cosmic rays, *Astrophys. J., 294*, 425, 1985.

Potgieter, M. S., and H. Moraal, Acceleration of cosmic rays in the solar wind termination shock. I – A steady state technique in a spherically symmetric model, *Astrophys. J.,330*, 445, 1988.

Potgieter, M. S., L. J. Haasbroek, and B. Heber, The modelling of the latitude dependence of cosmic ray protons and electrons in the inner heliosphere, *Adv. Space Res., 19* (6), 917, 1997.

Potgieter, M. S., J. A. le Roux, and R. A. Burger, Interplanetary cosmic ray radial gradients with steady state modulation models, *J. Geophys. Res., 94*, 2323, 1989.

Reinecke, J. P. L., H. Moraal, and F. B. McDonald, The cosmic radiation in the heliosphere at successive solar minima 3. Steady-state drift solutions of the transport equation, *J. Geophys. Res., 101*, 21581, 1996.

Richardson, J. D., C. Wang, and K. I. Paularena, The solar wind: From solar minimum to solar maximum, *Adv. Space Res., 27*(3), 471, 2001.

Scherer, K., and H. J. Fahr, Solar cycle induced variations of the outer heliospheric structures, *Geophys. Res. Lett., 30*(2), 17, 2003.

Scherer, K., and S. E. S. Ferreira, A heliospheric hybrid model: Hydrodynamic plasma flow and kinetic cosmic ray transport, *ASTRA, 1*, 17, 2005.

Scherer, K., S. E. S. Ferreira, M. S. Potgieter, and H. Fichtner, Time and latitude-dependence of the compression ratio and the injection efficiency at the heliospheric termination shock, *AIP Conf. Proc., 858*, 20, 2006.

Schwenn, R., The average solar wind in the inner heliosphere: Structures and slow variations, in *Solar Wind five*, edited by M. Neugebauer, NASA CP-2280, 489, 1983.

Sheeley, N. R., Y. M. Wang, S. H. Hawley, G. E. Brueckner, K. P. Dere, R. A. Howard, M. J. Kooman, C. M. Korendyke, D. J. Michels, S. E. Paswaters, D. G. Socker, O. C. St. Cyr, D. Wang, P. L. Lamy, A. Llebaria, R. Schwenn, G. M. Simnett, S. Plunkett, and D. A. Biesecker, Measurements of flow speeds in the corona between 2 and 30 R sub sun, *Astrophys. J., 484*, 472, 1997.

Siluszyk, M., and M. V. Alania, On the internal boundary condition problem for Parker's transport equation of galactic cosmic rays, *Proc. 27th Inter. Cosmic Rays Conf. (Hamburg), 9*, 3722, 2001.

Simpson, J. A., Cosmic radiation: Particle astrophysics in the heliosphere, in *Frontiers in Cosmic Physics: Symposium in memory of Serge Korff*, edited by R. B. Mendell, and A. J. Mincer, New York Academy of Sciences, New York, 97, 1992.

Simpson, J. A., The cosmic radiation: Reviewing the present and future, *Proc. 25th Inter. Cosmic Ray Conf. (Durban),2*,4, 1998.

Simpson, J. A., D. Hamilton, G. Lentz, R. B. McKibben, A. Mogro-Campero, M. Perkins, K. R. Pyle, A. J. Tuzzolino, and J. J. O'Gallagher, Protons and electrons in Jupiter's magnetic field: Results from the university of Chigago experiment on Pioneer 10, *Science, 183*(4122), 306, 1974.

Smith, E. J., The Sun, solar wind and magnetic field. I, in *Proc. Inter. School of Physics "Enrico Fermi" Course CXLII*, edited by B. Coppi, A. Ferrari, and E. Sindoni, IOS Press., Amsterdam, 179, 2000.

Smith, E. J., The heliospheric current sheet, *J. Geophys. Res.,106*(A8), 15819, 2001.

Smith, C. W., and J. W. Bieber, Solar cycle variation of the interplanetary magnetic field spiral, *Astrophys. J., 370*, 435, 1991.

Smith, E. J., and R. G. Marsden, Ulysses Observations at Solar Maximum: Introduction, *Geophys. Res. Lett.,30*(19), 1, 2003.

Smith, E. J., R. G. Marsden, A. Balogh, G. Gloeckler, J. Geiss, D. J. McComas, R. B. McKibben, R. J. MacDowall, L. J. Lanzerotti, N. Krupp, H. Krueger, and M. Landgraf, The Sun and heliosphere at solar maximum: Review, *Science, 302*, 1165, 2003.

Snodgrass, H. B., Magnetic rotation of the solar photosphere, *Astrophys. J., 270*, 288, 1983.

Sokolov, I. V., I. I. Roussev, L. A. Fisk, M. A. Lee, T. I. Gombosi, and J. I. Sakai, Diffusive shock acceleration theory revisited, *Astrophys. J., 642*, L81, 2006.

Stawicki, O., On magnetic fluctuations in the solar wind and their influence on the transport of charged particles, *Ph.D. Thesis, Ruhr-Universität Bochum*, Germany, 2003.

Steenberg, C. D., Modelling of anomalous and galactic cosmic ray modulation in the outer heliosphere, *Ph.D. Thesis, Potchefstroom University for C.H.E.*, South Africa, 1998.

Steenkamp, R., Shock acceleration as source of the anomalous component of cosmic rays in the heliosphere, *Ph.D. Thesis, Potchefstroom University for C.H.E.*, South Africa, 1995.

Stone, E. C., The solar wind termination shock and the outer heliosphere, *Frontiers of Cosmic Ray Science*, 383, 2004.

Stone, E. C., and A. C. Cummings, Estimate of the location of the solar wind termination shock, *Proc. 27th Inter. Cosmic Ray Conf. (Hamburg), 10*, 4263, 2001.

Stone E. C., A. C. Cummings, F. B. McDonald, B. C. Heikkila, N. Lal, and W. R. Webber, Voyager 1 Explores the termination shock region and the heliosheath beyond, *Science, 309*, 2017, 2005.

Suess, S. T., Temporal variations in the termination shock distance, *J. Geophys. Res., 98*(A9), 15147, 1993.

Tanimori, T., T. Hayami, S. Kamesi, S. A. Dezeley, P. G. Edwards, S. Gunji, S. Hara, T. Hara, J. Holder, A. Kawachi, T. Kifune, R. Kita, T. Konishi, A. Masaike, Y. Matsubara, T. Matsuoka, Y. Mizumoto, M. Mori, M. Moriya, H. Muraishi, Y. Muraki, T. Naito, K. Nishijima, S. Oda, S. Ogio, J. R. Patterson, M. D. Roberts, G. P. Rowell, K. Sakurazawa, T. Sako, Y. Sato, R. Susukita, A. Suzuki, R. Suzuki, T. Tamura, G. J. Thornton, S. Yanagita, T. Yoshida, and T. Yoshikoshi, Discovery of TeV Gamma Rays from SN 1006: Further Evidence for the Supernova Remnant Origin of Cosmic Rays, *Astrophys. J., 497,* L25, 1998.

Teegarden, B. J., F. B. McDonald, J. H. Trainor, W. R. Webber, and E. C. Roelof, Interplanetary MeV electrons of jovian origin, *J. Geophys. Res., 79,*3615, 1974.

Teufel, A., I. Lerche, and R. Schlickeiser, Cosmic ray transport in anisotropic magnetohydrodynamic turbulence II. Shear Alfvén waves, *Astron. Astrophys., 397*, 777, 2003.

Teufel, A., and R. Schlickeiser, Analytic calculation of the parallel mean free path of interplanetary cosmic rays I. Dynamical magnetic slab turbulence and random sweeping model, *Astron. Astophys., 393*, 703, 2002.

Teufel, A., and R. Schlickeiser, Analytic calculation of the parallel mean free path of heliospheric cosmic rays II. Dynamical magnetic slab turbulence and random sweeping slab turbulence with finite wave power at small wavenumbers, *Astron. Astrophys., 397*, 15, 2003.

van Niekerk, Y., An investigation into the causes and consequences of north-south asymmetries in the heliosphere, *M.Sc. dissertation, Potchefstroom University for C.H.E.*, South Africa, 2000.

van staden, M. L., and M. S. Potgieter, The effect of the changing polarity and neutral sheet of the IMF on the cosmic ray diurnal anisotropy at neutron monitor energies, *Plan. Space Sci., 39*(9), 1233, 1991.

Von Rosenvinge, T. T., and F. B. McDonald, IMP 6, 7 and 8 observations of the composition and time variations of low energy cosmic rays, *Proc. 14th Inter. Cosmic Ray Conf. (Munich), 2*, 92, 1975.

Webber, W. R., and J. A. lockwood, Onset and amplitude of the 11-year solar modulation of cosmic ray intensities at Earth and at Voyager 1 and 2 during the period 1997 to 2003, *J. Geophys. Res., 109*, 2004.

Webber, W. R., and J. A. Lockwood, Voyager and Pioneer spacecraft measurements of cosmic ray intensities in the outer heliosphere: Toward a new paradigm for understanding the global modulation process: 1. Minimum solar modulation (1987 and 1997), *J. Geophys. Res., 106*(A12), 29323, 2001.

Withroe, G. L., W. C. Feldman, and H. S. Ahluwalia, The solar wind and its coronal origins, in *Solar interior and atmosphere*, edited by A. N. Cox, W. C. Livingstone, and M. S. Mathews, University of Arizona Press., Tucson, 1087, 1992.

Zank, G. P., Interaction of the solar wind with the local interstellar medium: A theoretical perspective, *Space Science Reviews, 89*(3/4), 413, 1999.

Zank, G. P., W. H. Matthaeus, and C. W. Smith, Evolution of turbulent magnetic fluctuation power with heliospheric distance, *J. Geophys. Res., 101*(A8), 17093, 1996.

Zank, G. P., and H. R. Müller, The dynamical heliosphere, *J. Geophys. Res., 108*(A6), SSH 7-1, 2003.

Zank, G. P., W. K. M. Rice, I. H. Cairns, J. W. Bieber, R. M. Skoug, and C. W. Smith, Predicted timing for the turn-on of radiation in the outer heliosphere due to the Bastille Day shock, *J. Geophys. Res.,106*(A12), 29363, 2001.

Acknowledgements

I would like to express my gratitude to the following people and institutions in no particular order:

- Heavenly Father for having given me this few and far between opportunity to comprehend a small portion of his splendid creation.
- Prof. Marius Potgieter, my supervisor, for his splendid guidance, suggestions, explanations and motivation.
- Dr. Langner, my assistant supervisor, for his assistance with the numerical code.
- Mr Golden Nyambuya for his friendship, dialogs, support and trust.
- Mr Sibusiso Nkosi for his discussions.
- Mr Matthew Holleran for his unwavering assistance with computer related problems and queries.
- My friends, Va ka Mabedle, Isak, Rammy, Chris, Wantukulu, Standley, Tiyani, Aluwani, Mr B, Collen, Freddy, Oscar e.t.c. those not mentioned are not less important.
- The Unit for Space Physics at the North-West University Potchefstroom Campus for the use of their facilities.
- The South African National Research Foundation and Department of Labour of South Africa for their financial support.
- Mrs. Petro Sieberhagen and Mrs. Lizelle le Roux for all their administrative assistance.

A special thanks to:

- My parents, Mbhazima (Xikoci) and Florah-Ntsumele Ngobeni, for everything.
- My brother, Thomas Ngobeni, for your friendship, motivation, support and your understanding and love for education.
- Brother Khazamula Ngobeni the path finder.

I dedicate this dissertation to my mother, Florah Ntsumele-Ngobeni.

DYONDZO A YI LUMI!